Evaluating Track Stiffness and Rail Bending Moments using Vertical Track Deflection Measurements Considering the Effects of Track Geometry

by

Ngoan Tien Do

A thesis submitted in partial fulfillment of the requirements for the degree of

Doctor of Philosophy

in

STRUCTURAL ENGINEERING

Department of Civil and Environmental Engineering
University of Alberta

Abstract

Vertical track stiffness (or track modulus) is generally accepted as one of the key structural properties of track which impacts the bearing capacity, dynamic response of passing trains, quality of track geometry, and track components' life. Although it is known that track stiffness parameters can potentially provide useful information for track condition assessment, there is a lack of understanding of factors affecting the track stiffness measurements such as the effects of track geometry variations. For this reason, attempts to establish an automatic framework for track condition assessment using a track stiffness measurement system are limited. In this context, this thesis develops methods for assessing the track stiffness using vertical track deflection (VTD) measurements.

First, the effectiveness of using measured data from a continuous track stiffness measurement system for estimating track modulus and rail bending moments is investigated. Developed finite element models are employed to study the impacts of applied loads and track modulus on the resulting VTDs and rail bending moments. The relationship between the VTDs and track modulus and bending moments are established using artificial neural networks and wavelet-based techniques. Specifically, local variations of track modulus for different track section lengths are estimated from VTD measurements while the local extremum values of bending moments are also quantified.

Second, the effects of track geometry and other factors on the VTD measurements are investigated in detail. To understand the relationship between track modulus and track geometry in the measured VTD data, dynamic simulations are conducted to simulate the stochastic variations of track modulus and track geometry. A novel blind source separation technique is developed to reveal the track geometry and track modulus information separately using the numerical VTD measurements. Subsequently, the methodology is further improved and validated with field data collected from a study site. The track geometry variations and VTD collected at the study site support the proposal of using a continuous track stiffness measurement system for both track stiffness and track geometry quality evaluations. The investigation of the field VTD data also reveals the impact of motions of the vehicle carrying the track stiffness measurement system on

the reading of VTD values. Finally, conclusions and recommendations for future research are included in the thesis.

Preface

This thesis is an original work of Ngoan Do. Four chapters in the thesis have been published or submitted/under preparation for submission for publication.

A version of Chapter 3 has been published in Vibration journal, as Do N, Gül M, Fallah Nafari S, "Continuous Evaluation of Track Modulus from a Moving Railcar Using ANN-based Techniques". Ngoan Do was responsible for formal analysis and manuscript preparation. Dr. Gül was the supervisory author and took part in concept formulation, manuscript composition, and supervision. Dr. Fallah Nafari was responsible for providing the numerical data and manuscript edits.

A version of Chapter 4 has been submitted to the Journal of Transportation Engineering, Part A: Systems, as Do N, Gül M, "Estimations of Vertical Bending Moments in Rail from Relative Rail Deflection Data Using Wavelet Analysis and Radial Basis Function Neural Networks". Ngoan Do was responsible for formal analysis and manuscript preparation. Dr. Mustafa Gül was responsible for concept formulation, manuscript review and edits, and supervision.

A version of Chapter 5 has been submitted to the Journal of Mechanical Systems and Signal Processing, as Do N, Gül M, "A Recursive SSA-AMUSE Based Technique for Single Channel Blind Source Separation with an Application on Vertical Track Deflection Measurements". Ngoan Do responsible for concept formulation, formal analysis, and manuscript preparation. Dr. Mustafa Gül was responsible for concept formulation, manuscript review, and supervision.

A version of Chapter 6 will be submitted to the Proceedings of the Institution of Mechanical Engineers, Part F: Journal of Rail and Rapid Transit for publication, as Do N, Gül M, Hendry M.T, "A Hybrid Single Channel Blind Source Separation Technique for Extracting Track Geometry and Stiffness with a Real-life Application". Ngoan Do was responsible for concept formulation, formal analysis, and manuscript preparation. Dr. Mustafa Gül was responsible for concept formulation, manuscript composition, and supervision. Dr. Michael Hendry provided the field data, technical support for interpreting the results and manuscript review and edits.

To my son Richard "Cu Đen", my unborn baby, and my wife

Acknowledgments

First and foremost, I would like to express my thanks and my deepest gratitude to Dr. Mustafa Gül; for his guidance, kind support, and friendship throughout this study. He has inspired me and had a great influence on my professional life. None of this would have been possible without his mentorship and help.

I am greatly thankful Dr. Michael Hendry from the Canadian Rail Research Laboratory, University of Alberta for his valuable feedback and technical support. I am also very thankful to Dr. Saeideh Fallah Nafari, former PhD student for her constructive comments and help.

I would like to thank Dr. Neil Hoult from Queen's University, Dr. Vivek Bindiganavile, and Dr. Ben Jar from the University of Alberta for serving as my committee members and providing valuable feedback and recommendations.

This research was made possible through IC-IMPACTS (the India-Canada Centre for Innovative Multidisciplinary Partnerships to Accelerate Community Transformation and Sustainability), established through the Networks of Centres of Excellence of Canada.

I also would like to thank to the current and former members of our research team, Branislav Kostic, Jianfeng Gu, Qipei Mei, Haiyang Zhang, Riasat Azim, and Nima Shirzad-Ghaleroudkhani for their collaboration and help.

And of course, my family. My beloved wife, Thanh Thuy, has sacrificed everything for the family and constantly supported me in pursuing my unending education. My little angels, Richard "Cu Đen" and the unborn baby, who always make me feel positive and proud.

Table of Contents

List of Tables

List of Figures

Chapter 1: Introduction

1.1. Description of problem

With the total length of more than 48,000 kilometers, the Canadian railway network stands out as the fifth-longest network in the world, which reflects its vital role in the Canadian infrastructure system. In fact, 70% of the country's goods are transported by the heavy haul railway [1]. As the economy has been rapidly growing, the demand for higher transport volume and speeds is expected. As a result, timely inspections of the railway infrastructure for a proactive maintenance approach is especially required to prevent potential risks, ensure the safety of the railway networks, and minimize the life-cycle costs.

One of the most challenging tasks in management of the civil infrastructure system (CIS) is the maintenance of existing structures. Among different components of CIS, railway systems are essential parts and they are considered as "the blood lines" of almost every country. In addition to the aging material, railway lines are exposed to a harsh environment that contributes to their structural degradations. In the USA, broken rails or welds and track geometry defects have been reported as the leading causes of derailments [2,3]. In 2016, specifically, the Federal Railroad Administration (FRA), Office of Safety Analysis indicated 26.9% of train accidents are due to track related causes (e.g. track geometry defects, broken rails and welds) [4]. In Canada, 1,091 rail accidents were reported in 2017, where 55% of the accidents were related to main-track and non-main-track derailments. In terms of potential risks to the public and financial loss, main-track collisions and derailments are among the most serious categories although these problems make up 7.3% of the total number of occurrences. Also, track-related factors constituted 35% percent of the main-track problems (ten-year average from 2007 to 2017) [5]. Therefore, it is necessary to develop an automatic railway structural health monitoring framework for assessment of rail and track performance.

Evaluation of track performance by means of vertical track deflections (VTD) is one of the commonly used methods for track assessment. Soft subgrades or low track modulus (defined as the vertical stiffness of the subgrade components that form the track's foundation) result in large rail deflections and contribute to the degradations of track's components and rail failures. Recently, continuous track stiffness measurement systems have been developed in Europe, North America, and Asia for VTD measurements [6-9]. The difference among the systems is either relative or absolute deflections are recorded over long distances, from which subgrade conditions along the rail can be assessed globally. Although one of the first VTD systems was developed around two decades ago [9], mathematical relations between track modulus and vertical rail defections are simplified and require further investigations. Given the fact that rail deflections are greatly affected by loading conditions, track geometry, and other factors, one of the main objectives of this study is to develop a methodology for estimating the track modulus and its spatial variation over long distances considering track geometry effects. The outcome of this research is expected to facilitate a better understanding of the root causes of track-related problems by providing useful information about track stiffness as well as track geometry.

In addition, rail bending moments and the corresponding stresses are key parameters to assess the structural behaviour of rail under train loads [10]. Bending stresses are magnified by operational and environmental conditions. For instance, various stresses such as residual, thermal, and wheel-rail contact are induced during manufacturing and operating processes [11-14]. Under environmental effects, rail stress along thousands of kilometers of track may vary unfavorably. Even though different studies were conducted to quantify the variations of rail stress using numerical models, analytical approaches, and track-side measurement techniques [15-18], there are limited methods that can evaluate operational rail stresses over long distance. The development of VTD systems have opened new opportunities for investigating rail bending stress [19-22]. Even so, estimations of rail bending stress from moving cars presented in the literature require more sophisticated analysis so that uncertainties associated with track stiffness variations and other factors related to the measurement system are considered.

As mentioned above and detailed in the next chapter, there are considerable efforts devoted to the developments of train-mounted systems for track modulus and stiffness measurements. However, there are major concerns regarding the implementations of these systems in existing railway structures:

- Further investigations for interpreting VTD measurements are required. For instance, the track stiffness measurement system MRail [23] was developed mainly based on the numerical Winkler model that relates the vertical track modulus to the corresponding deflection under known wheel loads. However, the Winkler model assumes rails as continuous beams on elastic foundation with constant track modulus, which is not necessarily true;

- Moreover, most processing techniques for relating measured data to track stiffness mainly rely on statistical analysis, i.e. mean and standard deviation [22,24-26]. It is widely known that vertical rail deflection measurements are highly non-stationary due to the variations of track stiffness, track geometry, and superstructure's structural properties. Therefore, other techniques are required to extract meaningful features from the data;
- Track geometry variations are considered as the primary factors coinciding with the degradation of track performance. In fact, track irregularities have been utilized to define track quality in different manuals and studies. However, most available continuous track stiffness measurement systems ignore or simplify the effects of track geometry on the recorded deflection data. Due to the presence of these effects in the measured data, track stiffness cannot be accurately evaluated;
- Measured vertical track deflections are a combination of void, seating, and contact deflections together with the influence of track roughness (or track geometry). As these types of information are usually prominent in the raw VTD data, further validations of the usefulness of using track stiffness measurement systems for providing information about substructure conditions are required.

1.2. Objectives and Scope

The main objective of this PhD study is to develop different methodologies to quantitatively evaluate track modulus, track geometry variations, and rail bending moments through a continuous track stiffness measurement system. The specific research objectives of this doctoral research are outlined below:

Objective 1: Evaluate the track modulus and its variation using vertical track deflection data

- Utilize available finite element models (FEMs) to examine the relationship between the numerical VTD and the corresponding varying track modulus;
- Propose an artificial neural network (ANN)-based method to estimate the varying track modulus from the VTD data;

- Propose an ANN-based method to estimate the track modulus' variations from the VTD data.

Objective 2: Quantify the maximum positive and negative rail bending moments using continuous track stiffness measurement data

- Utilize extracted VTD measurements from the developed FEMs to investigate the impacts of varying track modulus on rail bending moments;
- Propose two methods to estimate the local extrema of positive and negative bending moments from VTD data using ANN and Wavelet Multiresolution analysis (WMRA).

Objective 3: Propose a blind source separation method to separate the track geometry information from VTD measurements for accurate vertical track stiffness evaluations.

- Dynamic models of flexible track with moving wheelsets are developed to simulate the effects of track geometry variations and varying track modulus on the track response under moving loads;
- Investigate the effects of individual track geometry parameters on the simulated VTD measurements;
- Propose a blind source separation method to separate the track geometry information from VTD measurements so that the processed data can reveal information about the vertical track stiffness.

Objective 4: Develop an improved methodology for separating track geometry and track modulus information using real-life continuous track stiffness measurement data

- Analyze the track geometry and VTD measurements to validate the proposed blind source separation technique for evaluating track quality and subgrade conditions using VTD measurements only;
- Further investigate the effects of individual track geometry parameters and other factors on VTD data and propose solutions to minimize these effects.

In this study, VTD data measured using a continuous track stiffness measurement system developed at the University of Nebraska – Lincoln (commonly known as the MRail system) was selected for analysis and validations primarily due to its application on Canadian railway lines.

Although the current methodologies are proposed based on the MRail VTD data, other VTD data measured by similar continuous track stiffness measurement system are still applicable. However, minor changes in the computational steps would be needed as VTD data from different systems are different due to the unique measurement method in each system.

1.3. Research contribution

Several continuous track stiffness measurement systems have been developed for track stiffness evaluations. However, investigating the effects of track geometry on the recorded VTD data is limited or only longitudinal track geometry (i.e. profile) is considered as the primary effect. The main contribution of this thesis is the development of a detailed methodology for evaluating track modulus variations and track quality from VTD measurements. The methodology facilitates better track quality evaluations by accurately estimating track modulus as well as high track geometry variations. A detailed investigation is conducted to confirm the substantial effects of track geometry parameters other than the profile on the VTD measurements. To the best of the author's knowledge, this is the first study that introduces the concept of blind source separation to VTD measurements. Additionally, the study proposes different methodologies for continuously estimating track modulus and rail bending stresses using VTD measurements putting a forward step to the structural integrity assessments of rail component.

1.4. Organization of the thesis

This thesis is presented in a paper-based format. The thesis consists of seven chapters, including this first introductory chapter:

Chapter 2 covers necessary literature review for this study. First, different types of loads and rail stresses are reviewed. Then, damage mechanisms in rail steel and the impacts of track quality on the rail life are presented. The chapter includes an introduction about track geometry measurements followed by a review of methods for track quality assessments. This chapter also presents the important role of track modulus in track performance. A detailed review of continuous track stiffness measurement systems is also presented.

Chapter 3 presents the study conducted to estimate track modulus and its variation from VTD data measured by a continuous track stiffness measurement system (i.e. MRail). Track stiffness measurement techniques are reviewed followed by the details about the MRail system. The chapter includes two methodologies that employ ANNs, statistical, and frequency analysis for estimating track modulus average and standard deviation from simulated VTD data. Comparisons with the related studies are also presented to show the effectiveness of the current methods.

Chapter 4 presents the study about the impacts of VTD on rail bending moments. A methodology that utilizes Radial basis function neural networks and Wavelet resolution analysis for estimating the local extrema of positive bending moments from the corresponding VTD measurements is presented. The local minima of negative bending moments are also estimated. The effectiveness of the methods is validated using the developed FEM with stochastic track modulus.

Chapter 5 presents a methodology that utilizes a new single channel blind source separation technique to separate the track geometry effects from the VTD for evaluating track modulus. Background and mathematical development of the proposed method are first introduced. The effectiveness of the proposed method is first evaluated by its performance in separating a single mixed synthetic signal into originally separated signals. The method is subsequently used to analyze the VTD signals which are extracted from a dynamic model developed by using a multibody dynamic simulation package and ABAQUS. The effects of random track geometry and varying track modulus are also simulated in the model. Finally, the results, effectiveness and limitations of the proposed method are discussed.

Chapter 6 presents a modified blind source separation technique for evaluating track quality and track modulus variations using field VTD data. The track geometry and the MRail VTD data measured along a revenue track are analyzed. The estimated variations of the track profile are compared with the actual measurements. The proposed flexibility index for track modulus evaluations is validated with specific site's assessments. Furthermore, the chapter presents the finding about the significant impact of superelevataion on the VTD measurements.

Chapter 7 provides conclusions and recommendations for future research.

Chapter 2: Background and Literature Review

2.1. Rail stresses

A typical structure of a ballasted railway track (Figure 2-1) consists of two main components, i.e. superstructure and substructure. Rails, fasteners, and ties make up the superstructure, whereas the substructure known as the track's foundation comprises typically three layers, i.e. ballast, sub-ballast, and subgrade. The main duty of the rail track is to maintain a smooth surface for trains to ride on and to convert the concentrated wheel loads to a low pressure on the subgrades [14,27]. Further functions of the substructure can be found in the literature and it is beyond the scope of this study [27-30].

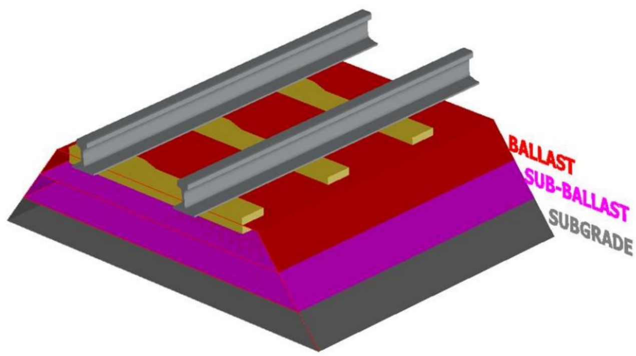

Figure 2-1. Typical layouts of a ballasted railway track

Rails undergo various stresses due to operational loading conditions and environmental factors. Generally, rail stresses are categorized and studied according to these effects individually. Besides the bending and shear stresses, contact stresses, thermal and residual stresses are the main stresses that rails are subjected to.

2.1.1. Operational bending and shear stresses

Moving wheel loads create vertical and lateral bending stresses on rails. Although vertical bending stresses are dominant, lateral bending stresses, longitudinal stresses are present in the rail. There are static, dynamic, and impact components that constitute a vertical wheel load [31]. The static load (which is the vehicle's gross weight) is magnified by the dynamic component that varies depending on the vehicle's speed and dynamic response of bogies to track geometries. Due to irregularities in the rail surface (dipped welds, joints) and wheel material (such as wheel flats, out of round), the impact load occurs and causes increases in static and dynamic components [11,31]. In addition to causing bending stresses, the vertical wheel load generates shear stresses which is the leading cause of rail web failure at bolt holes [32]. The lateral load, on the other hand, usually occurs at curves due to centrifugal forces, or even at a tangent track as a result of the vehicle's lateral dynamic behaviour such as hunting [12,33]. While lateral bending stresses mainly arise from the lateral loads, vertical tensile stresses along the rail web are also caused by these lateral loads [31]. In addition to causing bending stresses in rails, the movements of vertical and lateral wheel loads cause a reversal of these stresses from tension to compression in the rail head and from compression to tension in the rail base and vice versa [34].

Eccentrical wheel loads applied vertically at a distance from the shear centre of the rail create a torque about the centre of twist that contributes to the longitudinal stress in the rail head and base. In addition, the torsion in rail influences stresses in the web especially when the torque is accompanied by high lateral flanging forces [35].

2.1.2. Wheel-rail contract stresses

The magnitudes of contact stresses between the wheel and rail are significantly higher than other stresses in the rail. Generally, the normal contact stress can reach 1500 MPa in normal operation conditions [34]. These stresses can be predicted by Hertzian analysis whose theory is based on the assumption that the contact surface is continuous. When Hertzian analysis is used, the contact surface is modeled as an ellipsoid [12,33].

Together with wheel loads, maneuver forces due to traction, steering, and braking cause high contact stresses and increases in temperature within the small contact surface. Although having high magnitudes, contact stresses do not propagate significantly down the rail's depth. For this reason, their influence on crack propagations from the depth greater than 8-15 mm is negligible [36-38].

2.1.3. Thermal stresses

The rail/sleeper system is generally considered as a slender column whose buckling can occur under compression. Due to the varying temperature condition, a rail is subject to thermal loads as the constraints in the longitudinal direction prevent the rail from expansion and compression when the environmental temperature is different from the rail neutral temperature (RNT) [39]. RNT is a temperature at which the rail does not undergo any thermal stresses.

In modern railways, the risks associated with thermal stresses are a particular concern due to the use of continuous welded rail (CWR) track where rails are connected by welds rather than bolt connections. In a CWR track, the variations of thermal stresses can be high as there are no gaps that allow thermal expansions. However, a lower maintenance cost better ride quality are the main reasons CWT track is a better option compared to a conventional track whose rail joints and gaps are available to reduce the risks of thermal stresses [10].

As a CWR track's behaviour is somewhat similar to a long slender column, the structure is susceptible to buckling under compression [10]. High longitudinal compression in rails creates high pressure on the ballast until a buckling phenomenon occurs when the ballast's lateral resistance is exceeded [40]. Rail buckling can potentially lead to derailments, one of the leading concerns in railway transportation safety. Practically, it is recommended to install rails at a relatively high ambient temperature so that they are mostly in tension throughout the year [40-42]. While compressions in rails under hot ambient temperature are worrisome issues in railway safety, negative effects of tensile thermal stresses in extremely cold conditions on rail failures should not be ignored. Under cold temperatures, rails undergo excessive thermal-induced tensile stresses, and brittle failures can occur [10,12,42,43].

2.1.4. Residual stresses

Residual stress in a rail is formed by manufacturing and straightening processes such as rolling and non-uniform cooling [44]. The axial residual stresses are initially tensile in the rail head and base which are subsequently modified by service loads. These variations of the residual stresses affect rail fatigue. It is evidenced that tensile residual stress near the rail surface has direct relevance to crack growth and rail fracture [45]. Moreover, there is a significant difference in the residual stress in naturally hard and head hardened rails. Specifically, the values of residual stresses are higher in the head hardened rails [42,46]. Different methods for measuring the residual stresses include Moire interferometry, saw cut, ultrasonic testing, neutron scattering, etc. [47-49]. As the residual stresses vary under operational effects, measurements of their values generally give mixed results [10].

2.1.5. Contact shear stresses due to creep forces

The passage of wheels on rails also generates creep forces at the wheel/rail contact patch. The longitudinal creep forces are produced by the traction between rail and wheel. The traction changes when braking/accelerating are engaged or when the wheels approach a sharp curve. Transverse creep forces are also generated when the wheels are swaying on rails. Generally, the maximum shear stress due to the traction (creep) forces can occur within 2 to 4 mm below the contact surface [11,31,33].

2.2. Damage in rail steels and effects of track geometry

Under the effects of the above-mentioned stresses and environmental conditions, rail steels suffer from wear and rolling contact fatigue, the two common types of damage in rail steels [50,51]. Wear is described as the loss of steel material from the wheel-rail contact surface and is categorized according to factors causing the problem, e.g. abrasive wear, corrosive wear, and adhesive wear [51]. The load capacity of rail is significantly reduced due to wear as it reduces the cross-sectional area and moment of inertia of the rail. Fatigue refers to the strength of material being weakened due to extensive loading cycles. As a result of repeated overstressing of rail's surface and subsurface, cracks are initiated and propagate which leads to rolling contact fatigue (RCF) damage [52]. It was shown that a rail material with a higher wear rate has a lower rate of rolling contact fatigue damage [53]. It is because increasing wear volume also removes microcracks which reduces fatigue failures. Wear together with RCF defects poses a direct threat to rails [54].

It is not uncommon that railway lines, especially heavy haul lines are subjected to excessive loadings that cause plastic deformations in the rail material. By definition, plastic flows (or plastic deformations) occur when wheel/rail contact stresses exceed the material strength of the rail steel. Surface plastic deformations cause form changes on a rail (which directly impacts the service life of a track), whereas sub-surface plastic deformations contribute to the formations of wear flakes and fatigue cracks [55]. Moreover, the presence of track geometry defects increases dynamic wheel/rail loads, which in turn accelerates rail fatigue defects and thus reduces the rail's service life [56]. Comprehensive studies on effects of track geometry variations on dynamic wheel/rail loads and rail defects can be found in [27,57,58]. In the next section, definitions of track geometry parameters and their measuring methods are presented, which is followed by an overview of track quality assessments using track geometry parameters.

2.3. Track geometry measurements

Track geometry is the geometric layouts of a track in three dimensions in space. The measurements of track geometry are generally taken by locating the rails in the vertical and horizontal planes which are standardized in different standards and manuals to ensure safe passage of trains [28,59,60]. These parameters typically include gauge, crosslevel, superelevation, warp, alignment, and profile. Gauge is the distance between the gauge sides measured at 1.59 cm below the top of the two rails of a single railway line. Crosslevel is the difference in elevation between the two rails measured at top surfaces. Zero crosslevel is the intended design of a tangent track whereas the designated crosslevel is equivalent to the designated superelevation on a curved track. Superelevation is the designed vertical distance of the outer (high) rail above the inside (low) rail on a curved track. Warp is the difference in crosslevels at two points that are less than or equal to 62’ (18.9 m) apart. Alignment is the relative deviation of the rail’s position measured in the horizontal plane. The measurement of alignment can be taken as the maximum mid-offset of the rail from a 62’ (18.9 m) or 31’ (9.4 m) chord measured at the gauge side. Profile is the mid-offset of a 62’ (18.9 m) chord to the top surface of the rail measured on the longitudinal plane.

2.4. Track quality assessments

Generally, track performance is assessed by interpreting the track geometry data. Although the assessments can be detailed differently in different standards, two types of assessments, i.e. *track defects* and *Track Quality Index* (TQI) are generally followed [28,59-62].

Track geometry defects and TQI have a direct implication in track safety. It was found that track geometry defects are one of the main causes of derailments in the USA and Canada [2]. Out of 5146 freight train derailments from 2000 to 2014 in the USA, 394 cases are due to track geometry defects [3]. In Canada, 27% of main-track derailments in 2018 were due to track-related factors. This percentage is 38% considering the 10-year average from 2008 to 2018 [63]. Therefore monitoring the variations of track geometry at specific time intervals through the year is mandatory so that critical track geometry defects can be timely addressed and repaired to minimize any possibility of derailments due to track-related factors [59,60]. In addition, maintaining the margins of track geometry variations also helps to reduce the deteriorations of track components as the train-track dynamic interactions are greatly correlated to track geometry [64].

2.4.1. Track defects

Track geometry parameters are usually associated with their nominal values to represent ideal track conditions. However, track geometry measurements of a revenue track are most likely not equal to the nominal values. Therefore, the track geometry parameters are allowed to vary within a specific range while maintaining track safety. For instance, Transport Canada's rules respecting track safety (TC TSR) suggests any variations in the track geometry outside the allowable nominal ranges are consider defects [60]. According to TC TSR, there are five classes of track that are limited by the operating speeds (Table 2-1). The track geometry variations of each class of track are specifically regulated. For instance, Table 2-2 shows the lower and upper limits in gauge values for different classes. Moreover, TC TSR also recommends railway companies to adopt and customize these rules with more stringent requirements.

Table 2-1. Classes of track and maximum allowable operating speeds [60]

Class of track	The maximum allowable operating speed for freight trains is (mph)	The maximum allowable operating speed for passenger trains is (mph)
Class 1	10	15
Class 2	25	30
Class 3	40	60
Class 4	60	80
Class 5	80	95*

* For LRC Trains, 100

Table 2-2. Gauge' allowable limits [60]

Class of track	The gauge must be at least (inch)	But not more than (inch)
Class 1	55 3/4"	58"
Class 2	55 3/4"	57 3/4"
Class 3	56"	57 3/4"
Class 4 and 5	56"	57 1/2"

2.4.2. Track quality indexes

Overall, the term Track quality index (TQI) has been widely used in railway engineering and standards [28,62]. The most common types of TQI include Standard deviation (SD) of track geometry, combined standard deviation, and power spectral density (PSD) of track geometry.

Individual SD of track geometry is calculated for each parameter (such as gauge, alignment, etc.) defined over a track section, typically 200 m long. Individual TQI over track segments (or running standard deviation) significantly helps to refine the amount of track geometry measurements and facilitate simple assessments and comparisons between track segments. Besides the SD of track geometry, developments of new track quality indexes have been an objective of many related studies [65]. However, the newly developed TQIs are generally originated from the standard deviation of track geometry over a specific distance such as the Gauge Roughness Index, Superelevation Index, Surface Index [65].

Due to the stringent processing of assessing individual parameters of track geometry, TQI computed from combining the SD of different measurements of track geometry (such as alignment, cant, gauge, crosslevel, etc.) provides an overall assessment of track quality by a single parameter. In this regard, Sadeghi and his colleagues are well-known for their extensive work in developing different types of TQI for track quality assessments [66-69]. Another reason for a combined different values SD is to emphasize the effects of simultaneous track irregularities on vehicle behaviour. For instance, the same level of alignment at curved and tangent tracks is associated with different responses in the vehicle and lead to different potential hazards. In this case, evaluating track quality by assessing individual track geometry measurements would not be accurate [70];

2.4.3. Power spectral density (PSD)

PSD of a track geometry parameter provides the energy of the measured signal with respect to its frequency, which can be used for track quality assessment. Specifically, the features of a track system that cause an increase in the PSD at a specific frequency can be observed easily in the PSD plot. For instance, irregularities and defects such as welds, joints that recurrently present in the track data can be easily tracked by PSD plots. The use of PSD for track quality evaluations is widely acknowledged and standardized in many countries such as the USA, China, Germany, Britain, and France [71-74]. the following sections provide details formulation of the four commonly used PSD standards.

2.4.3.1. The FRA PSD standard [71]

The US Federal Railroad Administration (FRA) classifies railway tracks into Class 1 to 6 for normal tracks and Class 7 to 9 for high speed tracks. The single-sided PSD functions for random track irregularities associated with different classes are described as below:

PSD of vertical profile:

$$S_v(\Omega) = \frac{0.25 \cdot A_v \cdot \Omega_c^2}{\Omega^2 \cdot (\Omega^2 + \Omega_c^2)} \tag{2-1}$$

PSD of lateral alignment:

$$S_{al}(\Omega) = \frac{0.25 \cdot A_a \cdot \Omega_c^2}{\Omega^2 \cdot (\Omega^2 + \Omega_c^2)} \tag{2-2}$$

PSD of gauge and superelevation:

$$S_{gauge/sup}(\Omega) = \frac{A_a \cdot \Omega_c^2}{(\Omega^2 + \Omega_c^2) \cdot (\Omega^2 + \Omega_s^2)} \tag{2-3}$$

where,

$S_v(\Omega)$:	PSD of track vertical profile, $cm^2/(rad/m)$
$S_{al}(\Omega)$:	PSD of track alignment, $cm^2/(rad/m)$
$S_{gauge/sup}(\Omega)$:	PSD of track gauge and superelevation, $cm^2/(rad/m)$
Ω:	Spatial wavenumber, rad/m
Ω_c, Ω_s:	Critical wavenumbers, rad/m
A_v, A_a:	Roughness coefficients, $cm^2 \cdot rad/m$

The spatial wavenumber is the number of wavelengths per unit distance, which means $\Omega = 1/\lambda$. It is recommended that the FRA's PSD functions are valid within the wavelength from 1.524 m to 304.8 m. The parameters in equations (2-1) to (2-3) are defined in Table 2-3

Table 2-3. Coefficients for the FRA's power spectrum density function [71]

Class of track	A_v (cm^2·rad/m)	A_c (cm^2·rad/m)	Ω_c (rad/m)	Ω_s (rad/m)
Class 1	1.2107	3.3634	0.8245	0.6046
Class 2	1.0181	1.2107	0.8245	0.9308
Class 3	0.6816	0.4128	0.8245	0.852
Class 4	0.5376	0.3027	0.8245	1.1312
Class 5	0.2095	0.0762	0.8245	0.8209
Class 6	0.0339	0.0339	0.8245	0.438

2.4.3.2. German PSD standards

The German PSD of track geometry is commonly used in European countries and it can generate track irregularities with the wavelength varying from 2.5 m to 100 m [73].

PSD of vertical profile:

$$S_v(\Omega) = \frac{A_p \cdot \Omega_c^2}{\left(\Omega^2 + \Omega_\gamma^2\right) \cdot (\Omega^2 + \Omega_c^2)} \tag{2-4}$$

PSD of lateral alignment:

$$S_{al}(\Omega) = \frac{A_a \cdot \Omega_c^2}{\left(\Omega^2 + \Omega_\gamma^2\right) \cdot (\Omega^2 + \Omega_c^2)} \tag{2-5}$$

PSD of gauge and superelevation:

$$S_{gauge/sup}(\Omega) = \frac{A_p \cdot \Omega_c^2 \cdot a^{-2} \cdot \Omega^2}{\left(\Omega^2 + \Omega_\gamma^2\right) \cdot (\Omega^2 + \Omega_c^2) \cdot (\Omega^2 + \Omega_s^2)} \quad (2\text{-}6)$$

where:

$S_v(\Omega)$:	PSD of track vertical profile, $cm^2/(rad/m)$
$S_{al}(\Omega)$:	PSD of track alignment, $cm^2/(rad/m)$
$S_{gauge/sup}(\Omega)$:	PSD of track gauge and superelevation, $cm^2/(rad/m)$
Ω:	Spatial wavenumber, rad/m
$\Omega_\gamma, \Omega_c, \Omega_s$:	The cut-off wavenumbers, rad/m
A_v, A_a:	Roughness constants, $m^2 \cdot rad/m$
a:	the half-distance of the wheel rolling circle ($\cong$ 0.75 m)

The parameters in equations (2-4) to (2-6) are given in Table 2-4.

Table 2-4. The German track PSD parameters

Parameters	A_a (10^{-7} m^2·rad/m)	A_p (10^{-7} m^2·rad/m)	Ω_c (rad/m)	Ω_γ(rad/m)	Ω_s(rad/m)
Low irregularities	2.119	4.032	0.820	0.0206	0.438
High irregularities	6.125	10.80	0.820	0.0206	0.438

2.4.3.3. The Chinese PSD standard

The Chinese Academy of Railway Science (CARS) provides one of the most detailed standards of track geometry spectra. Track quality is evaluated based on the lower and higher limits of individual PSDs of track geometry parameters. In addition, the PSDs are different for each class of track which is defined based on the operational speed, i.e. 200 km/h, 160 km/h, and 120 km/h [72]. When evaluating the spectra of a track segment, the closer the spectrum to the lower limit, the better quality the track has and vice versa.

The CARS's single-sided spectrum of track geometry is defined based on six parameters as below:

$$S(f) = \frac{af^2 + b}{cf^2 + df^4 + ef^2 + k} \quad (2\text{-}7)$$

where $S(f)$ is the track irregularity PSD ($mm^2/(1/m)$), f is the spatial frequency in 1/m. The spectral coefficients a, b, c, d, f, k for different speed limits can be found in [72].

2.4.3.4. The French PSD standards

The National Society of French railways (SNCF) provides the reference for PSD functions of track profiles that vary within the range from 2 m to 40 m. The PSD model is given below:

$$G_{rr}(n) = \frac{A}{\left(1 + \frac{n}{n_0}\right)^3} \tag{2-8}$$

where, A is the surface roughness coefficient, which is $308\times0.509\times10^{-6}$ for low roughness and $308\times1.790\times10^{-6}$ for high roughness; $n_0 = 0.0489$ 1/m; n is the spatial frequency (1/m).

Figure 2-2 demonstrates the PSDs of vertical profiles generated by different standards. It should be noted that although the PSD functions are different in these standards, the wavelengths within 2 to 40 m is always the focus as they are directly related to the safety and reliability issues of a track system [62].

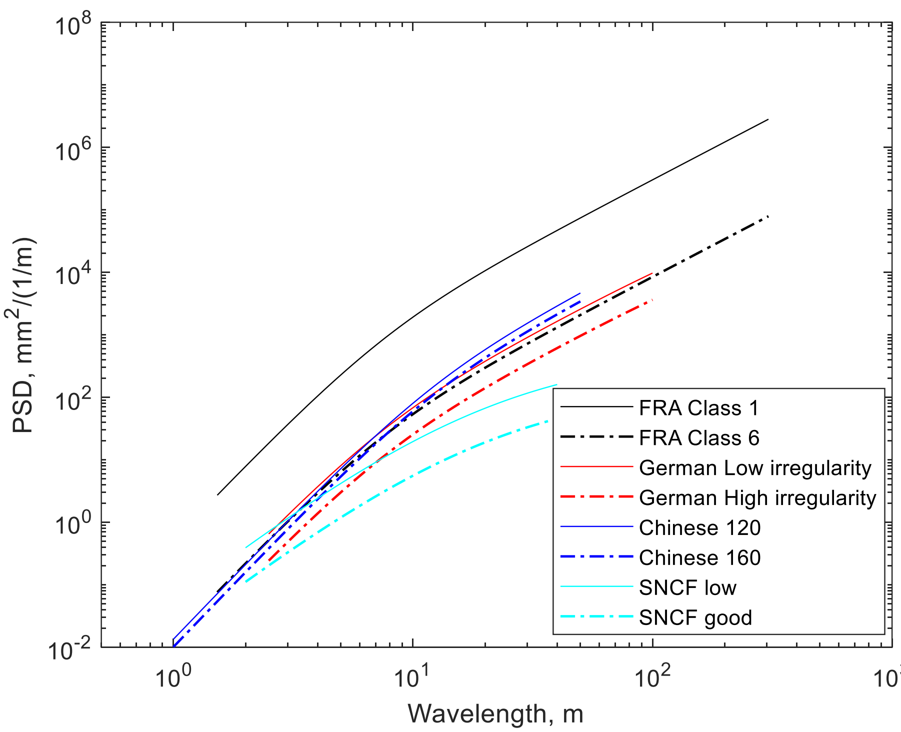

Figure 2-2. Comparison of different PSD's specifications (vertical profile)

2.5. Track modulus

Track foundation modulus (generally known as track modulus) describes the vertical stiffness of the track foundation. It is defined as the vertical supporting force per unit length of rail per unit deflection [75]. In other words, it is the coefficient of proportionality between vertical contact pressure (at the surface between the rail base and the track foundation) and rail deflection [76]. Track modulus is related to fastening systems, ties, and substructure conditions, and is not affected by the properties of the rail component [76-79]. The variation of track modulus depends on the formation of track foundation such as soil properties and characteristics of subgrade layers. It can rapidly change at transition locations along the track such as switches, turnouts, crossing, locations between embankments and bridges, transitions between ballasted and slab tracks [80-84].

Track modulus is an important parameter for evaluating track performance. It is advised that a desirable track modulus should be within a range that is not too low or high [75,81]. A stiff track would cause excessive vibrations and increase dynamic effects on the wheel/rail contact surface, where rolling contact fatigue (RCF) and wear can further develop [11,26,85]. On the other hand, soft track results in excessive deflections under wheel loads, which leads to unstable conditions. The quality of the track's foundation is categorized based on different ranges of track modulus whose variations should be small to prevent large deformations (Table 2-5). According to AREMA manual, to avoid rail fatigue in bending and unstable ballasts due to excessive deflection, vertical rail deflection should be smaller than 6.35 mm (1/4 in). To prevent wheel-rail contact fatigue due to hard supports, wear of ties, and ballast, vertical rail deflection should be desirably greater than 3.175 mm (1/8 in) [86].

Table 2-5. Recommended ranges of track modulus

Track modulus, MPa (psi)	**Quality**	**References**
< 14 (2,000)	Poor (not recommended)	[11,75]
14 (2,000) to 28 (4,000)	Average	[11,75]
28 (4,000) to 34 (5,000)	Good	[11,75]
34 (5,000) to 69 (10,000)	Optimum	[11,75,87,88]
> 69 (10,000)	Not recommended	[11,75,87,88]

2.6. The role of track stiffness measurements for track maintenance decisions

Understanding the vertical stiffness of the track foundation (track modulus), or the vertical stiffness of the entire track structure (global track stiffness) is important for track maintenance purposes [75]. Global track stiffness varies in both spatial and frequency domain and depends greatly on the applied load and track's location [14]. The variations of global track stiffness directly affect wheel/rail interactions and degradations of the track structure. Therefore, continuous measurement of vertical track deflections (or stiffness) together with an appropriate data interpretation method enables engineers to optimize the maintenance activities [77]. There are three main purposes for the use of vertical track stiffness measurement systems: 1 – Indicate the root causes of track performance issues; 2 – Facilitate the decision for upgrading a railway line (e.g. increasing speed and axle load); 3 – Monitor revenue and newly built tracks.

Generally, track performance is assessed by the quality of track geometry. However, when concerns associated with track geometry irregularities, ballast, and sub-ballast problems are not adequately addressed, the track deflection measurements can be an additional tool to detect the root causes of the problems [85]. Typical applications of track stiffness measurement systems include identifying foundation-related causes and environmental effects on track performance.

One of the main goals of using vertical track stiffness measurement systems is to assess the capability of a railway line to sustain a higher axle load and speed. This task is challenging as knowledge about track performance's history is limited especially considering the high mileage of railway network levels. Although track geometry measurements and visual inspections are available, the subgrade conditions are often unknown or can be only partially assessed by standstill methods [79,89]. As continuous measurements of track deflections are available, it is possible to continuously measure the track stiffness to locate the track sites that required substructure enhancement or further investigations.

One of the concerns during the design and operations of a track is the desired track deflection and the allowable variations of track stiffness for an optimal condition [90]. In the literature, different studies were conducted on the contribution of track stiffness on track deteriorations. For instance, Lopez Pita et al. [91] concluded that track sections suffering from rapid deteriorations are corresponding to short rigid structures such as culverts, bridges, and the transition zones between bridges and embankments. With the availability of continuous track stiffness measurement systems, it is possible to evaluate the track stiffness values and variations so that not only newly built tracks can be verified but also in-service tracks can be well monitored.

2.7. Continuous track stiffness measurement systems and their applications

Recently, track-side (or standstill) and on-board systems are the two common types of measurement systems for railway monitoring. In track-side monitoring systems, measurement devices are installed at specific locations on the track's sides for wheel-rail contact loads evaluation, bogie performance, rail's deflection, and track performance [77,88,92]. A major disadvantage of track-side systems is only specific locations along the track are measured and thus it is impossible for long-distance measurements. On-board monitoring systems, on the other hand, have been introduced around two decades ago [9]. The main objective of such systems is to detect wagon, wheel, rail local defects, and failures in suspension systems. Measuring sensors are generally installed on axle boxes, bogies, and car bodies to primarily acquire vibration signals for fault detections [93-95]. Although axle box sensors have been widely used for track irregularities and RCF defects, their service life is limited due to the direct impacts of wheel-rail impact loads [96]. In addition, railway structural health monitoring systems can be divided into systems for railway vehicle monitoring and track performance monitoring. In the context of this Ph.D. study, continuous track stiffness measurement systems for track performance monitoring are of interest. There are two main approaches to the development of those systems. One system collects the vertical track deflection using dynamic measurements on a single axle, the other outputs relative vertical track defection using indirect methods such as image and laser-based techniques. Available systems include those developed in China, the USA, and European countries [7,9,20,26,97], which are discussed in the following sections.

2.7.1. China academy of railway sciences (CARS) system

China Academy of Railway Sciences (CARS) is one of the first institutes introducing the concept of continuous track stiffness measurements. In 1997, Wangqing et al. [9] proposed the design of a vehicle for track elasticity measurements. As shown in Figure 2-3, the chord measurement method is used to measure the deflections at the measurement wheels in the heavy car and the light car at the rear. The total load exerted by the heavy car can be adjusted from 150 to 250 kN to simulate the influence of different loads on the measured deflections. The light car applied a load of 40 kN to the track to close void deflections due to the clearance between the rail and sleeper, and between sleeper and ballast as well (Figure 2-3 (a)).

As shown in Figure 2-3 (b-c), the wheel deflection under either light or heavy car is a combination of the contact deflections (y_{KH}, y_{KH}) and y_2, i.e. the deflection due to rail surface irregularities (y_1) and hidden gaps between rail, sleeper, and ballast (y_0). The elastic stiffness is measured as:

$$K = \frac{\Delta P}{\Delta y} = \frac{P_H - P_L}{y_{KH} - y_{KL}} = \frac{P_H - P_L}{y_H - y_L} \tag{2-9}$$

where P_H, P_L are the wheel loads due to the heavy and light cars; y_{KH}, y_{KL} are the deflections due to the track stiffness only; y_H, y_L, are the total measured deflections under P_H, P_L loads.

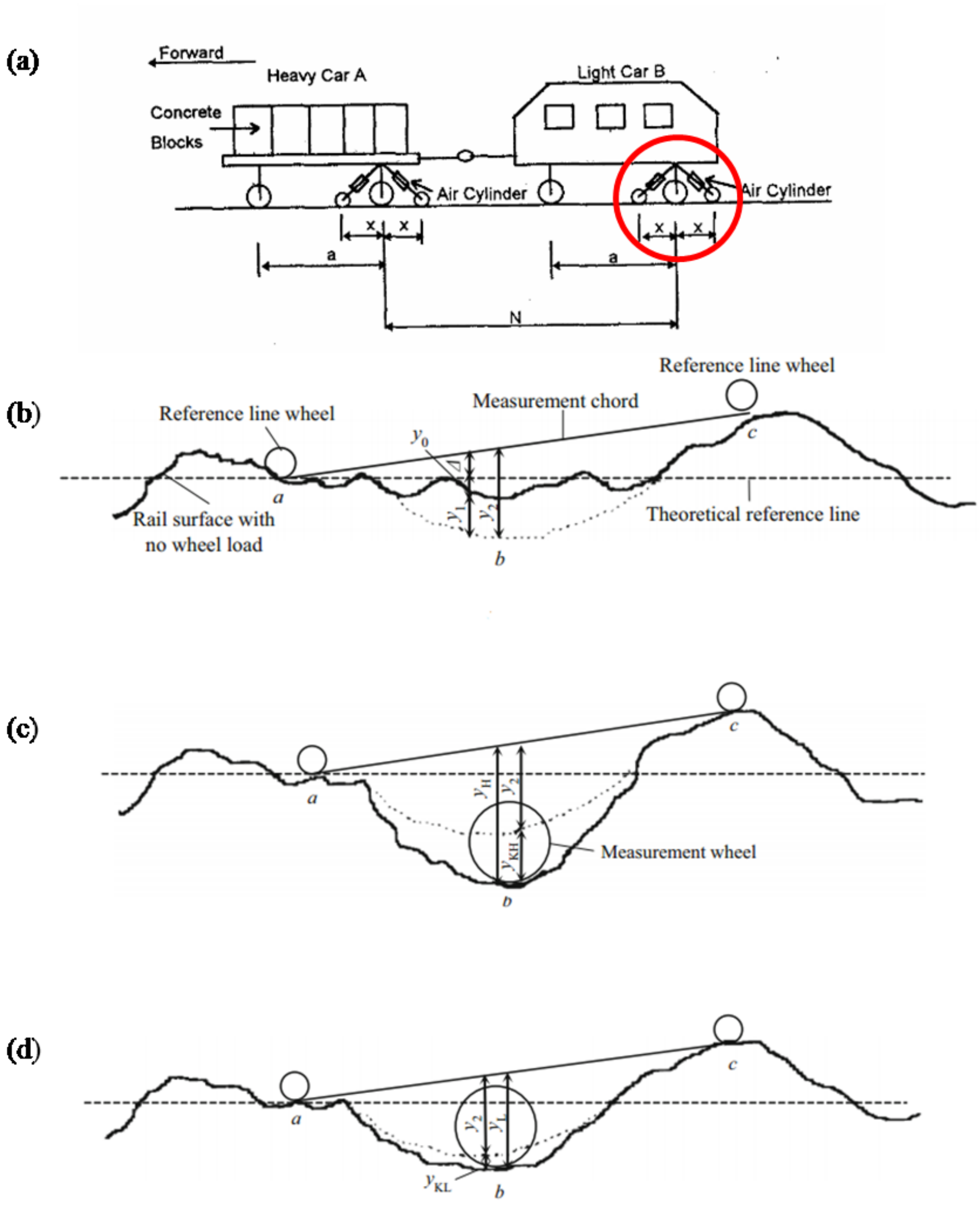

Figure 2-3. Measurement principle of the CARS system: (a) the measurement system; (b-d) the magnified deflections of the measurement wheels under no load, light car, heavy car (adapted from [98])

2.7.2. SBB track deflection measurement wagon

A deflection measurement wagon was developed by the Swiss Federal Railways (SSB) [99] to continuously measure track deflections at 10-15 km/h speed. The system consists of an unloaded wagon and a heavy wagon with the axle load being 20 tonnes (Figure 2-4). An incremental sensor (Heidenhain LS 220) and a digital display unit are the main instrumentation of the SSB system. To obtain the deflection due to the load only, the unloaded deflection under the unloaded wagon is subtracted from the loaded deflection under the heavy wagon. It is also recommended to filter the measured deflections by a low pass filter with the cut-off wavelength from 10 m to 20 m. With this configuration, the system can collect data every 5 cm with the accuracy levels varying around ± 0.2 mm.

It was shown that the SSB system can be used to identify the stiffness variations in long wavelengths corresponding to variations of soil properties, bridges, and the influence of USP (under sleeper pad) [99]

Figure 2-4. The SBB track deflection measurement wagon (adapted from Reference [99])

2.7.3. Track loading vehicle by Transportation Technology Center, Inc. (TTCI) in Pueblo, Colorado (TTCI)

The Transportation Technology Center Inc. (TTCI) developed a track loading vehicle to measure vertical track deflections under standstill loads as well as moving loads with a speed up to 16 km/h [7]. As shown in Figure 2-5, the system consists of a heavy car (i.e. the track loading vehicle), an empty tank car. The track loading vehicle (TLV) is equipped with a fifth wheelset that can hydraulically exert a range of loads (lateral and vertical) from 4 to 267 kN. In order to eliminate the effects of track geometry on the final readings, two sets of track deflections are measured simultaneously, e.g. a loaded profile due to the wheel loads of the TLV and an unloaded profile under the empty tank car weighting at 62 kN. Finally, the unloaded profile is subtracted from the loaded profile to get the track deflection due to the applied loads only. It should be noted that noncontact laser camera sensors are used to record the vertical track deflections.

Figure 2-5. The TTCI system: (a) the track loading vehicle: (b) A closer look at the fifth wheelset at the center of the vehicle (*http://www.drgw.net/trips/report.php?tr=TTCI.3* [100])

The TLV was extensively tested on revenue tracks to verify its capability of monitoring substructure conditions [101,102]. It was shown that the system is able to quantify the vertical track supports such as identifying the locations with abrupt changes in track stiffness (e.g. bridge approaches and soft subgrades). It was recommended that the system can be used for two main tasks one of which is assessing existing tracks for upgrading the operating speeds and axle loads. The second task is to provide a tool for investigating the degradations of track strength which helps to develop an optimized maintenance strategy.

One of the first applications of TLV was conducted on revenue service extensively [7]. The variations of the deflection profiles clearly indicated the difference between strong and weak tracks. In order to obtain the dynamic track modulus and minimize the effects of track geometry, two runs were acquired at different loads. The difference between the two deflection profiles was used to compute the dynamic track modulus. However, it should be noted that the train speed must be kept relatively the same between the two runs which may be difficult to maintain in real-life conditions.

The data measured by TLV was further verified by the use of cone penetration tests (CPT) [101]. It was shown that the sublayer conditions identified by the CPT further explained the large variations of the TLV stiffness profile. This evaluation further addressed the usefulness of continuous track stiffness measurement systems locating problematic areas where detailed tests such as CPT can be employed to investigate the substructure conditions. Similar to the previous study, the effects of track geometry were not clearly addressed. For instance, the difference between the two deflection profiles was expected to remove the effect of track profile whereas the effects of other types of track geometry were not verified.

2.7.4. The Swedish rolling stiffness measurement vehicle (RSMV)

Swedish Railways Administration (Banverket) and Royal Institute of Technology (KTH) developed a new rolling stiffness measurement vehicle (RSMV) to measure quasi-static and dynamic vertical track stiffness that is subsequently used for evaluating the track's degradation [103].

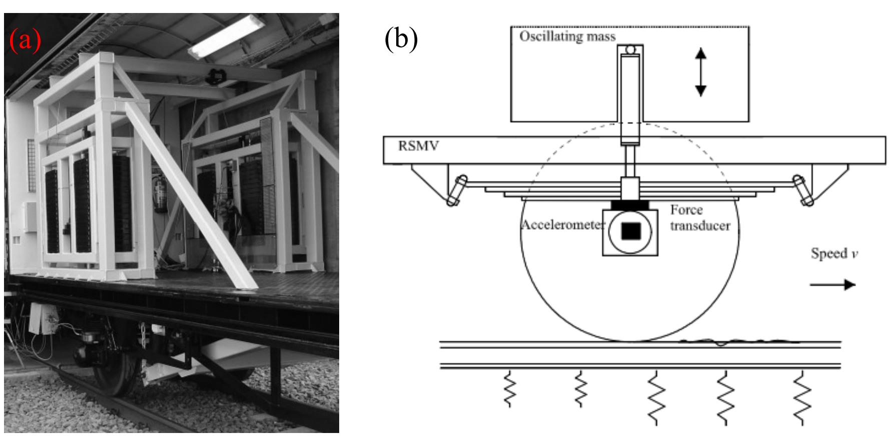

Figure 2-6. The RMSV system: (a) the system's setup; (b) the schematic side view (adapted from Reference [103])

As shown in Figure 2-6, the RMSV system is built on a two-axle freight wagon whose main components are two oscillating masses above the wheel axle, an accelerometer, and a force transducer installed at the axle box for recording the vibration. The oscillating masses (4,000 kg) are used to dynamically excite the track via the wheel axle. The system can apply a static axle load of 180 kN or higher, a dynamic axle load up to 60 kN. With the configuration, the system can measure track dynamic stiffness up to 50 Hz. The measurement can be taken at high speeds (up to 50 km/h) during which the track is excited by 1 to 3 simultaneous sinusoidal sources of excitations. Detailed investigations about the track stiffness can also be performed at a slower speed (≤ 10 km/h) with the source of excitation being artificial noise.

The RMSV has been deployed in revenue tracks to validate its effectiveness in identifying the global track stiffness [26,97,103,104]. For instance, Berggren et al. [104] conducted numerical simulations and field measurements to verify the effectiveness of the RMSV in measuring the dynamic properties of railway tracks below 50 Hz. The results showed that the thickness of embankment and soil could be estimated from the dynamic stiffness measurements. It was also shown that the information given by the dynamic stiffness measurements agrees well with that from the Ground Penetration Radar (GPR) data.

Statistical properties of track stiffness were examined by means of statistical properties of dynamic track stiffness values measured by the MRSV [26]. Three typical kinds of Swedish track were examined by cumulative distribution functions (CDF) of the corresponding dynamic track stiffness measurements. It was shown that the difference in the three types of track and the stiffness variations can be observed from the CDFs. However, the accuracy of displacements computed by double integrating the axle acceleration, effects of other factors such as track geometry and wheel out-of-roundness remain the major concern in the use of MRSV. For instance, track geometry variations can cause a significant impact on the acceleration response which can lead to inaccurate displacements. Without, a sound understanding of the impacts of these factors on the recorded signals, any conclusions about the vertical track stiffness cannot be fully justified.

2.7.5. Portancemetre vehicle

The Portancemetre vehicle was developed by the Centre d'Expérimentation et de Recherche and the Engineering Department of SNCF (National Society of French railways) to measure the dynamic track stiffness [6,105]. Having a similar measurement concept as the RMSV, the Portancemetre vehicle includes an oscillating wheel axle with a suspension mass (Figure 2-7). The system is instrumented with two accelerometers, a phase sensor for synchronization, and an incremental distance encoder for traveling distance measurements. The vehicle can apply a static load varying between 70 and 120 kN and a dynamic load that can reach 70 kN. The Portancemetre vehicle was validated with in-service tracks and it was shown that the system is able to measure the dynamic stiffness with frequencies up to 35 Hz [106]. However, it was not mentioned how track geometry and irregularities of the rail surface influence the recorded force and displacements although the system applies a similar concept as that of RMSV.

Figure 2-7. The Portancemetre system (inside the red square) (adopted from Reference [106])

2.7.6. The MRail system

Under the sponsorship of the Federal Railroad Administration (FRA), a continuous track stiffness measurement system that is commercially known as MRail system was developed at the University of Nebraska-Lincoln [8,21,107]. The system consists of two laser lines and a camera system that measures the relative deflection (Y_{rel}) at 1.22 m from the nearest wheel. Y_{rel} is the distance between the rail surface and the rail-wheel contact plane. Further details about the system's specifications are discussed in Chapter 3. One of the practical advantages of using the MRail system is that it can measure the vertical track deflections at normal to full train speeds.

One of the first applications of the system on a real-life track showed that the preliminary analysis of Y_{rel} clearly indicates the track issues such as muddy crossings, crushed rail heads, broken rails, etc. In addition, statistical properties of Y_{rel} i.e. mean and standard deviation were computed for track assessments [108,109]. Moreover, by using the Winkler model that assumes a rail as a beam on continuously constant supports, the relationship between Y_{rel} and rail bending stresses was established and subsequently tested with measured data [19]. It was shown that the differences between the estimated rail bending strain (from Y_{rel}) and the actual values at two locations were only 13.7% and 12.2%. An early study about the effects of track geometry on the measured Y_{rel} was first conducted by Lu et al. [21]. In the study, the applicability of using Y_{rel} for locating track segments with problematic stiffness and the evolution of Y_{rel} measurements taken on the same track at different time intervals were first presented. In addition, the effects of track geometry on the measured Y_{rel} were examined by considering vertical track profile only. From the numerical simulations, it was concluded that only "extreme track geometry variations" can cause errors in the Y_{rel} measurements.

In Canada, the MRail system has been employed for track performance evaluations. Both numerical and experimental studies were conducted to verify its effectiveness. Fallah Nafari et al. utilized different finite element models (FEM) to examine the track modulus variations using numerical Y_{rel} signals [110]. As the MRail system was originally developed based on the concept of Winkler model that assumes a track on continuous supports with constant track modulus, the study considered the fact that track modulus varies along the track. By using statistical properties of the simulated Y_{rel} data and curve-fitting approaches, the track modulus average was estimated. However, the variation of track modulus was not effectively estimated from Y_{rel} especially the variation over a relatively long track section. Another application of using Y_{rel} for rail bending moment estimations was also studied from the FEM models [25,111]. The relative track deflection (or Y_{rel}) and the corresponding maximum positive and negative rail bending moments were first extracted from numerical simulations. The study showed that there was a strong correlation between Y_{rel} and positive bending moments. However, the negative bending moments were not estimated successfully from Y_{rel} using statistical analysis and curve-fitting approaches. The methodology was also validated with field data [22]. Measured Y_{rel} was used to estimate the tensile strain using a regression function that was built from a numerical study. Subsequently, the estimation accuracy was evaluated by comparing the estimated values with those measured by strain gauges. The results showed that Y_{rel} can be used to assess rail bending stresses.

MRail system was also used for quantitatively evaluating Canadian track subgrade conditions. Roghani et al. [112] investigated the MRail measurements (i.e. Y_{rel}) to map their variations to the properties of soft foundations under the railway line. Y_{rel} data collected over 12,000 km of track was first processed by moving average filters to remove short-wavelength components (which corresponds to the surface irregularities) and used to assess the subgrade conditions (which occurs at long wavelengths). It was concluded that filtered Y_{rel} is a representation of subgrade conditions.

In another study, two indices were derived from Y_{rel} to represent the subgrade stiffness and its variations for track condition assessments. Historical records of the track roughness show strong correlations with the derived indices whose high variations correspond to locations with geometry defects [113]. A different study was conducted to examine the changes of Y_{rel} measurements that were taken before and after major maintenance to improve track performance [24]. The track upgrades included replacing 49.6-kg/m (100-lb/yd) bolted rail to 57-kg/m (115-lb/yd) continuous welded rail (CWR), embankment reconstruction, and geogrid placement. The moving average of Y_{rel} and its first-order difference are capable of quantifying the changes in track modulus due to the maintenance activity. In the next section, a brief review of blind source separation is introduced as it is a potential tool for analyzing MRail data.

2.8. Blind source separation techniques

Obtaining separated source signals from their mixed observations without a priori knowledge of the mixing mechanism and sources is referred as blind source separation (BSS). The principle of BSS is demonstrated in Figure 2-8. In general, depending on the physical meaning of the observations (e.g. speech signals or vibrational signals), the mixing mechanism can be: (1) instantaneous mixing and (b) dynamic or convolutive mixing. In both cases, the aim of BSS is to define the de-mixing matrix and recover the original sources using the information from the observations only.

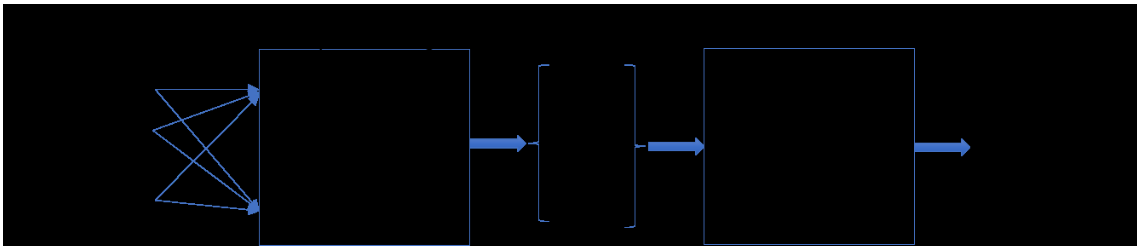

Figure 2-8. Demonstration of BSS

Instantaneous mixing is a common aspect of BSS where all sources are recorded instantly with no time lag and different intensities. The problem can be mathematically expressed as:

$$\begin{aligned} \mathbf{x} &= \mathbf{A}\mathbf{s} \\ \hat{\mathbf{s}} &= \mathbf{W}\mathbf{x} \end{aligned} \tag{2-1}$$

where

- $\mathbf{s} = \{s_i\}$ $i = 1, 2, \ldots, n_s$ the number of sources
- $\mathbf{x} = \{x_j\}$ $j = 1, 2, \ldots, n_m$ the number of sensor measurements (observations)
- $\mathbf{A} \in R^{n_m \times n_s}$ is the instantaneous mixing matrix, and $\mathbf{W} \in R^{n_s \times n_m}$ is the de-mixing matrix.

Depending on the number of sources and observations, BSS can be categorized as determined case ($n_m = n_s$); underdetermined case ($n_m < n_s$); or overdetermined case ($n_m > n_s$). These cases can be solved by a variety of BSS algorithms which follow three main categories: (1) second order or higher order statistics of signals; (2) sparse blind source separation; (3) tensor-based decomposition for BSS. The first category is common for determined and overdetermined case ($n_m \geq n_s$) where second order statistics blind source identification (SOBI), and higher order statistics independent component analysis (ICA) are mainly used for BSS [114-116]. On the other hand, spare blind source separation is based on transformations of the observations in time, frequency, and time-frequency domain [117,118]. The third algorithm refers to multi-linear algebra methods to solve BSS problem such as parallel factor (PARAFAC) decomposition. PARAFAC algorithms are valid for both underdetermined and overdetermined BSS problems [119-122].

A special variant of BSS, i.e. single channel blind source separation (SCBSS), is formed when only one observed mixture is available. Its applications include speech processing, communications, etc. In general, the source signals are randomly mixed by a mixing matrix (with different weights), and the summed mixture is recorded by a sensor or receiver. Vertical track deflection data is essentially a single mixture and SCBSS techniques can be a potential tool to analyze the data for track evaluations. Several methods were proposed to solve the SCBSS problem by converting a single channel problem to a pseudo multi input multi output (MIMO) problem. Ma et al. [123] employed Singular spectrum analysis (SSA) to decompose a single mixture to multiple signals which were then inputted to a fast BSS algorithm to recover the source signals. Wavelet decomposition and FastICA have been combined to recover up to 3 original sources from a single mixture [124]. Another method using ensemble empirical mode decomposition (EEMD) and ICA was presented by Guo et al. [125]. First the single channel observation was decomposed into a number of intrinsic mode functions (IMFs). Principal component analysis was subsequently used to extract several components of IMFs for the inputs of ICA algorithm. Other techniques such as slope EEMD, variational mode decomposition, shift-invariant spare coding, and non-negative matrix factorization were also employed in different studies to solve the SCBSS problem [126-131].

2.9. Summary and discussion

A review of the related literature was presented in this chapter. First, dominant stresses in rail such as bending, contact, thermal and residual stresses were reviewed which was followed by damage mechanism of rail materials. The impact of track geometry on rail stresses was also presented. Then, assessments of track quality using track geometry measurements were presented. The assessment methods that use standard deviation and power spectrum density function of track geometry measurements were described. Next, an overview of track modulus and its effects on rail deflections, stresses, and track structure degradations was discussed. It was followed by detailed review of continuous track stiffness measurement systems. Finally, a brief introduction about BSS and SCBSS algorithms were given and an idea of how track stiffness evaluations would be a potential application of SCBSS was discussed. According to the literature review, there are concerns about the systems' effectiveness and the effects of track geometry variations the measurements which partially defines the purpose of this doctoral research:

1. The effects of track geometry on measured data were not fully investigated. As most continuous track stiffness measurement systems are at their early deployment stage, there are limited efforts for considering track geometry effects on the measured data. For

instance, the numerical study conducted by researchers at the University of Nebraska Lincoln concluded that only large vertical track geometry variations can affect the measurements [21]. This was contrary to what has been found by Mehrali et al. [132] where the authors showed that track alignment has more effects on the measured data. However, a sound explanation for this relationship was not given as the findings were found based on data mining techniques. Therefore, an in-depth investigation of track geometry effects on a continuous track stiffness measurement system is worth conducting so that their effectiveness of track stiffness measurement systems is verified.

2. Most techniques utilized to analyze measured VTD data are based on its statistical properties. Cumulative distribution functions of VTD collected by different systems have been mainly used for assessing track conditions [7,26,133]. However, there are limited efforts in refining the raw measurements before they are used for this purpose. This study aims to employ blind source separation and other advanced techniques to facilitate better methodologies for track stiffness evaluations so that more accurate and more detailed information can be extracted from the measurements. It is arguably the first time that blind source separation techniques are investigated for analyzing VTD measurements.
3. Lack of clear demonstrations of how continuous track stiffness measurement systems are more superior than other systems. For instance, Read and Plotkin questioned the novelty of the track stiffness measurement systems over track geometry vehicles and ground penetrating radar systems [134]. Although many studies have been conducted to justify the effectiveness of continuous track stiffness measurement systems, further investigations are worth conducting to validate the applicability of these systems. For instance, it is promising that these systems can potentially reveal track geometry variations in addition to the track stiffness. The current doctoral research intends to establish new methodologies that employ measurements of a specific track stiffness measurement system to effectively assess track stiffness variations and rail bending moments while giving useful information about track geometry.

Chapter 3: Continuous Evaluation of Track Modulus from a Moving Railcar Using ANN-Based Techniques[1]

3.1. Overview

Track foundation stiffness (also referred to the track modulus) is one of the main parameters that affect the track performance, and thus, quantifying its magnitudes and variations along the track is widely accepted as a method for evaluating the track condition. Over the past decades, the train-mounted vertical track deflection measurement system developed at the University of Nebraska – Lincoln (known as MRail system) appears as a promising tool to assess the track structures over long distances. Numerical methods with different levels of complexity have been proposed to simulate MRail deflection measurements. These simulations facilitated the investigation and quantification of the relationship between vertical deflections and track modulus. In this study, finite element models (FEMs) with stochastically varying track modulus have been used for the simulation of the deflection measurements, the relationship between the measured deflection and track modulus averages and standard deviations are quantified using artificial neural networks (ANNs). Different approaches available for training the ANNs using FEMs data sets are discussed. It is shown that the estimation accuracy can be significantly increased by using ANNs. Especially, when the estimations of track modulus and its variations are required over short track section lengths, ANNs result in more accurate estimations compared to the use of equations from curve fitting approaches. Results also show that ANNs are effective for the estimations of track modulus even when the noisy datasets are used for training the ANNs.

3.2. Introduction

It is widely accepted that track modulus and its variations are indicators of subgrade conditions [75,77,80,82]. Track modulus is a measure of the vertical stiffness of the rail foundation and is defined as the ratio of the vertical supporting force per unit length of rail to the vertical deflection [75]. A practical way to assess track modulus is to measure rail deflection under specified loads

---

[1] A version of this chapter has been published in Vibration, Special Issue: Inverse Dynamics Problems as N.T. Do, M. Gül, S.F. Nafari, Continuous Evaluation of Track Modulus from a Moving Railcar Using ANN-Based Techniques. *Vibration* 3 (2020). doi:10.3390/vibration3020012.

[20,23,135]. Measured deflections can be correlated to the track modulus using mathematical equations. Two methods are available to measure rail deflections: trackside measurement techniques and on-train approaches. Trackside measurement techniques are used to measure the rail deflection at specific locations under specified static loads or moving loads [98]. Although these techniques provide accurate estimations of track stiffness, they are laborious, time-consuming especially when multi-point measurements are required. On the other hand, on-train measurement systems allow the measurement of rail deflections over long distances and thus provide an overall evaluation of the entire railway network [7,8,107,136-138]. Comprehensive analysis is typically needed to investigate the relationship between deflection measurements from on-train systems and track modulus [104,139].

The Real-time Vertical Track Deflection Measurement System (known as MRail System) developed at the University of Nebraska – Lincoln under the sponsorship of the Federal Railroad Administration (FRA) has become more popular over the last decades [8,107,136]. The system computes relative vertical deflection (Y_{rel}) between the rail/wheel contact plane and rail surface at a distance of 1.22 m from the nearest wheel to the sensor system. The MRail system has been tested over different railway lines in the USA and Canada for evaluating track conditions [110,140-142]. Results from the MRail field tests show that the system not only has the potential to identify the local track problems, i.e. muddy ballast, degraded joints, crushed rail head, broken ties, but also provides an opportunity to map the subgrade condition and assess the track performance along the railway line [109,112,132,143].

In addition to the experimental studies, different numerical models have been used to investigate the relationship between track modulus and Y_{rel} data where numerical approaches have been proposed to estimate track modulus from Y_{rel} [25,110]. The current study aims to propose a new and advanced approach for estimating track modulus statistical properties from Y_{rel} data more accurately compared to previous studies. First, details of the MRail system are briefly presented and numerical models developed by others and their shortcomings are discussed. Then, artificial neural networks (ANNs) are explained as the main tool to investigate the relationship between track modulus and Y_{rel} data in this chapter. Different methods for training the ANNs are used and the effectiveness of the trained ANNs are investigated using error measurement parameters such as the coefficient of determination (R^2), the root mean square error (RMSE), and mean absolute percentage error (MAPE). Suitable signatures of Y_{rel} data are identified by conducting both statistical and frequency analysis. Feedforward neural networks are proposed as a function approximation technique to estimate the track modulus average (U_{Ave}) and standard deviation (U_{SD}) from Y_{rel} data. To further investigate the effectiveness of the ANNs for estimating the track modulus, noisy FEMs datasets are employed for training the ANNs. The accuracy of the track modulus estimations using these ANNs is also investigated using R^2, RMSE, and MAPE.

3.3. The stiffness measurement system and numerical simulations

3.3.1. MRail measurement system

The MRail system was originally developed at the University of Nebraska – Lincoln under the sponsorship of the Federal Railroad Administration (FRA) [8,107,136]. The system measures the relative vertical deflection (Y_{rel}) between the rail surface and the rail/wheel contact plane at a distance of 1.22 m from the nearest wheel to the acquisition system (Figure 3-1(a)). The sensors consist of two laser lines, a digital camera mounted on the side frame of the rail car (Figure 3-1(b)). The laser system projects two curves on the rail surface, whose minimum distance (d) is captured by the camera (Figure 3-1(c)). Subsequently, the distance between the camera and the rail surface (h) is computed by converting d. Finally, the relative deflection Y_{rel} is calculated by subtracting h from ($Y_{rel} + h$), the fixed distance between the rail/wheel contact plane and the camera.

(a)

(b)

(c)

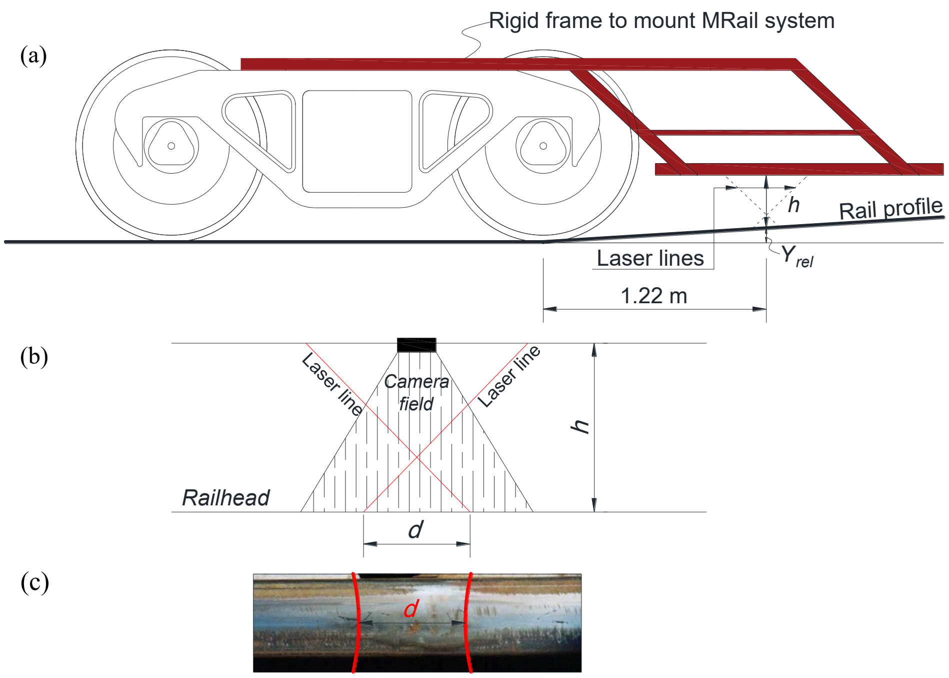

Figure 3-1. Demonstration of MRail system for Y_{rel} measurements: (a) the measurement system on rigid frame; (b) the sensor system; (c) projections of the laser lines on the railhead

The MRail system can measure the deflection at different sampling rates with the speed up to 96 km/h (60 mph). Winkler model and Finite element models have been used to estimate track modulus from Y_{rel} [143].

3.3.2. Winkler model

Rail deformation and bending stress under specific loads are typically estimated using Winkler model, which considers the track as an infinite beam on a continuous elastic foundation [14,144,145]. Using Winkler model (equation (3-1)), the vertical rail deflection (y) at a distance x from the applied load (P) is computed as follows:

$$y(x) = \frac{P\beta e^{-\beta x}(\cos\beta x + \sin\beta x)}{2U} \tag{3-1}$$

where β is the stiffness ratio, which is equal to $(U/(4EI))^{0.25}$, U is the track modulus, E is the modulus of elasticity of the rail, and I is the second moment of area of the rail.

From Winkler model, the vertical deflection profile of a rail is only dependent on track modulus value when rail size and vertical loads are known. Once a value is assumed for track modulus, the rail vertical deflection profile can be estimated using equation (3-1), and from the rail vertical deflection profile, Y_{rel} can be calculated as the relative vertical deflection between the rail surface and the rail/wheel contact plane at a distance of 1.22 m from the nearest wheel (Figure 3-1(a)) [107,111]. The main shortcoming in this method is that Winkler model assumes track modulus is constant along the track while field data shows track modulus stochastically varies along the track [7,146,147]. Therefore, the estimation of track modulus from Y_{rel} measurements needs more advanced numerical models.

3.3.3. Finite element model (FEMs)

FEMs allow the simulation of stochastically varying track modulus, and therefore, more accurate simulation of Y_{rel} measurements. Fallah Nafari *et al.* developed 90 FEMs with stochastically varying track modulus to facilitate a more detailed investigation of the relationship between Y_{rel} and track modulus [110]. Datasets from the 90 FEMs are used for the study in this chapter. Hence, details of the models are discussed briefly. The models are developed using CSiBridge software, where each model includes a 180.8-meter track structure with two rails, crossties, and spring supports [148]. To develop each model, a normal track modulus distribution is assumed and randomly selected numbers from this distribution are assigned to the spring supports along the track. Statistical properties of the assumed normal distributions are summarized in Table 3-1 and the applied loads are depicted in Figure 3-2. RE136 rail size and 0.508-meter tie spacings are used in the models.

Table 3-1. Statistical properties of the track modulus in the FEMs

Track modulus average (MPa)	**Coefficient of variation (COV)**	**No. of simulations**
41.4	0.25; 0.5; 0.75	30 (10 simulations for each COV)
27.6	0.25; 0.5; 0.75	30 (10 simulations for each COV)
12.8	0.25; 0.5; 0.75	30 (10 simulations for each COV)

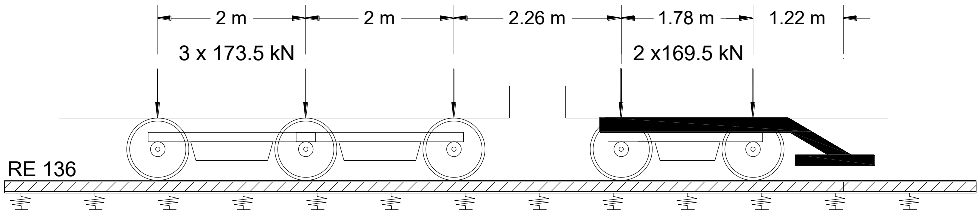

Figure 3-2. The loading condition in the FEMs

Individual Y_{rel} values are calculated from the vertical deflection profile at every 0.3048 m (≈ 1 ft) interval while the moving loads pass the track model. The dynamic effects of track-train interactions are not considered during the simulations due to the software's limitation. This is acceptable within the scope of this study which mostly focuses on the Canadian freight lines where speeds are most likely lower than 65 km/h.

Figure 3-3 shows an example of the inputted track modulus to the model and corresponding Y_{rel} output. Fallah Nafari *et al.* used basic statistical analysis and curve fitting approaches to study the relationship between statistical properties of track modulus (U) and Y_{rel} [110]. The results showed that the average and standard deviation of track modulus over a track section length can be estimated from the average and standard deviation of Y_{rel} over the same track section length. However, the estimation accuracy becomes lower by decreasing the track section length [110]. To overcome this shortcoming and increase the estimation accuracy of track modulus, ANNs are proposed for the track modulus estimations in this study.

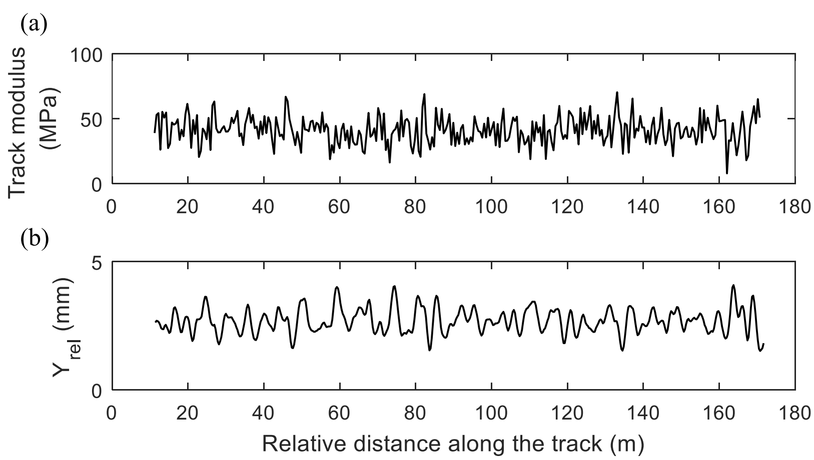

Figure 3-3. (a) Track modulus inputted to the FEM (Mean = 41.4 MPa, COV = 0.25); (b)The extracted Y_{rel}

3.4. Estimation of track modulus average

3.4.1. Multilayer perceptron artificial neural networks

Multilayer perceptron neural networks (MLPNN) are typically useful for classification and function approximation problems [149-153]. The implementation of MLPNN is operated with two stages of performance, i.e. training and testing procedures. Once the training process is successfully performed in a self-adaptive manner with all defined parameters (such as learning algorithm and network architecture including several layers and neurons in each layer), the network can effectively approximate the input-output mapping function.

MLPNN is a network containing two or more neurons distributed in different layers such as input layers, output layers, and hidden layers that connect input and output layers (Figure 3-4(a)). Each neuron has a nonlinear differentiable activation function that creates real values and is highly connected to other neurons based on synaptic weights $w_{ij}(n)$ (Figure 3-4(b)) as the level of connectivity.

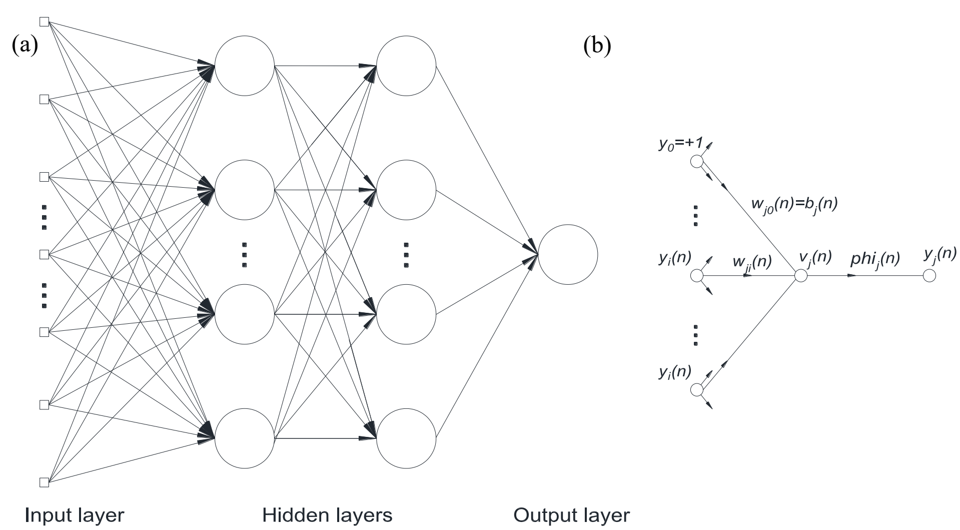

Figure 3-4. (a) Example of a two-hidden layer perceptron; (b) Typical operation at neuron *j*

One of the most complicated tasks before executing an MLPNN is that all required parameters should be well defined to approximate the input-output relationship, which is called the learning process that contains two phases. In the forward phase, the inputs are fed into the network from left to right and layer by layer with the fixed values of synaptic weights. In the backward phase, the error vector is first computed by subtracting the output of the network from the expected target. The error is then propagated backward from the output to the input layer. In this phase, the synaptic weights are adjusted to minimize the network error by solving the credit-assignment problems in the operation of each hidden unit. Each synaptic weight will be updated differently based upon the contribution of the corresponding hidden unit to the overall error. More information about training the network using backpropagation and gradient descent is given by Haykin [149].

3.4.2. Estimation procedure and results

The inputted track modulus and the corresponding Y_{rel} data from 180-m track models are divided into equivalent groups based on a track section length (e.g. 5 m, 10 m, etc.). Once the subgroups are defined, the average and standard deviation of Y_{rel} in each subgroup are used as the networks' inputs whereas the track modulus averages in the corresponding track segments are defined as the network's outputs.

Y_{rel} data extracted from eighty-one FEMs (out of ninety FEMs) are used to train the neural network. The accuracy of the trained network is then tested using the remaining nine (unseen) FEMs. These nine FEMs are called "unseen models" hereafter as they are not used in training the network. To test the trained network, track modulus average is estimated from Y_{rel} average and standard deviation for the nine unseen models. The estimated track modulus average is then compared with the track modulus inputted initially into the FEMs to generate Y_{rel} data. The effectiveness of the proposed network is measured based on three parameters: the coefficient of determination (R^2), the root mean square error (RMSE), and mean absolute percentage error (MAPE) [154]. These measures are described as follows:

$$R^2 = \left(\frac{\frac{1}{N}\sum_{i=1}^{N}[(o_i - \bar{o}_i) \cdot (y_i - \bar{y}_i)]}{\sigma_o \cdot \sigma_y} \right)^2 \tag{3-2}$$

$$\mathrm{RMSE} = \sqrt{\sum_{i=1}^{N} \frac{(y_i - o_i)^2}{N}} \tag{3-3}$$

$$\mathrm{MAPE} = \frac{1}{N}\sum_{i=1}^{N} 100\,\frac{|y_i - o_i|}{y_i} \tag{3-4}$$

where $\bar{o}_i$, $\bar{y}_i$, σ_o, and σ_y are the average and standard deviation of the estimated, and targeted values; N is the number of testing samples.

When a network is trained, 5-fold cross validation is employed to minimize any potential over-fitting problem and increase the network's generalization. Regarding the network architecture, a network with two hidden layers (each contains 15 hidden nodes) is used in this study. This network ensures an acceptable error range, avoids over-fitting, and optimizes the computational efficiency. From different tests, it is noted that increasing the number of hidden nodes and hidden layers does not necessarily mean the network's performance is improved. In fact, the input configuration is the most important factor that controls the network performance.

Five networks for five different track section lengths have been fully trained to perform this study. The track modulus average over five section lengths is then estimated for the nine new models using the trained networks. Table 3-2 presents the accuracy level of these estimations. From the table, the network performs better when the track section length increases although the error is numerically small even with the case of 10-meter section length. R^2 is 0.95 for the case of 10-meter section length, which means the estimated and inputted track modulus averages are well correlated. Moreover, the RMSE and MAPE are quite small, i.e. 2.81 MPa and 6.99% respectively, considering that range of inputted track modulus average is 12.8 to 41.4 MPa. In addition to confirming the applicability of Y_{rel} data in indicating track modulus information, the current methodology provides more accurate results than the other method in the literature [110]. As shown in Table 3-2, the R^2 value computed in the related study decrease as the length of the track segment reduces whereas the R^2 in the current study is almost constant for cases with 10 m track section and higher.

Table 3-2. Estimation accuracy of the track modulus average (no noise added)

Section length (m)	MAPE (%)	RMSE (MPa)	R^2	R^2 in [110]
5	12.42	4.58	0.86	0.79
10	6.99	2.81	0.95	0.93
15	5.90	2.56	0.95	N/A
20	4.32	1.60	0.98	0.96
25	3.87	1.63	0.98	N/A

The goodness of the estimation method for the case of 10 and 20 meter section lengths is demonstrated in Figure 3-5 for four models as an example. These four models had different track modulus average and variations. From the figure, the values estimated from networks are close to the actual track modulus average inputted to the FEMs. Most importantly, the local fluctuation of the track modulus is well captured.

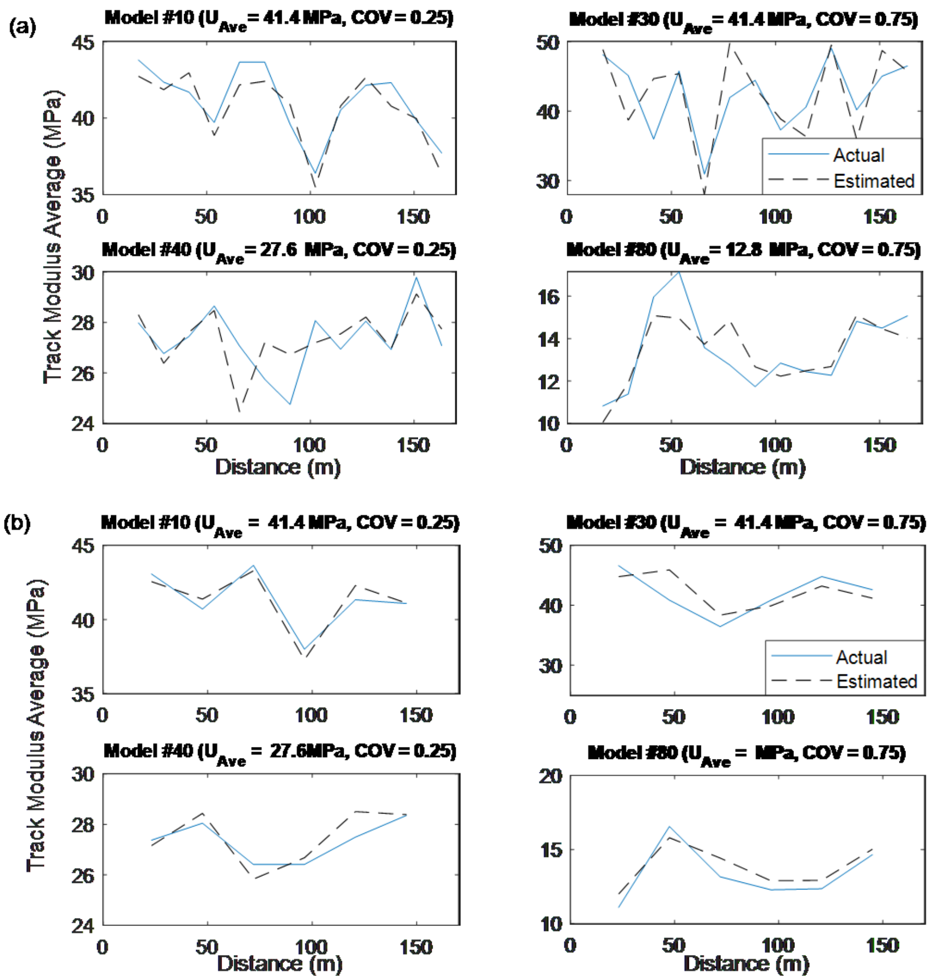

Figure 3-5. Moving average of the actual track modulus inputted to the FEMs vs. estimated values over: (a) 10-meter section length; (b) 20-meter section length

The effectiveness of the framework is investigated further by adding artificial noise to the Y_{rel} data extracted from the FEMs. This simulates the real-life condition in which the Y_{rel} measurements are affected by parameters such as the resolution of the MRail measurement system, track irregularities, etc. The artificial noise is added based on equation (3-5) [155]. An example of pure vs. noise-added Y_{rel} is shown in Figure 3-6.

$$Y_{rel-noisy} = Y_{rel} + \alpha \cdot 0.12 + \beta \cdot 0.1 \cdot Y_{rel} \tag{3-5}$$

where α and β are random number ranging from -1 to 1

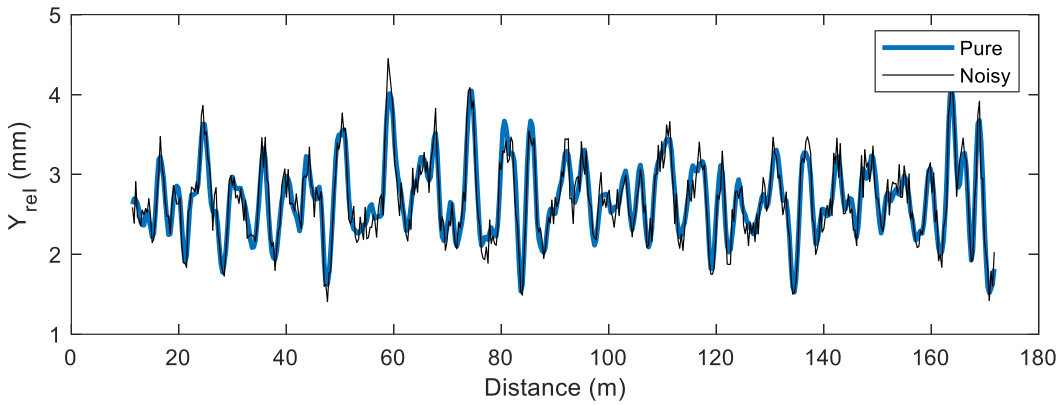

Figure 3-6. Demonstration of pure and *noisy* Y_{rel}

The noisy Y_{rel} is used to train new networks and then the trained networks are used to estimate track modulus average. The estimated track modulus is then compared with the inputted track modulus for each model and the error is reported in Table 3-3. From the table, the estimation of track modulus average (U_{ave}) from noisy Y_{rel} is still successful even for the short track section length of 10 m as R^2 is 0.95 and RMSE is 2.77 MPa. This demonstrates that the framework performs effectively even when the Y_{rel} data contains noise and thus expected to work with real-life data.

Table 3-3. Estimation accuracy of the track modulus average (with added noise)

Section length (m)	**MAPE (%)**	R^2	**RMSE (MPa)**	R^2 **in [110]**
5	14.09	0.83	5.07	0.79
10	7.01	0.95	2.77	0.93
15	5.93	0.96	2.36	-*
20	6.07	0.97	1.98	0.96
25	3.98	0.98	1.53	-*

*Not available for comparisons since those section lengths are not available in the previous study

3.5. Estimation of track modulus standard deviation (U_{SD})

The estimation of track modulus standard deviation from Y_{rel} data using statistical methods and curve fitting approaches has not been successful for track section lengths shorter than 80 m [110]. Therefore, frequency characteristics of the deflection data are investigated in this study to increase the estimation accuracy of track modulus standard deviation. The coefficients associated with the

Y_{rel} frequency components are employed as one of the inputs to the ANNs, whose outputs are the track modulus standard deviation over different track section lengths. As demonstrated in Figure 3-7, Y_{rel} and track modulus data are divided into different subgroups based on various track section lengths (similar to the procedure used for estimating the track modulus average). Then, statistical analysis, fast Fourier transform, and liftering technique are applied on Y_{rel} data in each subgroup to extract the average and standard deviation of the Y_{rel} and average and standard deviation of liftering FFT coefficients. These parameters are used as the inputs of ANNs.

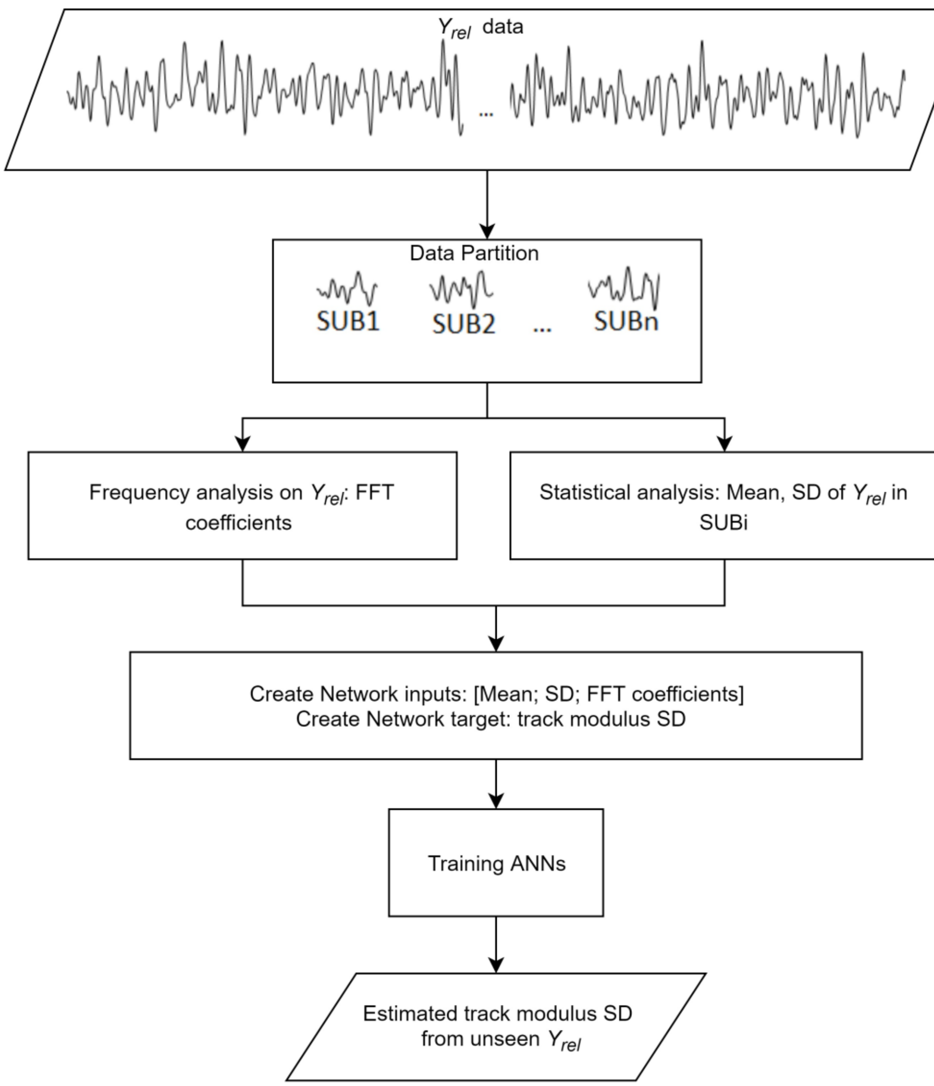

FFT: fast Fourier transform; SD: standard deviation; ANNs: artificial neural networks

Figure 3-7. Procedure for estimating track modulus standard deviation (U_{SD})

Figure 3-8(a) shows an example of the FFT coefficients of Y_{rel} data over a track section of 30 m for 81 models. As can be seen, the coefficients at higher orders are relatively small. This is undesirable for training the ANN due to possible bias. Therefore, the coefficients are processed using a liftering technique (equation (3-6)) to roughly normalize their variances [156].

$$X'(k) = \left(1 + \frac{L}{2}\sin\left(\frac{\pi(k+1)}{L}\right)\right) \cdot X(k), \qquad k = 0, \dots, N-1 \tag{3-6}$$

where L is the sin lifter parameter, which is 50 in the current study, $X(k)$ is the FFT coefficients.

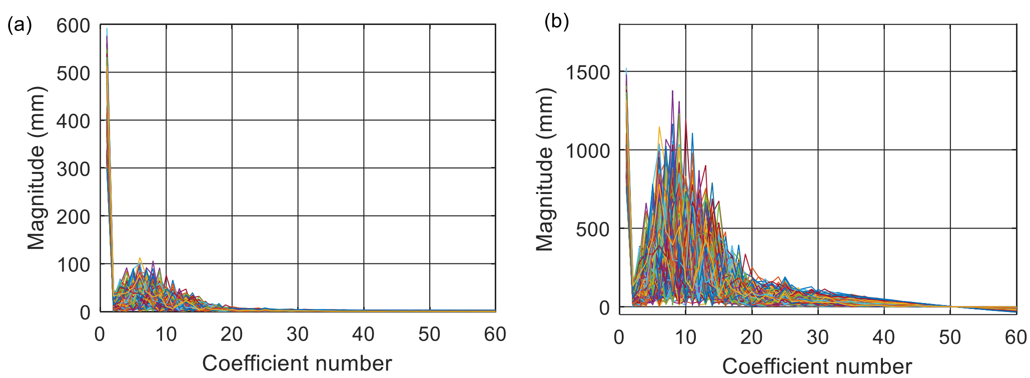

Figure 3-8. FFT of Y_{rel}: a) before liftering; b) after liftering

Once the liftering technique is applied (Figure 3-8(b)), average and standard deviations of the lifted FFT are calculated using equation (3-7) and (3-8) are used as two additional inputs for ANNs.

$$P_1 = \frac{2}{N-1} \sum_{k=0}^{(N-1)/2} |X'(k)| \tag{3-7}$$

$$P_2 = \sqrt{\frac{2}{N-1} \sum_{k=0}^{N/2} \left(|X'(k)| - P(1)\right)^2} \tag{3-8}$$

The architecture used for developing the network in this section has two hidden layers and 15 hidden nodes in each layer, similar to the network's architecture for estimating the track modulus average. The trained networks are used for estimating the track modulus standard deviation over different track section lengths and three accuracy measurements are reported in Table 3-4. In order to show the current input-output pair is optimized, two network architectures are trained (ANN-1 with 4 inputs, i.e. average and standard deviation of Y_{rel} and average and standard deviation of the lifted FFT; ANN-2 with 2 inputs, i.e. mean and standard deviation of Y_{rel}). In each case, the two networks are trained and tested multiple times and the mean and standard deviation of performance parameters are computed and reported in Table 3-4. For the case of 5 m section length, for instance, the networks' input and output are first extracted based on the chosen section (5 m), then ANN-1 and ANN-2 networks are trained using the training data and tested against the data extracted from 9 unseen FEMs.

From Table 3-4, the error values show that the standard deviation of track modulus (U_{SD}) can be estimated satisfactorily by both network configurations (ANN-1 and ANN-2). Even for the 10-m section length case, for instance, the coefficient of correlations between the actual U_{SD} and the one estimated by the two networks are high, e.g. 0.83 and 0.82, respectively. However, the networks with four inputs (ANN-1) slightly outperform the one with two inputs (ANN-2) regardless of the section lengths. Specifically, the RMSE and MAPE are always smaller than those arising from the trained networks whose inputs are the statistical properties of Y_{rel} only (ANN-2). Values estimated using the networks with four inputs have relatively high R^2 in all cases showing that the methodology is successful. In particular, the R^2 is as high as 0.94 for the case of 25-meter section length and the RMSE is 1.83 MPa, which is a relatively small error considering that the maximum standard deviation of the inputted track modulus in the FEMs is 31.05 MPa. Moreover, the first network (ANN-1) provides more reliable results as the standard deviation of RMSE remains stable (varying from 0.11 to 0.17 MPa) and lower than those of ANN-2. Therefore, combining FFT and statistical analysis to configure the input for the networks noticeably improve the estimation accuracy and increase the stability of the ANNs, the mapping function between the Y_{rel} characteristics and the track modulus standard deviation (U_{SD}). Most importantly, there is a big step forward in this study compared to the previous study, where the R^2 coefficient is 0.748 even though 40-meter section length is used [110]. The performance of this estimation can be considered ineffective as the R^2 coefficient reduced significantly in shorter track segment cases (Table 3-4). Hence, considering the current results, it can be claimed that neural networks are more powerful for mapping the relationship between Y_{rel} and track modulus, especially over the short track section lengths.

Table 3-4. Estimation accuracy of U_{SD} (no noise added, the standard deviation in the parenthesis)

Section length (m)	Network configuration	RMSE (MPa)	MAPE (%)	R^2	R^2 in [110]
10	ANN-1	3.00 (0.16*)	18.41	0.83	0.53
	ANN-2	3.05 (0.22)	19.12	0.82	-
15	ANN-1	2.36 (0.08)	15.01	0.89	-
	ANN-2	2.61 (0.39)	15.79	0.87	-
20	ANN-1	2.23 (0.11)	14.49	0.91	0.66
	ANN-2	2.59 (0.89)	14.47	0.88	-
25	ANN-1	1.83 (0.13)	11.96	0.94	-
	ANN-2	1.99 (0.30)	11.72	0.92	-
30	ANN-1	2.08 (0.17)	11.61	0.92	-
	ANN-2	2.14 (0.44)	11.79	0.91	-

*Standard deviation of the estimation error

For more descriptive results, the strong correlation between the actual and estimated track modulus's standard deviation for the 25-meter section length is demonstrated in Figure 3-9. As can be seen, the estimated standard deviations follow the same patterns as those of the actual values which greatly vary from 3.2 to 31.05 MPa.

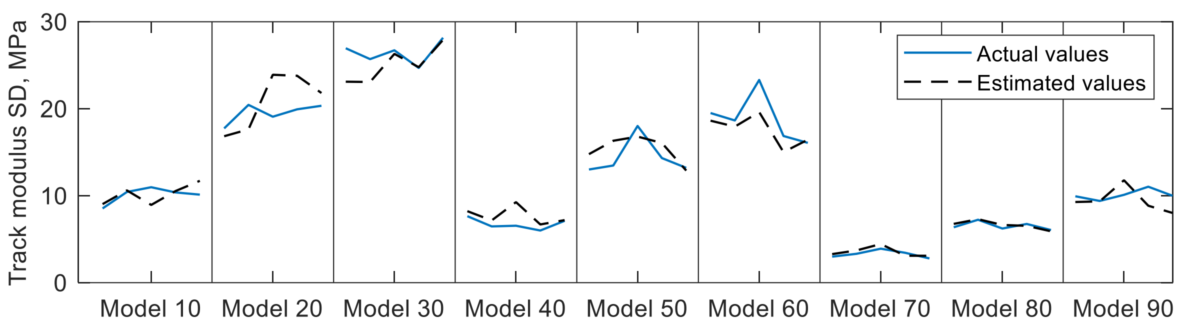

Figure 3-9. The actual track modulus standard deviation over 25-meter section length vs. estimated values

The effectiveness of the methodology is further validated by adding noise into the deflection data (Y_{rel}). Similar to the procedure mentioned in the previous section, noise is added to the Y_{rel} data from 90 models using Equation (3-5). The dataset from 81 models is then used to train the networks using two approaches: networks with two inputs (average and standard deviation of Y_{rel}) and networks with four inputs (average and standard deviation of Y_{rel} and average and standard deviation of lifted FFT). The developed networks are used to estimate track modulus standard deviations over different section lengths from unseen Y_{rel} data. The estimated values are compared with the standard deviation of track modulus inputted to FEMs and results are reported in Table 3-5. The results show the proposed approaches work well even when Y_{rel} datasets are affected by noises. The R^2 is again higher than 0.90 when the 25-meter or higher section lengths are utilized.

Table 3-5. Estimation accuracy of U_{SD} (with noise added)

Section length (m)	Network configuration	R^2	RMSE (MPa)	MAPE (%)
10	ANN-1	0.82	3.06	20.12
	ANN-2	0.81	3.14	19.64
15	ANN-1	0.87	2.59	16.30
	ANN-2	0.87	2.64	16.23
20	ANN-1	0.89	2.42	16.13
	ANN-2	0.89	2.45	14.71
25	ANN-1	0.94	1.86	11.96
	ANN-2	0.93	1.88	11.73
30	ANN-1	0.94	1.84	10.43
	ANN-2	0.93	1.89	10.95

3.6. Conclusions

In this chapter, two frameworks are proposed for estimating the track modulus average and standard deviation over different track section lengths. The frameworks employed Y_{rel} data (a relative rail vertical deflection measured using MRail system) for the track modulus estimations. The relationship between the statistical properties of track modulus and Y_{rel} data are investigated using artificial neural networks (ANNs). Datasets from FEMs are used to train the ANNs in which their outputs are either track modulus average or standard deviations. Both statistical and frequency analyses are conducted to identify the optimized inputs for the ANNs from the Y_{rel} data. From the results, the track modulus average over a track section length of 10 m or longer is accurately estimated from the average and standard deviation of the Y_{rel} data within the corresponding section length. Additionally, the standard deviation of track modulus over a section length of 25 m or longer is estimated with an acceptable level of accuracy. It is also shown that the trained ANNs work well for the track modulus estimations even when the Y_{rel} values as the ANNs inputs are affected by noise. The proposed ANNs are only applicable to a specific rail type and loading condition. Hence, a similar procedure should be followed to train ANNs for different ranges of rail sections and loading types.

Chapter 4: Estimations of Vertical Rail Bending Moments from Numerical Track Deflection Measurements Using Wavelet Analysis and Radial Basis Function Neural Networks[2]

4.1. Overview

A method for estimating rail bending moments from relative vertical track deflection data measured by a train-mounted measurement system is presented in this chapter. The novelty of the current study is that complete estimations of rail positive and negative bending moments from track deflection measurements are conducted by using Wavelet multiresolution analysis in conjunction with radial basis function neural network considering the effects of varying track modulus. The simulation results show that the proposed framework can effectively employ vertical track deflections to estimate both maximum positive and negative bending moments in rails with the average estimation error being 6.22% (i.e. 2.82 kNm). Moreover, the study confirms the capability of the train-mounted vertical track deflection measurement system (commercially known as MRail) in evaluating the rail bending moments over long distances.

4.2. Introduction

Rapid deterioration of civil infrastructures has been observed over the last few decades due to operational, environmental factors, and most importantly, aging of those structures. To maintain the reliability and safety aspects, implementing smart infrastructures appears as a possible solution due to their ability to provide self-diagnosis, self-prognosis, etc. In this context, structural health monitoring (SHM) plays an important role in smart systems. This study is devoted to the SHM of railway infrastructure since it is considered as one of the most important components of the civil infrastructure system in many countries, including Canada [1,157].

In railway engineering, several structural health monitoring systems have been developed for different types of evaluations. In general, those systems can be separated into two main categories, i.e. standstill and onboard systems. In standstill monitoring systems, measurement devices are installed at specific locations on the track primarily for condition monitoring of railway vehicles

---

[2] A version of this chapter is under review in the ASCE Journal of Transportation Engineering, Part A: Systems. Authors: N.T. Do, M. Gül (the outcome of the first review round was "minor revisions for review by editor only")

and track at the current location [77,88,92-95]. Onboard monitoring systems, on the other hand, have been in use for decades due to their ability in providing overall assessments of track conditions over long distances as well as the condition of the rail vehicle under monitoring. The typical applications of these systems include evaluations of vertical track stiffness, wagon and wheel defects [158,159]. Recently, rolling deflection measurement systems for track performance monitoring have gained attention due to their potential in assessing different aspects of track structures. There are two main approaches to system developments. One system provides the vertical track deflections using dynamic measurements on a single axle, whereas the other outputs relative vertical track defections. Among the systems developed in China, Europe, and North America [7,9,20,26,77,88,92-97], the current study is devoted to the use of MRail, a train-mounted vertical track deflection (VTD) measurement system, to investigate rail bending moments from the measured data [8,21,107].

Regarding the types of rail accidents in North America, derailments have been reported as one of the most common problems [2,160]. Relevant research studies have shown that the main cause is rail breaks (the leading cause of derailments) due to fatigue and excessive loads [2,10,161]. Rail sections are always subjected to either compression or tension due to the residual, thermal-induced stresses, and live bending stress from the applied moving loads. There are studies conducted to estimate different types of stresses in rails although the results are inconsistent due to their complex nature [33,162,163]. Specifically, live bending stresses, one of the main factors contributing to transverse fatigue defects that lead to rail breaks, are generally evaluated by using strain gauges installed at discrete locations to measure strains due to passing trains [18]. However, this method is not practically feasible for a whole railway network. Advances in fibre optic sensor technologies allow engineers to measure moving loads and the corresponding strains in the rails within a relatively long segment [18,164]. This has opened new opportunities in validating analytical methods for rail stress and bending moment estimations. However, implementing optical fibre is still limited at a specific segment of track.

Although the MRail system was developed primarily for track stiffness evaluations, it was also used for estimating rail bending moments [19]. However, there are concerns about the validity of the method. First, the mathematical relationship between the deflection data and bending stresses is oversimplified and heavily relies on Winkler model (an analytical model for vertical deflection and bending moments of track structure under specific loads and constant track modulus). Second, although the effect of track modulus variations was taken into account when examining the vertical rail deflection, direct estimations of bending moments were not yet determined [25].

In this study, the main objective is to develop a methodology to accurately estimate the positive and negative bending moments in rails using the data collected by MRail system. For this purpose, complete estimations of positive and negative bending moments from VTD under the effects of stochastic track modulus are proposed. The VTD data and bending moments are extracted from finite element models (FEMs) of track having specific rail profile, geometry, and various track modulus. Firstly, the extrema of Y_{rel} are extracted. Secondly, wavelet multiresolution analysis (WMRA) is conducted on positive and negative bending moments to extract their minima and maxima. Then, radial basis function neural networks (RBFN) are utilized to approximate the extrema of bending moments from VTD measurements. The results show that the methodology can effectively estimate the values of rail bending moments locally. Although it is infeasible to measure rail bending moments over long distances via strain gauges, efforts can be made to collect the rail bending moments at specific locations along the rail which is sufficient for the training stage of the estimation process. Therefore, the main contribution of the current study is that it is the first time positive and negative bending moments of rail over long distances are successfully estimated directly from the measured VTD data considering the effect of varying track modulus. The proposed framework can help to improve the rail reliability analysis by increasing the accuracy and productivity as well.

4.3. The measurement system

The current study focuses on one of the available train-mounted measurement systems whose main task is vertical track stiffness evaluations. In North America specifically, there are two different systems for this purpose: Track Loading Vehicle (TLV) [7] and the Real-time vertical track deflection measurement system (commercially called MRail), developed at the University of Nebraska-Lincoln under the sponsorship of the Federal Railroad Administration) [21]. These VTD systems have been proved to be a potential tool for assessment of track condition and rail bending stress based on analytical methods [22,133]. In this study, due to the ability in measuring vertical rail deflection at revenue speed with modest resources, measurement data from MRail are chosen as the preliminary inputs for rail bending moment estimations. Note that the same concept can still be applied for other track vertical stiffness measurement systems although minor modifications are required.

As shown in Figure 4-1, the sensor system consists of two laser lines and a digital camera, which is rigidly attached to a bracket mounted to the side frame of a railcar truck. By using image processing techniques, the relative deflection (Y_{rel}) between the rail-wheel contact line and the rail surface at 1.22 m from the nearest axle is measured [21]. In the next section, a theoretical background about the proposed methodology is given followed by detailed discussions about the two frameworks for maximum positive bending moments (M^+_{max}) and negative bending moments (M^-_{max}) estimations.

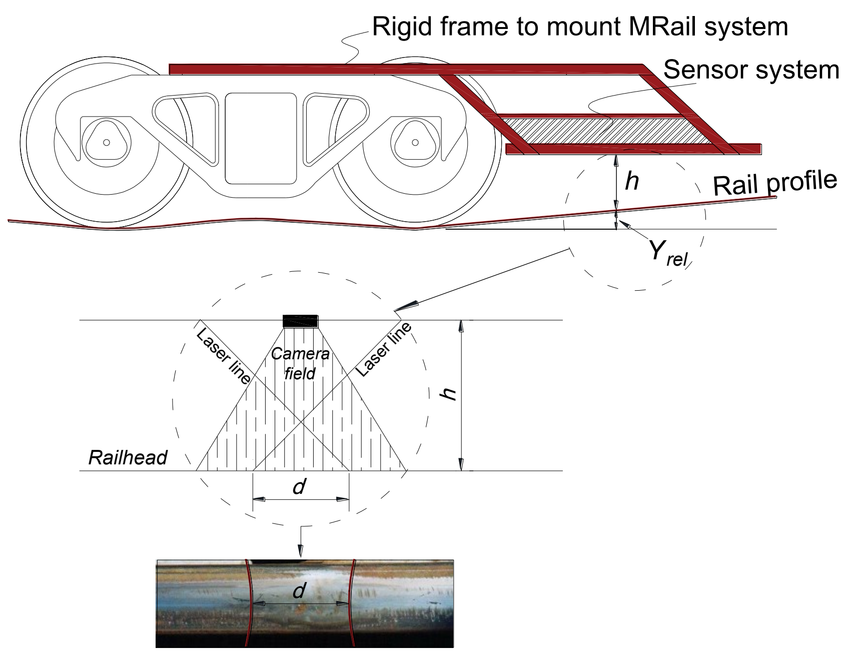

Figure 4-1. Illustration of MRail system

4.4. Methodology

Under the rail-wheel contact points, there is compressive stress at the railhead and tensile stress at the rail base, whereas a reversal of stress is observed on the sides of the wheel load locations. As the wheel passes over, the rail section is cyclically subject to positive moment and negative moment that are corresponding to the tensile and compressive stresses. The cycle of changing from tension and compression in railhead and base greatly contribute to transverse defects in rail materials [44].

The magnitude of bending stresses directly relates to the vertical rail displacements that are dependent on rail type, axle load, and track foundation stiffness (track modulus). Although the Winkler model is widely used as an analytical rail model, the assumption of constant track modulus is a considerable limitation. In this study, instead of relying on the Winkler model for computing the rail deflections and bending moments, FEMs of a track with a specific rail type, axle loads, and varying vertical spring supports (track modulus) are utilized to extract the vertical rail deflections (Y_{rel}) and the resulting bending moments. The FEMs are created in CSiBridge software and consist of two rails (size RE136), crossties, spring supports connected to the base of the crossties [148]. The model length is 180.8 m with 0.508 m tie spacing resulting in a total of 357 crossties. The effects of boundary conditions are minimized by assigning constant stiffness within 10 m at both ends of the models and only the middle part with various stiffness is used for the analysis. Y_{rel} at 0.3 m (1 ft) interval is computed from the deflected rail profile. A demonstration of the applied loads is shown in Figure 4-2.

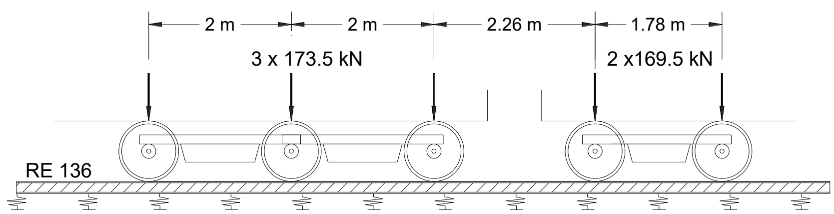

Figure 4-2. Demonstration of the applied loads

In order to study the variations of rail vertical deflections and bending stresses due to the variations of track modulus, 90 models with random normal distribution track modulus are considered (Table 4-1). The generated track modulus values are converted to the stiffness coefficients assigned to the spring supports. Further validations of the FEM model can be found in [110].

Table 4-1. Statistical properties of the track modulus in the FEMs

Track modulus average (MPa)	**COV**	**No. of simulations**
41.4	0.25; 0.5; 0.75	30 (10 simulations for each COV)
27.6	0.25; 0.5; 0.75	30 (10 simulations for each COV)
12.8	0.25; 0.5; 0.75	30 (10 simulations for each COV)

Figure 4-3 shows an example of the track modulus assigned to a model, the extracted Y_{rel}, and maximum bending moments (M^{+}_{max} and M^{-}_{max}). As can be seen, there are some degrees of correlations between Y_{rel} and the corresponding positive and negative moments. However, direct relationships between Y_{rel} and bending moments have not been configured successfully although different studies have been conducted [19,25].

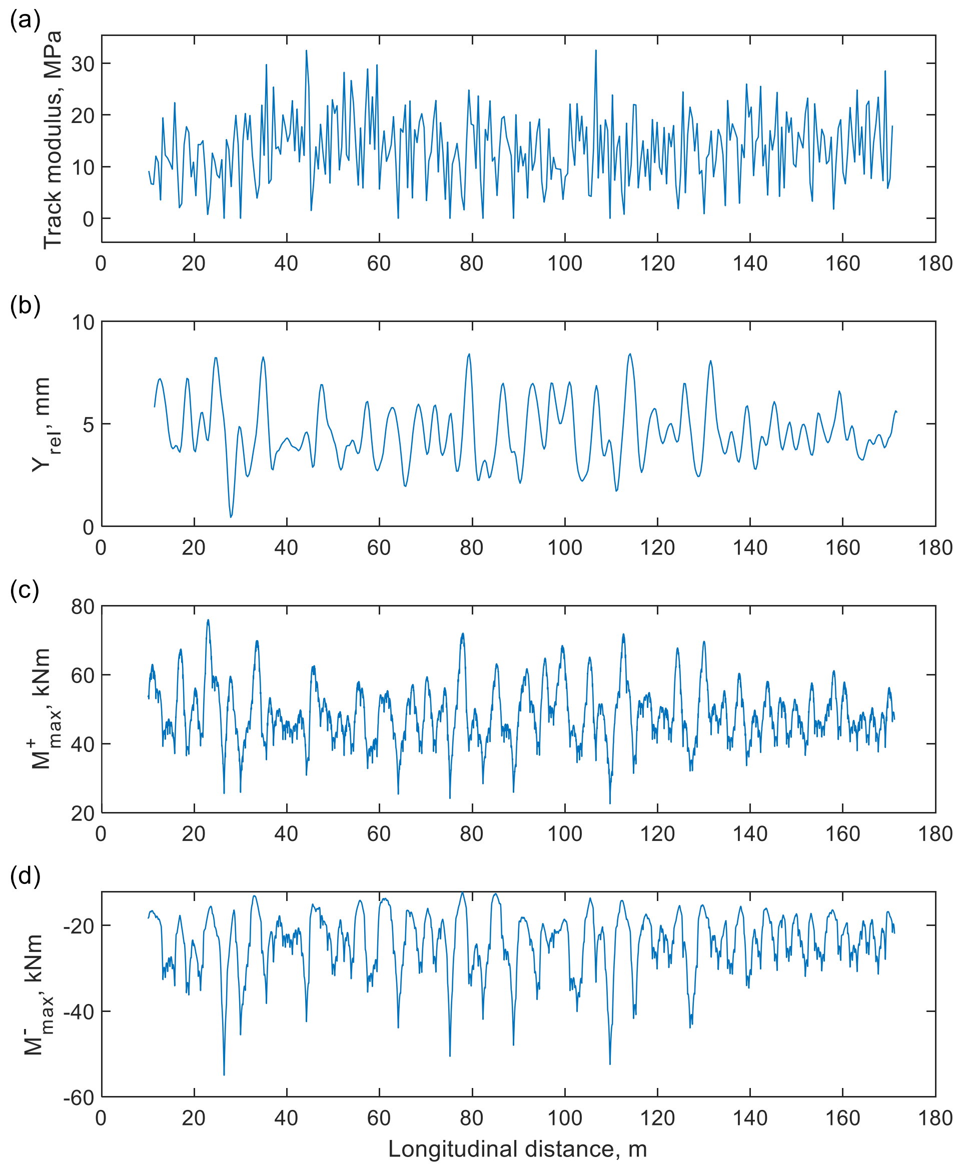

Figure 4-3. Demonstration of a numerical model: (a) the inputted track modulus; (b) the extracted Y_{rel}; (c) the envelope M^+_{max} profile; (d) the envelope M^-_{max} profile

In the current work, a technique is proposed by using wavelet analysis and radial basis function neural networks for the estimations of minima and maxima of positive and negative bending moments via Y_{rel} . First, the minima and maxima of Y_{rel} are extracted. Second, wavelet multiresolution analysis is utilized to decompose the bending moments (M^{+}_{max} and M^{-}_{max}) into different levels so that the true maxima and minima of bending moments can be defined. Third, RBFN is employed as a function approximation tool to map the Y_{rel} (local minima and maxima) into positive and negative bending moments. Finally, the proposed methodology is validated by examining the estimated bending moment from unseen Y_{rel} data. In the following sections, an overview of wavelet analysis and RBFN are given followed by the details about the procedures for positive and negative bending moment estimations.

4.4.1. Wavelets and multi-resolution analysis

An overview of wavelet analysis is given herein. More details about wavelet analysis can be found in the literature [165-169]. Continuous wavelet transform (CWT) of a signal *x(t)* is determined as:

$$\mathrm{CWT}(\alpha,\tau) = \frac{1}{\sqrt{|a|}}\int_{-\infty}^{+\infty} x(t)\psi\left(\frac{t-\tau}{a}\right)dt \tag{4-1}$$

where a and τ are the scaling and translation parameters of the wavelet function $\psi(t)$. The signal is continuously multiplied by each scaled and shifted version of the mother wavelet.

The discrete wavelet transform (DWT) of a digitized signal $x(n)$ is computed as:

$$DWT(j,k) = 2^{-j/2}\sum_{n=0}^{N-1} x(n)\psi\left(2^{-j}n-k\right) \tag{4-2}$$

where $\psi(n)$ is the discrete wavelet function, $2^{-j/2}$ and $\psi(2^{-j}n - k)$ are the parameters for the scaled and shifted version of the $\psi(n)$.

The scale parameter (j) and the translation parameter (k) are the discrete versions of a and b. The scale parameter controls the stretching and shrinking of the mother wavelet whereas the shift parameter refers to the movement of the mother wavelet along the entire signal.

Practically, DWT is performed by an efficient process called Wavelet multi-resolution analysis (WMRA), which was proposed by Mallat [170]. WMRA is a process of filtering a signal through low-pass and high pass filters whose parameters are related to the scaled and shifted versions of the mother wavelet. A signal $x(n)$ can be expanded as:

$$x(n) = \sum_{k=-\infty}^{+\infty} a_{J,k}\phi_{J,k}(n) + \sum\nolimits_{j=1}^{J} \sum\nolimits_{k=-\infty}^{+\infty} d_{j,k}\psi_{j,k}(n) \tag{4-3}$$

where $\phi_{j,k}(n) = 2^{j/2}\,\phi(2^j n - k)$ is the scaled and shifted version of the scaling function $\phi(n)$; $a_{J,k}$ and $d_{j,k}$ are the expansion coefficients at the scale level *J* and *j*.

In equation (4-3), the first summation is referred to as the approximation *A* (the high-scale, low-frequency component of $x(n)$); the second summation is referred the detail *D* (the low-scale, high-frequency component of $x(n)$); In practice, the level of decomposition can go up to a finite number *J*, therefore, equation (4-3) can be simplified as

$$x(n) = A_J + \sum\nolimits_{j=j_0}^{J} D_j \approx A_J + \sum\nolimits_{j=1}^{J} D_j \tag{4-4}$$

where $A_J = \sum_{k=-\infty}^{+\infty} a_{J,k}\phi_{J,k}(n)$ is the approximation at level J and $D_j = \sum_{k=-\infty}^{+\infty} d_{j,k}\psi_{j,k}(n)$ is the detail at level *j*.

4.4.2. Radial basis function neural networks (RBFN)

Similar to the Multilayer perceptron, RBFN is a layer-type structure (Figure 4-4). Typically, the network contains three layers, i.e. the input layer, hidden layer, and output layer. Input vector *x* with *S* dimensions is presented into *S* nodes of the first layer, whereas the hidden layer contains *K* nodes. Depending on the chosen algorithms the number of hidden nodes may vary from 1 to *N*, the size of the training sample. The output at each hidden node is calculated by a radial basis function (i.e. Gaussian function). The network outputs are computed as the weighted sum of hidden layer outputs.

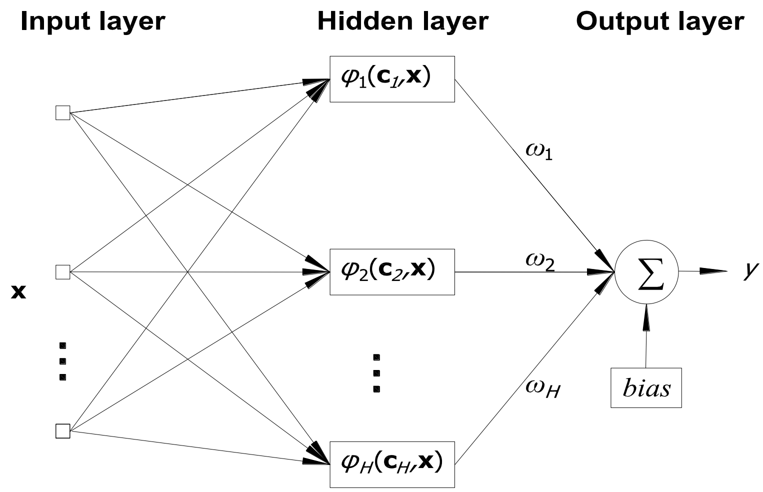

Figure 4-4. Radial basis function neural network

Since the RBFN is a distance-weighted regression technique, it suitably fits the applications for function approximations and pattern classifications. The universal approximation function using RBFN can be realized as:

$$\begin{aligned} y_k = F(\mathbf{x}) &= \sum_{j=1}^{H} w_{kj}\varphi_j(\mathbf{c}_j,\mathbf{x}) + b_k \\ &= \sum_{j=1}^{H} w_{kj} \exp\left(-\frac{1}{2\sigma_j^2}\left\|\mathbf{c}_j - \mathbf{x}\right\|^2\right) + b_k \end{aligned} \tag{4-5}$$

where y_k is the kth element of the output, w_{kj} is the element of the weight matrix $\mathbf{W}$, $\mathbf{c}_j$ and σ_j are the centroid (or kernel) and the width of the Gaussian function at the jth hidden node; b_k is the kth element of the bias vector at the output layer.

Training RBFNs involves selecting an optimized weight matrix $\mathbf{W}$, the centers and widths of the RBFs. The process consists of three main steps:

- Determine the center unit in each hidden node by k -means clustering algorithm.
- Initialize the width of the Gaussian functions.
- Compute the weight matrix by recursive least-square estimation [149].

k-means clustering algorithm is commonly used to group training data and determine the clusters' means which are corresponding to the kernels or centers of the Gaussian functions in the hidden layer. The establishments of the centers are followed by the selection of the RBF widths. The heuristic for choosing the function width (also known as the spread) is that it should be large enough so that there will be sufficient overlaps among the Gaussian functions for a smooth approximation. Too large widths can lead to overgeneralizations since there no distinct peaks in the decision region formed by the RBFs. In contrast, RBFs with too small widths are not desirable since more RBFs in the network are requires, which potentially results in a lack of generalizations and overfitting. In this study specifically, the optimized width is chosen within the range from 0.05 to 10. Overall, the training procedure of an RBFN is demonstrated in Figure 4-5. It is worth noting that careful attention should be given in training RBFN since it is susceptible to overfitting compared to other network types.

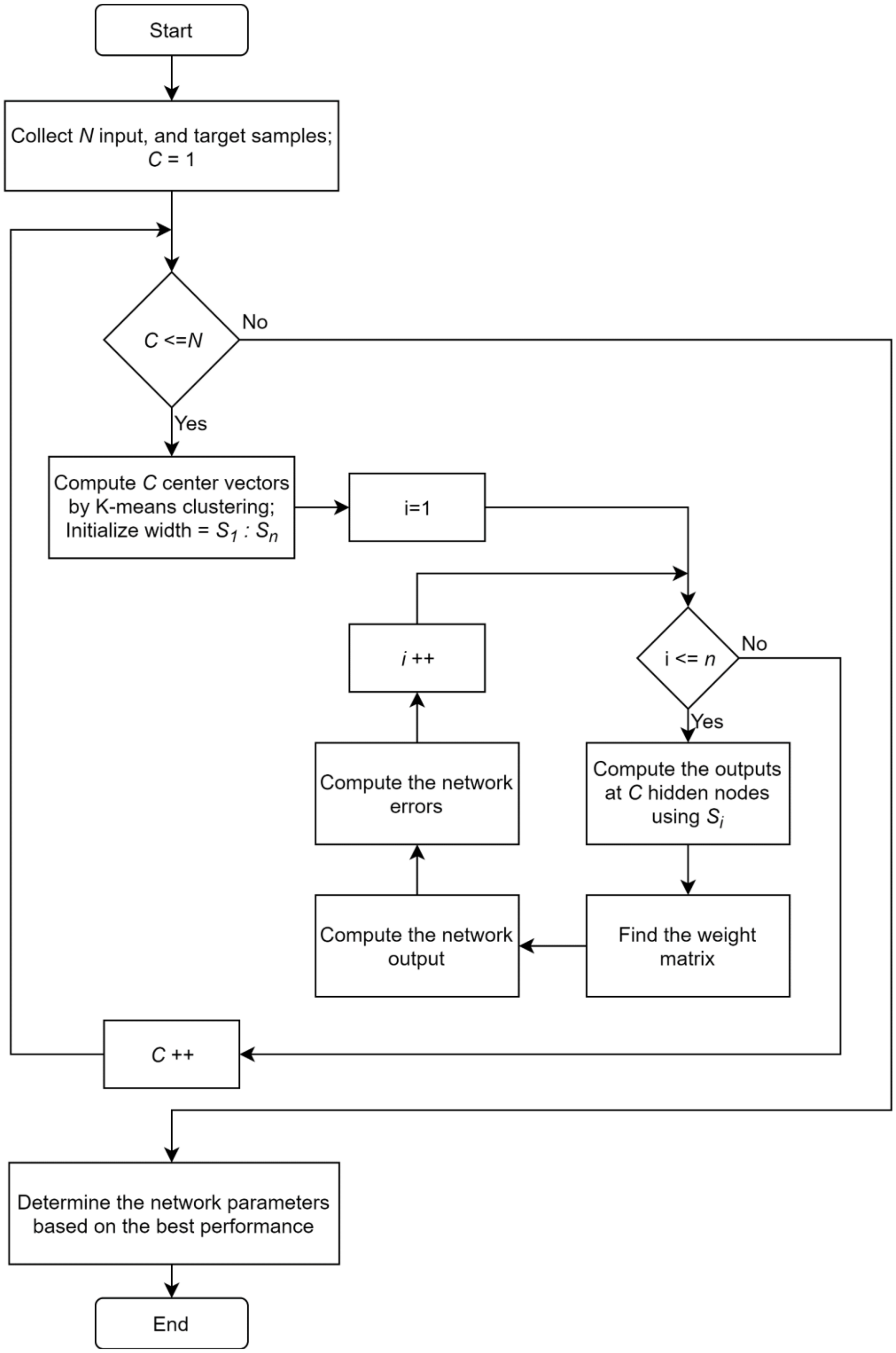

Figure 4-5. Flowchart of defining RBFN parameters

4.5. Estimation of positive bending moment (M^+_{max})

Y_{rel} data extracted from a FEM model and the corresponding maximum positive moment are shown in Figure 4-6.

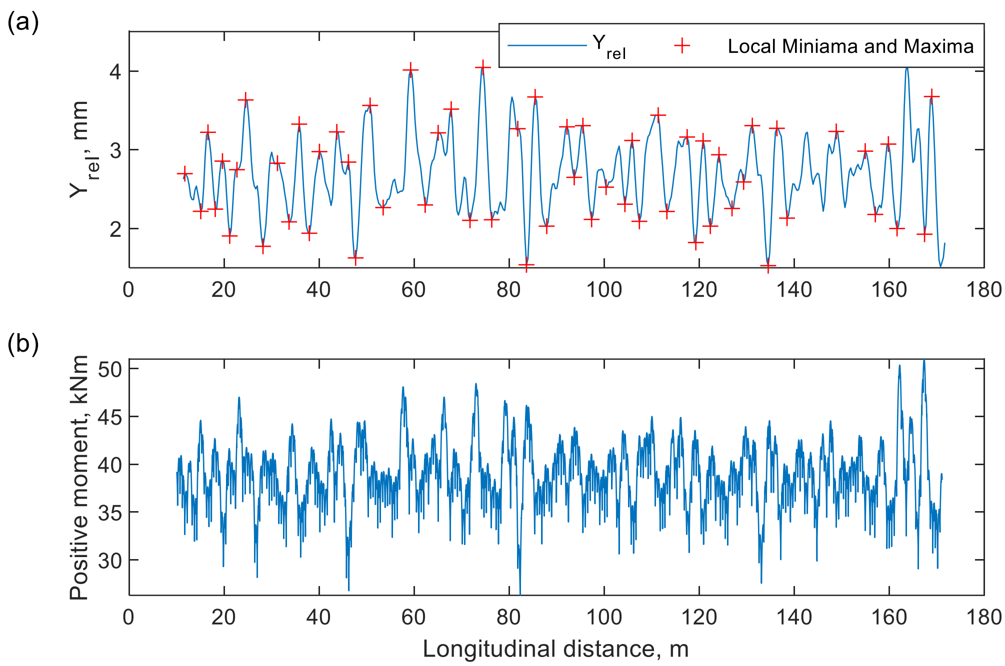

Figure 4-6. (a) Y_{rel} data along the rail location; (b) The corresponding positive moment

It can be noticed that there are some correlations between the fluctuations of Y_{rel} and those of maximum positive bending moment. The data shows the highest correlation occurs at approximately 1.22 m lag, which is due to the configuration of MRail system whose measured point is 1.22m away from the nearest wheel. Moreover, the strongest similarity is found at the extreme points between Y_{rel} and positive bending moments. Considering that critical locations along a track are more likely to suffer from excessive deflections and high bending moments, the current study is conducted to estimate the local extrema of positive bending moments from relative deflection data (Y_{rel}).

The minima and maxima of Y_{rel} can be easily extracted (Figure 4-6) by applying a simple forward difference technique. However, it is not the case for bending moment data as there are local peaks in the signal because of multiple load case combinations. Therefore, wavelet multiresolution analysis (WMRA) is utilized to decompose the positive moment into different components containing different frequency contents. A four-level decomposition of the moment in Figure 4-6.b is shown in Figure 4-7.

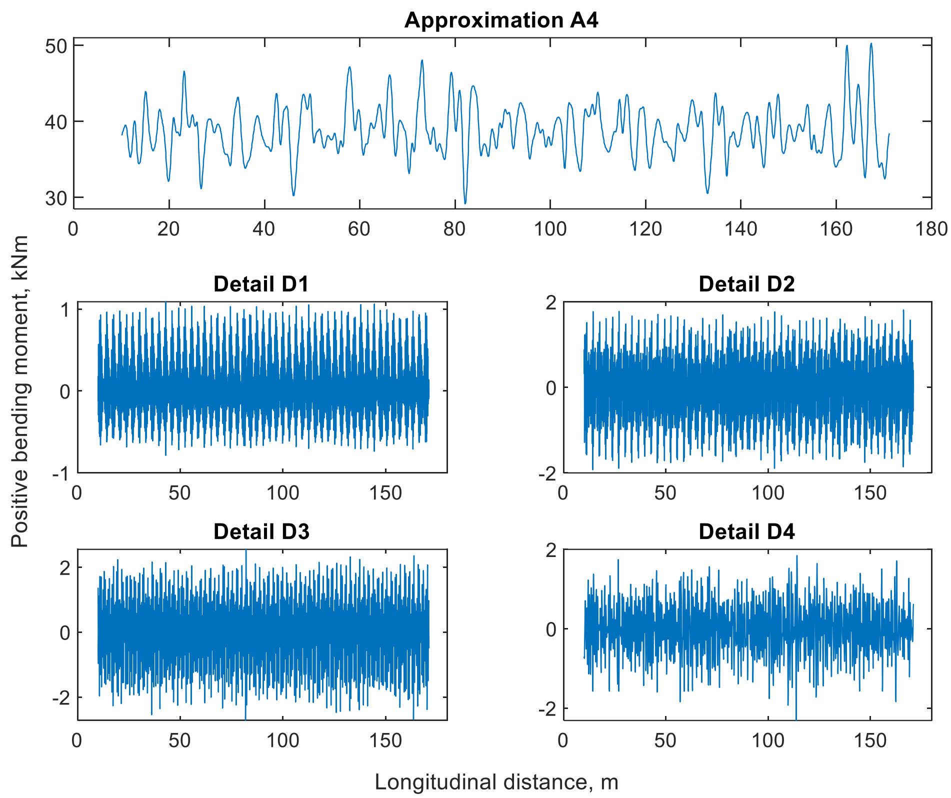

Figure 4-7. The decomposed approximation and details of the maximum bending moment using Daubechies wavelet at four-level decomposition.

As can be seen, the approximation A_4 can be considered the main component of the positive bending moment since its magnitude occupies more than 90% the original moment, whereas the remaining decomposed components, i.e. D1 to D4, are numerically insignificant. Therefore, the positive bending moment data from 90 models are analysed by WMRA to compute the approximation A4 (Figure 4-7), which are subsequently used to extract the bending moment's local minima and maxima.

Having the local extremum of Y_{rel} and positive bending moments allows the construction input-output pairs for training RBFNs. As it was mentioned in the above section, one of the most important parameters of RBFNs is the number of the radial basis function's width that strongly varies depending on input data, number of hidden neurons and error threshold during training. Therefore, for the purpose of finding the optimized parameters (Figure 4-5), different networks are trained with varying hidden neurons and the width values ranging from 0.05 to 10. The final network will be the one that produces the minimum error. Note that data from 81 out of 90 models are used during training, whereas the remaining 9 models are separated and reserved for testing the proposed framework. Five-fold cross-validation is also employed to minimize the overfitting problem.

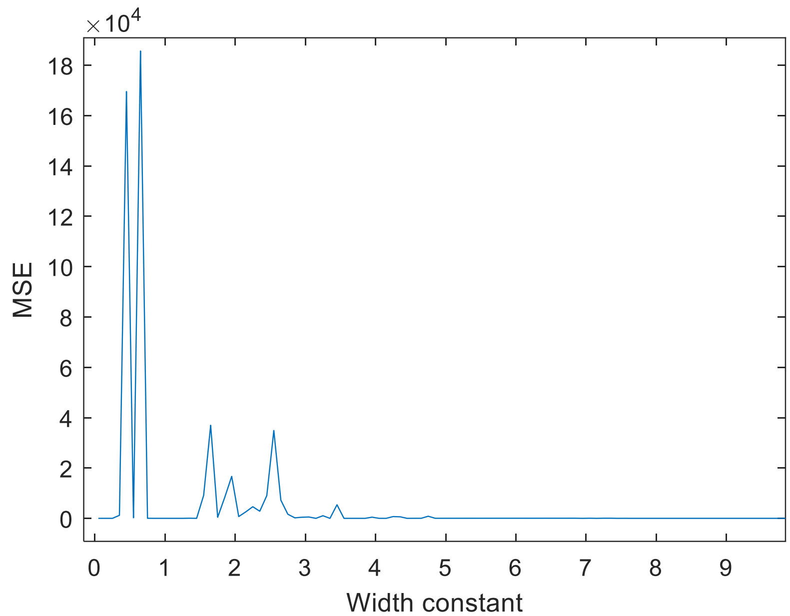

Figure 4-8. the performance of RBFNs with different widths

Figure 4-8 shows the performance of RBFNs in terms of mean square errors (MSE) with different width values and 100 hidden neurons. It can be seen that increasing the width value can reduce the MSE whose value converges at a width of 3.9. Considering that larger widths does not necessarily result in better performance, it is decided that the final width value is 3.9.

After successfully establishing the RBFN, testing with unseen data is conducted. Figure 4-9 shows the bending moments of six models that were not used during training the networks, the estimated minima and maxima values. As can be seen, all critical points including the lower and upper bounds in the bending moments are effectively captured.

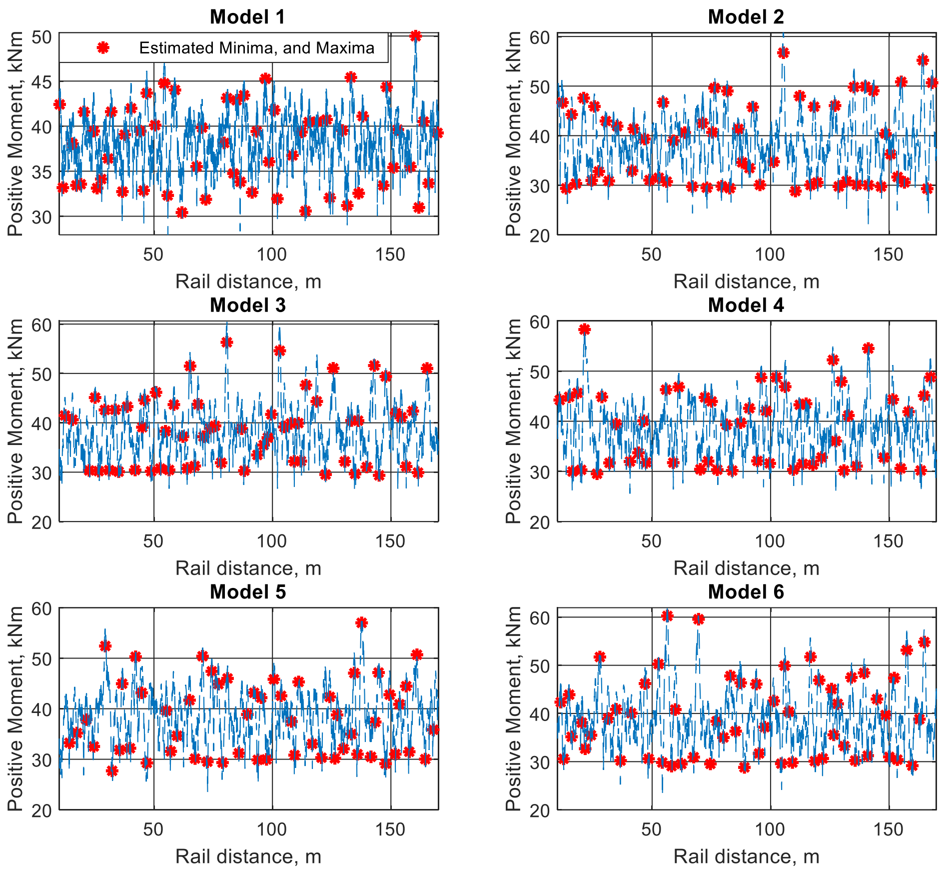

Figure 4-9. the variations of positive bending moment and its estimated extremum

Considering the performance measures of the RBFN, RMSE (root mean square error) and MAPE (mean absolute percentage error) are considered in this chapter. They are defined as below:

$$\mathrm{RMSE} = \sqrt{\sum_{i=1}^{n} \frac{(y_i - \hat{y}_i)^2}{n}} \tag{4-6}$$

$$\mathrm{MAPE} = \frac{1}{n} \sum_{i=1}^{n} \frac{y_i - \hat{y}_i}{y_i} \times 100 \tag{4-7}$$

where y_i and $\hat{y}_i$ are the actual and estimated values, n is the forecast horizon

Estimation errors of all nine unseen models are shown in Table 4-2. As can be seen, the estimation of positive bending moments is successful as the RMSE and MAPE are numerically small. Specifically, the highest error is found in model 8, where the RMSE is 3.65 kNm. The error is deemed acceptable since it is 7.3% of the actual bending moment. In the next section, the procedure for estimating negative bending moments is introduced. The reason is that the estimation requires different input-output pairs and further modifications are conducted to train the RBFN.

Table 4-2. Estimation errors (Maximum positive bending moment)

Model	1	2	3	4	5	6	7	8	9
RMSE (kNm)	1.81	2.56	3.01	1.50	2.41	3.40	3.32	3.65	3.32
MAPE (%)	3.80	4.84	5.81	3.02	4.85	7.25	6.39	7.30	6.26

4.6. Estimation of negative bending moment (M^{-}_{max})

In this case, the same procedure is applied to extract the local minima and maxima of Y_{rel} and the negative bending moments. However, 5-level WMRA is applied to compute the approximation A5 of the negative bending moment. Subsequently, the local minima of the negative bending moment are extracted from the approximation A5. An example of Y_{rel} and the corresponding negative bending moment is shown in Figure 4-10. In this case, specifically, the local minimum values of the negative bending moment are more important since they are predominantly high in magnitude. Therefore, the purpose of the current section is to estimate the local minima (those with high magnitudes) of the negative bending moment.

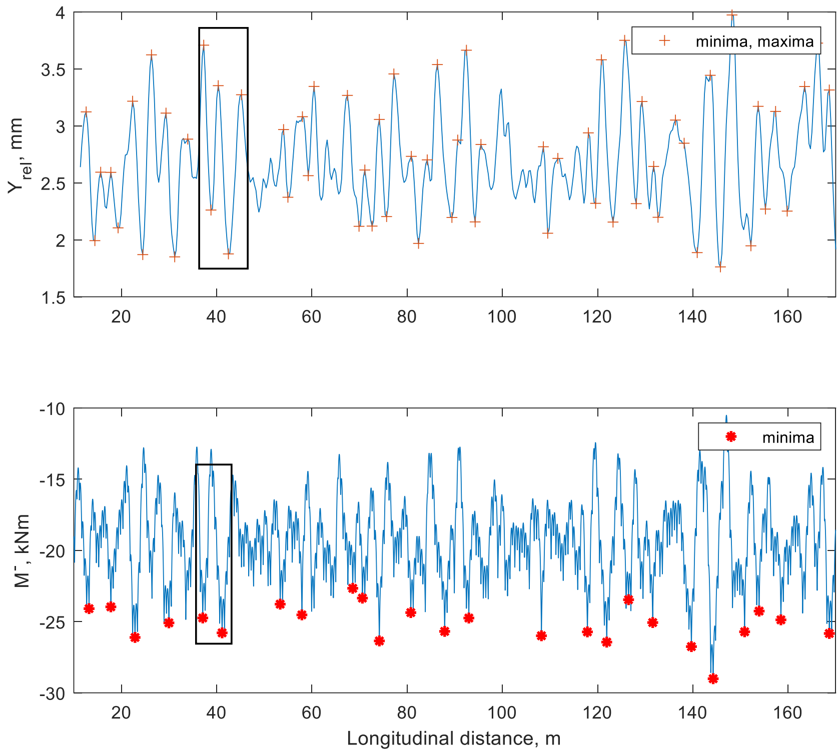

Figure 4-10. Relative deflection and the corresponding negative bending moment

In contrast to the process of positive bending moment estimations, where the output is computed via a one-to-one mapping function, the estimation of negative bending moment requires more inputs for better estimations. Specifically, it is observed that a local minimum value of negative bending moments strongly correlates to three consecutive max-min-max Y_{rel} points (demonstrations are shown in the rectangular boxes in Figure 4-10). This observation can be further confirmed by the Euler-Bernoulli beam theory, where the bending moment is proportional to the second derivative of the deflection. As shown in equation (4-8), the bending moment results from the double integration of the vertical deflection which can be approximated by three deflection points in the discrete form.

$$M = -\frac{EId^2\omega}{dx^2} \cong -EI \times \frac{\omega_{x+1} - 2\omega_x + w_{x-1}}{\Delta x^2} \qquad (4\text{-}8)$$

where M is the bending moment, EI is the bending stiffness, E is the modulus of the elasticity of the rail, and I is the second moment of area of the rail, ω_x is the vertical deflection at position x.

After the input-output datasets are collected, training a RBFN is conducted by selecting the appropriate parameters. In this specific case, solely using mean square error (MSE) as the cost function during training is not effective, since it will result in an extremely large number of hidden neurons and consequently overfitting. Therefore, in addition to mean square error, the coefficient of correlation is used as the main objective to obtain the optimized number of hidden neurons and the Gaussian function's spread. Figure 4-11 shows the network performance under different values of widths and hidden nodes. The figure clearly shows that increasing the number of hidden nodes and spread constant does not always help to improve network performance. In fact, the network performance is significantly reduced as the width and the number of hidden nodes is larger than 5 and 50 respectively. From Figure 4-11.b, it is concluded that 2.85 is the optimized value of the width and 28 hidden neurons are chosen for the current network. It is worth mentioning again that overfitting is one of the biggest concerns in designing RBFN, which prevents it from being deployed in real-life applications. Using multiple types of measures for network performance would be a solution.

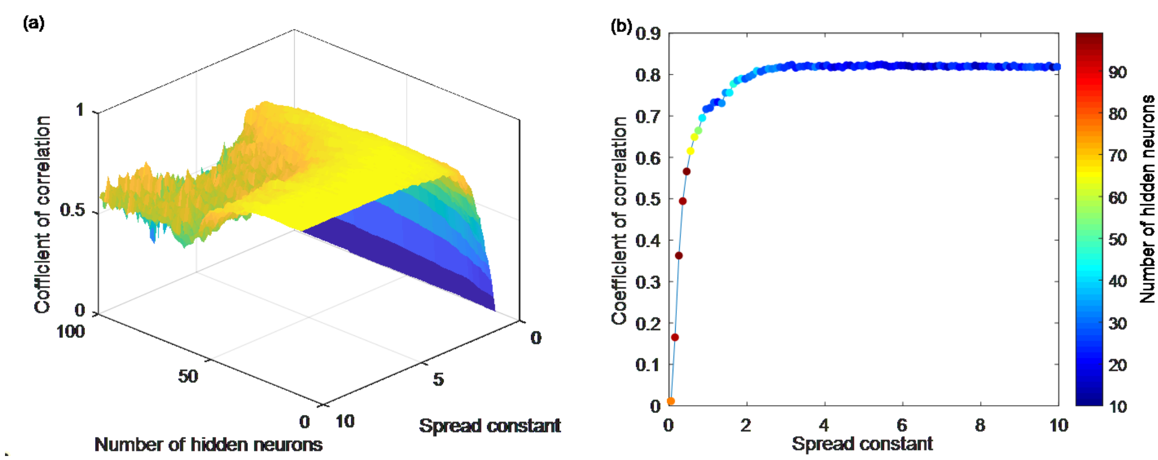

Figure 4-11. Network performance: (a) 3D plot; (b) 2D plot

Having the network fully trained, the new data are utilized to evaluate the effectiveness of the proposed estimation method. The negative bending moments of the six models that were not used during training are shown in Figure 4-12. It is clear from the figure that almost all local minima values are captured. The results continue to confirm that the negative bending moment is strongly related to the statistical properties of Y_{rel}, the relative vertical deflection.

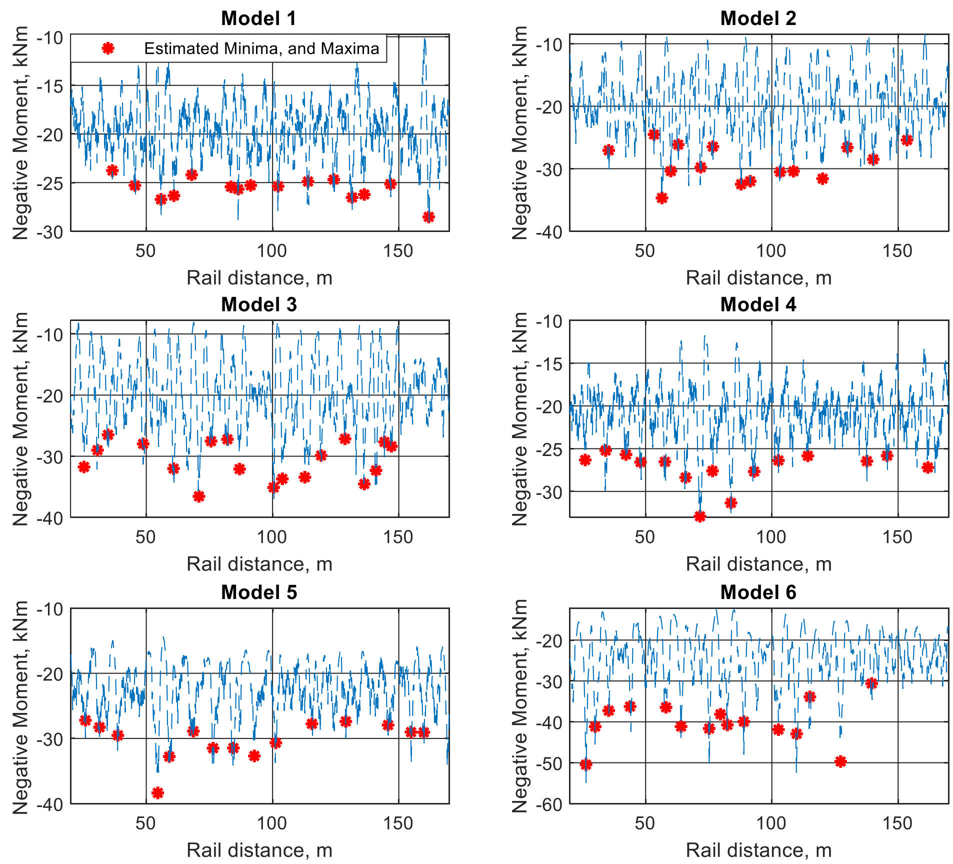

Figure 4-12. the variations of positive bending moment and its estimated minimum

Regarding the estimation errors shown in Table 4-3, the small errors reveal that the maximum negative bending moment can be successfully estimated from Y_{rel}. Specifically, the highest error is found in model 9, where the *RMSE* is 5.01 kNm (equivalent to 10.53 % of $M_{\max}^{-}$). In this context, the estimation error is deemed appropriate considering that the maximum negative moment is as high as 55 kNm.

Table 4-3. Estimation errors (Maximum negative bending moment)

Model	1	2	3	4	5	6	7	8	9
RMSE (kNm)	1.69	1.51	2.53	2.03	3.61	2.83	1.82	4.68	5.01
MAPE (%)	5.59	3.95	7.09	5.94	8.63	6.56	5.26	8.89	10.53

4.7. Conclusions

A new methodology is presented in this chapter to evaluate rail vertical bending moments using train mounted VTD records. First, VTD measurements, maximum positive and negative bending moments are extracted from finite element track models having varying track modulus. Second, Wavelet multiresolution analysis is applied to extract the extremum values of the bending moments in the rail section. Subsequently, a Radial basis function neural network (RBFN) is utilized as a universal function approximation to quantify the correlation between the extreme values of Y_{rel} the corresponding bending moments. The proposed method successfully estimates the rail bending moments (M^{+}_{max}, M^{-}_{max}) from VTD measurements considering the effects of varying track modulus. The results also confirm the ability of using MRail measurement system for rail bending moment estimations which is useful for rail reliability analysis.

Chapter 5: A Recursive SSA-AMUSE Based Technique for Single Channel Blind Source Separation with an Application on Vertical Track Deflection Measurements[3]

5.1. Overview

Vertical track deflection measurements have been widely used to evaluate track stiffness. However, interpreting these measurements remain a challenge due to multiple sources that contribute to the total deflections. This chapter presents a recursive SSA-AMUSE (SSA: singular spectrum analysis, AMUSE: algorithm for multiple unknown signals extraction) technique to solve single channel blind source separation (SCBSS) problem, aiming to evaluate track stiffness from a single observation of vertical track deflections. As the first step, the inputted signal is decomposed into finite sequences using SSA. Then, AMUSE is employed to recover the source signals from the SSA components. The proposed SSA-AMUSE method is implemented iteratively to extract the original signals sequentially. The first application of the proposed method on the synthetic signals provides more accurate results than the other available methods. Moreover, the successful application of the current method on vertical track deflection measurements due to the simultaneous impact of varying track modulus and track geometry greatly promotes the application of a continuous track stiffness measurement system on rail-track structure health monitoring.

5.2. Introduction

Measured signals of dynamic mechanical systems contain various information and features for condition diagnosis. However, the sampled signal is simply the response due to multiple unknown sources that create simultaneous stimuli on the system. Moreover, due to technical and economical requirements in some circumstances, only a single sensor is allowed during measurements. Therefore, mechanical system condition assessments using a single measurement is essentially the single channel blind source separation (SCBSS) problem whose task is to extract interpretable signals from the observed signal recorded by a single sensor [171].

The general procedure in SCBSS is first applying a multi-mapping method to decompose the observed signal to equivalent elementary signals followed by a blind source separation step to

[3] A version of this chapter is under review in Mechanical Systems and Signal Processing, Elsevier. Authors: N.T. Do, M. Gül

reconstruct the sources. Wavelet-ICA, EMD-ICA and EEMD-FastICA are typical algorithms for SCBSS [172,173]. Shao *et al.* [172] employed wavelet decomposition and independent component analysis (ICA) to solve the SCBSS problem. First, wavelet decomposition was used to break a single signal into multiple series, then ICA is applied to extract the original signals. With a similar idea, Mijović *et al.* [173] proposed a slightly different approach that uses empirical mode decomposition (EMD) and ICA to recover the source signals from a single observation signal. Recently, Isham *et al.* [174] proposed the application of variational mode decomposition, another decomposition technique that is claimed to surpass the limitation of EMD (i.e. mode mixing and end effect [175]), for rotating machinery diagnosis. The applications on wind turbine gearboxes and bearing outer race fault show that the method is capable of determining the mode number of the signals for fault diagnosis. Other techniques for underdetermined BSS can be found in the literature [176-180].

Overall, the application of SCBSS has been widely used in many scientific and engineering fields. However, it has not been applied in railway engineering thoroughly. For example, track stiffness measurement systems have been introduced to measure vertical track deflections (VTD), as a means of structural health monitoring of railway infrastructures [7,21,103]. The systems show great potentials in monitoring the rail and track conditions [112,181]. However, the following issues prevent their applications from regular maintenance activities [134]:

- Vertical track deflections contain mixed information of track roughness (or track geometry) and deflections due to support stiffness. As the track roughness information in the data is dominant, advanced data analysis techniques are required to accurately reveal the substructure condition.
- The calculation of track modulus is done from the total deflection containing both void deflection and contact deflection although the contact deflection is the only one directly related to the substructure stiffness.

Therefore, analyzing the measured data from the vertical track stiffness measurement systems can be posed as an SCBSS assignment whose outputs could provide information about the track modulus, track geometry, and so on. More importantly, a framework that successfully utilizes the data from vertical track stiffness measurement systems would greatly contribute to standardize their applications in track maintenance routines.

In this study, a hybrid algorithm that employs singular spectrum analysis (SSA) and Algorithm for Multiple Unknown Signals Extraction (AMUSE) technique is proposed to solve the SCBSS problem. Specifically, the combined technique is implemented iteratively to separate the source signals. The organization of the chapter is as follows, In Section 5.3, the theoretical background of the proposed method is described. Next, in Section 5.4, the performance of the proposed method in separating synthetic signals is tested and compared with those of other methods in the literature. In Section 5.5, the method is further validated with the VTD signals extracted from a track model simulated by SIMPACK (a multibody dynamic package) and ABAQUS. Finally, a conclusion section summarizing the method as well as a future plan is presented.

5.3. Methodology

5.3.1. Mathematical description of the single blind source mixing system

A dynamic system is excited by multiple excitations in which the observed response is measured via a single sensor. Depending on the interactions among the source signals, the mixture mechanism can be an instantaneous linear combination or higher-order combinations to produce the multi-channel mixed signal. The mixing model can be described as:

$$x(t) = f\big(s_1(t), s_2(t), \dots, s_n(t)\big) + e(t) \tag{5-1}$$

where $f()$ is the mixing function, $s_i(t)$ is the i-th source signal, $e(t)$ is the measurement noise that has Gaussian distribution with zero mean and σ^2 variance, n denotes the number of source signals. The goal of SCBSS problem is to define the unmixing matrix $\mathbf{W}$ and the source signals from the single mixed signal $\boldsymbol{x}(t)$ only.

$$\mathbf{s}(t) = [s_1(t), s_2(t), \dots, s_n(t)] = x(t) \times \mathbf{W}^{\mathrm{T}} \tag{5-2}$$

To make it possible to solve equation (5-2), the underdetermined blind separation problem is first transformed to a determined problem followed by a blind source separation technique to retrieve the separated signals. In other words, in this study, the single mixed signal $x(t)$ is first transformed into multiple mixed signals using singular spectrum analysis (SSA). Then, the determined blind source separation is performed using the algorithm for multiple unknown signals extraction

(AMUSE) technique. The combined method is applied iteratively on the original signal to extract the sources.

5.3.2. Singular Spectrum Analysis (SSA) for Signal Decomposition

SSA is a time series analysis and forecasting technique with a wide range of applications such as multivariate geometry, dynamical systems. Overall, the main idea of SSA is to decompose a time series into a sum of multiple series. In this section, details about implementing SSA are given. Further background about SSA can be found in the literature and is out of the scope of the chapter [182,183].

Consider a finite real-value series $x(t) = (x_1, x_2, \dots, x_N)$ with N discrete points. The window length L and parameter K are defined that satisfies $1 < L < N$ and $K = N - L + 1$. SSA algorithm follows two main stages (i.e. decomposition and reconstruction) that consist of four steps.

Step 1: Embedding

One-step delay-embedding is performed on the original series $\boldsymbol{x}$ to compute its trajectory matrix $\mathbf{X}$

$$\mathbf{X} = [X_1, X_2, \dots, X_K] = \begin{bmatrix} x_1 & x_2 & x_3 & \cdots & x_K \\ x_2 & x_3 & x_4 & \cdots & x_{K+1} \\ x_3 & x_4 & x_5 & \cdots & x_{K+2} \\ \vdots & \vdots & \vdots & \ddots & \vdots \\ x_L & x_{L+1} & x_{L+2} & \cdots & x_N \end{bmatrix} \tag{5-3}$$

The current delay-embedding configuration produces the trajectory matrix $\mathbf{X}$ that has constant skew-diagonals. Therefore, this step is also known as matrix Hankelization transform.

Step 2: Singular value decomposition

In this step, the trajectory matrix $\mathbf{X}$ is decomposed into L matrices by singular value decomposition (SVD) of $\mathbf{X}$. That is:

$$\mathbf{X} = \sum_{i=1}^{L} \mathbf{X}_i = \sqrt{\lambda_i} U_i V_i^{\mathrm{T}} \tag{5-4}$$

where U_i is the left singular vector, V_i is the right singular vector, and λ_i is the eigenvalues (that are $\lambda_1 \geq \lambda_2 \geq \dots \geq \lambda_L \geq 0$) of the covariance matrix $\mathbf{XX}^{\mathrm{T}}$.

Step 3: Grouping

The expansion in equation (5-4) can be simplified by partitioning the $\mathbf{X}_i$ matrices into I_g subsets such that:

$$\mathbf{X} = \mathbf{X}_{I_1} + \mathbf{X}_{I_2} + \cdots + \mathbf{X}_{I_g} \qquad (5\text{-}5)$$

where $\mathbf{X}_I = \sum_{i \in I} \mathbf{X}_i$ is the elementary matrix of $\mathbf{X}$.

The grouping procedure depends primarily on the singular values of $\mathbf{XX}^{\mathrm{T}}$ matrix whose magnitudes are sorted in descending order and usually appear in pairs.

Step 4: Diagonal averaging

At this final step, each elementary matrix $\mathbf{X}_I$ is transformed into a new series with N elements. For simplicity, let $\mathbf{Y} = \mathbf{X}_I$ with $\mathbf{X}_I \in \mathcal{M}_{L,K}(\mathbb{R})$, $L \le K$. By diagonal averaging the element $y_{l,k}$ of the matrix $\mathbf{Y}$, the corresponding series $\tilde{y} = (\tilde{y}_1, \tilde{y}_2, \ldots, \tilde{y}_s, \ldots \tilde{y}_N)$ is produced:

$$\tilde{y}_s = \begin{cases} \dfrac{1}{k} \displaystyle\sum_{m=1}^{k} y_{m,k-m+1} & \text{for } 1 < k \le L \\ \dfrac{1}{L} \displaystyle\sum_{m=1}^{k} y_{m,k-m+1} & \text{for } L < k \le K \\ \dfrac{1}{N-k+1} \displaystyle\sum_{m=k-K+1}^{N-K+1} y_{m,k-m+1} & \text{for } K < k \le N \end{cases} \qquad (5\text{-}6)$$

Overall, by applying the diagonal averaging (equation (5-6)) to each matrix $\mathbf{X}_I$ in equation (5-5), the original series $x(n)$ is decomposed into a g interpretable component series.

$$x(t) \xrightarrow{\boldsymbol{SSA}} \mathbf{y}(t) = \{y^{(1)}(t), y^{(2)}(t), \ldots, y^{(g)}(t)\}, \qquad \mathbf{y} \in \mathcal{M}_{N,g}(\mathbb{R}) \qquad (5\text{-}7)$$

5.3.3. Algorithm for Multiple Unknown Signals Extraction (AMUSE) technique

The application of SSA helps to transform a signal blind source separation problem into a determined blind source separation problem. Equation (5-2) is rewritten in a new form where both sources and measured signals are in matrix form.

$$\mathbf{s}(t) = \mathbf{y}(t) \times \mathbf{W}^{\mathrm{T}} \qquad (5\text{-}8)$$

where $\mathbf{s}$ and $\mathbf{y}$ are $N \times g$ matrices that contain g sources and observed signals, $\mathbf{W}$ is the $g \times g$ unmixing matrix.

The source **s** and the unmixing matrix **W** can be estimated by second order blind identification (SOBI) techniques by assuming that the sources are weakly uncorrelated and stationary. In this study, AMUSE is employed to develop a hybrid SSA-AMUSE technique for solving the SCBSS problem. AMUSE method was introduced by Tong *et al.* [184] to estimate the unmixing matrices and sources by simultaneously diagonalizing two covariance matrices. The main implementation steps of AMUSE is listed below.

First, the covariance matrix of the observed signals **y** is estimated:

$$\mathbf{R}_y(0) = E\{\mathbf{y}(t)\mathbf{y}^{\mathrm{T}}(t)\} \tag{5-9}$$

where $\mathbf{R}_y(0)$ is the covariance matrix at zero time lag and $t = 1{:}N$ (N is the length of the time series)

Then, the eigenvalue decomposition of $\mathbf{R}_y(0)$ is computed:

$$\mathbf{R}_y(0) = \mathbf{V}_y\mathbf{\Lambda}_y\mathbf{V}_y^{\mathrm{T}} \tag{5-10}$$

where $\mathbf{V}_y$ is the matrix of eigenvectors and $\mathbf{\Lambda}_y$ is the diagonal matrix of eigenvalues in descending order.

Then, whitening transformation is performed:

$$\bar{\mathbf{y}}(t) = \left(\mathbf{V}_y\mathbf{\Lambda}_y^{-\frac{1}{2}}\mathbf{V}_y^{\mathrm{T}}\right)\mathbf{y}(t) = \mathbf{Q}\mathbf{y}(t) \tag{5-11}$$

where $\mathbf{Q}$ is the whitening matrix and $\bar{\mathbf{y}}(t)$ is the whitened matrix.

Then, the covariance matrix with lag τ and the corresponding symmetrized covariance matrix are calculated:

$$\mathbf{R}_{\bar{y}}(\tau) = E\{\bar{\mathbf{y}}(t)\bar{\mathbf{y}}(t-\tau)^{\mathrm{T}}\} \tag{5-12}$$

$$\mathbf{R}_{\bar{y}}^{S}(\tau) = \frac{1}{2}\left(\mathbf{R}_{\bar{y}}(\tau) + \mathbf{R}_{\bar{y}}(\tau)^{\mathrm{T}}\right) \tag{5-13}$$

Finally, eigenvalue decomposition is applied the second time to the symmetrized covariance matrix $\mathbf{R}_{\bar{y}}^{S}(\tau)$ to extract its eigenmatrix **V**. Finally, the unmixing matrix **W** and the separated sources **s** are estimated using:

$$\mathbf{W} = \mathbf{V}^{\mathrm{T}}\mathbf{Q} \tag{5-14}$$

$$\mathbf{s}(t) = \mathbf{y}(t)\mathbf{W}^{\mathrm{T}} \tag{5-15}$$

5.3.4. The proposed hybrid SSA-AMUSE method

Both SSA and AMUSE have been widely employed as blind source separation techniques [185-188]. However, each method inherits both strengths and weaknesses. Specifically, SSA is ideal for trend and seasonality detection although not all source signals are distinguished by these properties. On the other hand, the implementation of AMUSE is straightforward and computer-efficient in comparison with other blind separation techniques that employ joint approximate diagonalization (JAD) to transform the covariance matrix in equation (5-12) [189,190]. The choice of time lag τ can be cumbersome when implementing AMUSE technique, but it provides users a lot of flexibility in evaluating the recovered sources which are estimated by different values of τ. In some specific cases where the unmixed sources are not completely uncorrelated, the application of AMUSE becomes superior. In order to maximize the effectiveness of both techniques, in this study, an iterative framework that combines SSA and AMUSE is proposed to solve the SCBSS problem. The key contribution of the proposed method is that the sources are revealed sequentially from the single mixed signal through an iterative process that cannot be done at once. The algorithm flow of the proposed SSA-AMUSE method is shown in Table 5-1.

Table 5-1. Algorithm flow of the proposed SSA-AMUSE method

- Initialize: $\boldsymbol{x} \in \mathbb{R}^N$: the raw data; *K*: the number of extracted components
- Define the trajectory matrix of $\boldsymbol{x}$

  $\mathbf{X} = [X_1, X_2, \ldots, X_K]$ /* equation (5-3) */
- Define the grouping subsets by examining the singular spectrum of $\mathbf{X}$

  $\boldsymbol{I} = \left\{\mathbf{X}_{I_1}, \mathbf{X}_{I_2}, \ldots, \mathbf{X}_{I_g}\right\}$ /* equation (5-5) */
- **For** $i = 1$ to n
  - Perform SSA on $\boldsymbol{x}$:

    $\boldsymbol{y} = \mathrm{SSA}(\boldsymbol{x}, K, \boldsymbol{I})$ /* §5.3.2 */
  - Perform AMUSE on $\boldsymbol{y}$:

    $\boldsymbol{s} = \mathrm{AMUSE}(\boldsymbol{y}, \tau)$ /* §5.3.3 */
  - Define the residual $\boldsymbol{xr}$:

    $\boldsymbol{xr} = \boldsymbol{x} - \sum \boldsymbol{y}$
  - Update new $\boldsymbol{x}$:

    $\boldsymbol{x} = \boldsymbol{xr}$
- **end**

5.4. Application on synthetic signals

In order to show the effectiveness of the proposed method in a comparative manner, the synthetic signals appearing in He *et al.* [191] are replicated in this chapter. A mixed signal is generated by instantaneously compounding the four synthetic dynamic signals below [191]:

$$s_1 = sign\left(\cos\left(\frac{2\pi f_1 t}{f_s}\right)\right) = \frac{\pi}{4}\sum_{k=1}^{\infty}\frac{\sin(2\pi(2k-1)f_1 t)}{2k-1}$$
$$= \frac{4}{\pi}\left(\sin(2\pi f_1 t) + \frac{1}{3}\sin(2\pi 3 f_1 t) + \frac{1}{5}\sin(2\pi 5 f_1 t)\right) \tag{5-16}$$

where $\omega_1 = 2\pi f_1$

$$s_2 = \sin\left(\frac{2\pi f_2 t}{f_s}\right) \tag{5-17}$$

$$s_3 = \sin\left(\frac{2\pi f_3 t}{f_s}\right) \tag{5-18}$$

$$s_4 = \sin\left(\frac{2\pi f_4 t}{f_s}\right)\sin\left(\frac{2\pi f_5 t}{f_s}\right) \tag{5-19}$$

In the above equations, the sampling frequency f_s = 10,000 Hz, the frequencies of the signals are: f_1 = 155 Hz, f_2 = 80 Hz, f_3 = 90 Hz, f_4 = 9 Hz, f_5 = 300 Hz [191]. The source signals with the length of 4000 samples are shown in Figure 5-1(a-d).

According to equation (5-1), a randomly generated matrix is employed to mix the source signals to produce the mixed signal shown in Figure 5-1(e).

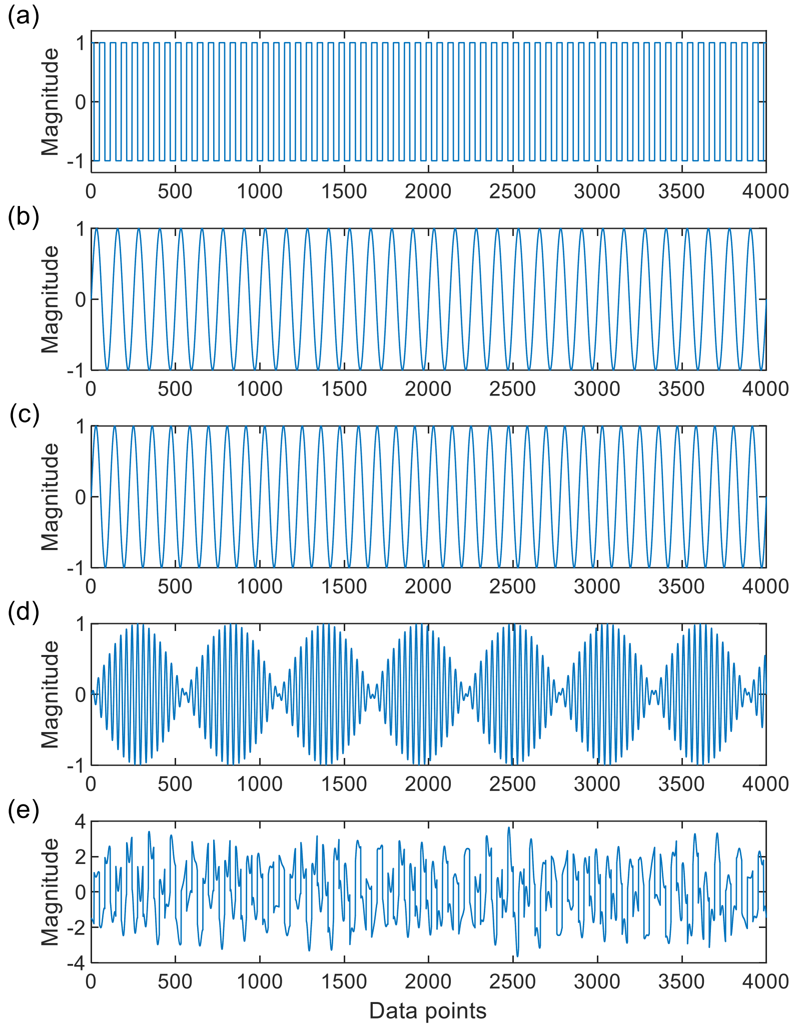

Figure 5-1. The synthetic signals: (a) Source s_1; (b) Source s_2; (c) Source s_3; (d) Source s_4; (e) the mixed signal

The most two important parameters for implementing the SSA method is the window length (L) resulting in the number of decomposed series (K) and the clustering group for the reconstruction of the time series components. The heuristic is that increasing K will result in further levels of decompositions that are corresponding to noise, trend, sinusoidal decompositions respectively [192]. In the current application, half of the mixed source length is chosen to be K, a relatively large number of components to be extracted from the mixed signal as the purpose is to define the original sinewave signals.

Besides, the third step (grouping) in the SSA process requires attention to assign the signals to be grouped for the final reconstruction step. Although the grouping step gives users the freedom of choice, it can be done by examining the singular spectrum (i.e. eigenvalue spectrum) of the trajectory matrix. For instance, the singular spectrum plot in Figure 5-2 clearly shows several steps composed by the pairs of eigenvalues. Through this observation, it is decided that two consecutive matrices $\mathbf{X}_i$ and $\mathbf{X}_{i+1}$ (equation (5-4)) are grouped together. It is noted also that only the first three sources are extracted in each iteration of the proposed method (Table 5-1). As the number of iterations increases, the sources will be eventually recovered.

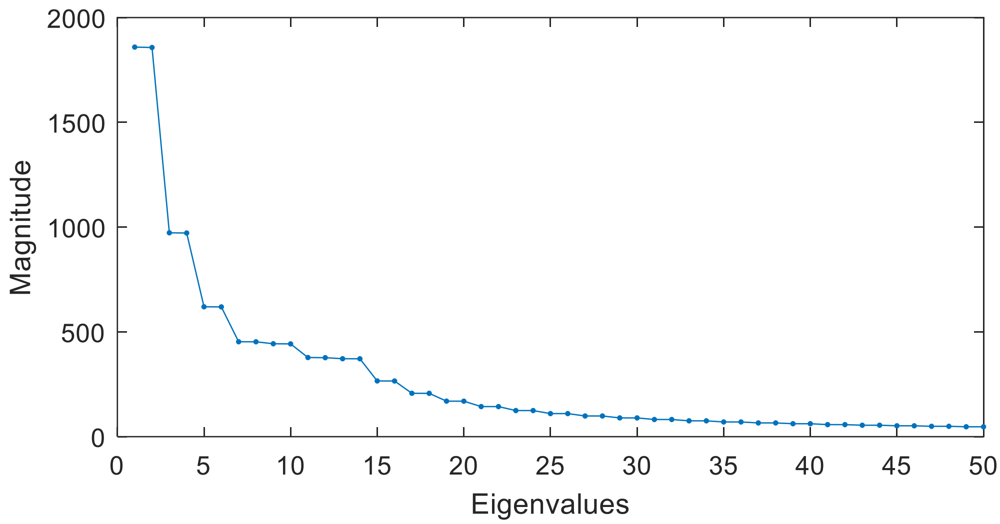

Figure 5-2. First 50 eigenvalues of the trajectory matrix of the mixed signal

Figure 5-3 and Figure 5-4 not only show the typical results of SSA and AMUSE analysis in an iteration but also demonstrate the novelty of the proposed method. In Figure 5-3, the application of SSA on a single signal results in three individual signals (i.e. ssa_1, ssa_2, ssa_3), which still appear to have some degrees of correlations, especially between ssa_2 and ssa_3. Specifically, ssa_2 is similar to ssa_3 in both time and frequency domain with the power spectral density (PSD) functions peaking around 290 and 310 Hz.

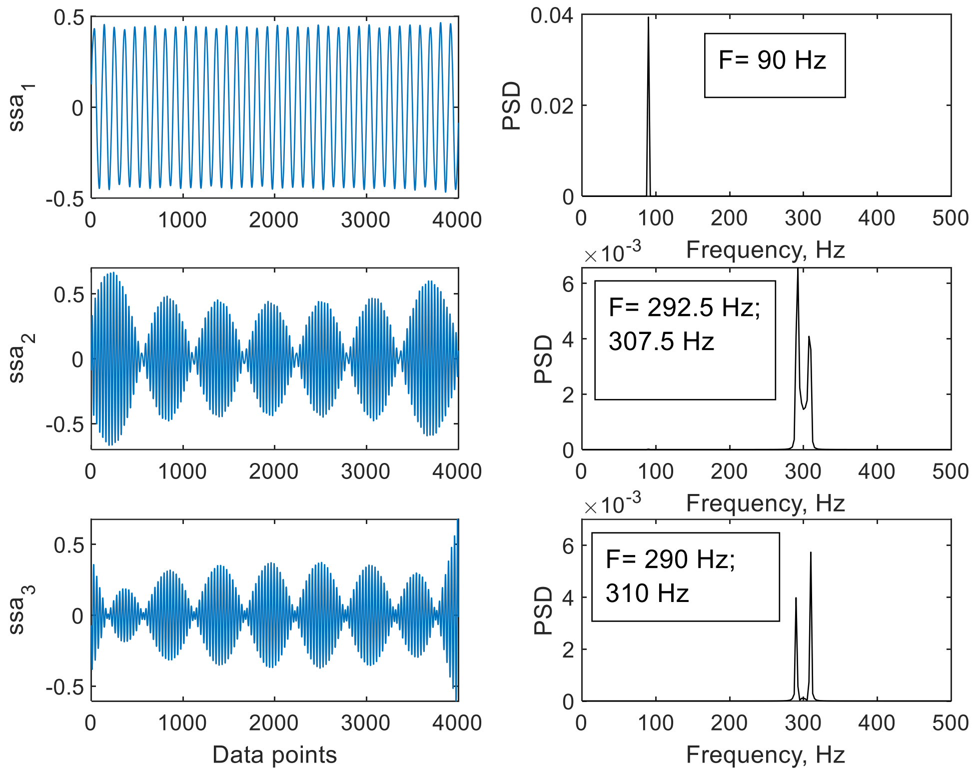

Figure 5-3. The extracted SSA components and corresponding PSD

The application of AMUSE on the SSA components (Figure 5-3) helps to further separate the signals to obtain the original ones. As recommended by Cichocki and Amari [193] and Miettinen *et al.* [194], different values for τ are tested and it is found that the time lag $\tau = N/6 = 666$ produces the most effective results. As can be seen from Figure 5-4, the first recovered signal ($amuse_1$) is deemed to be the original signal s_4 as their pattern and frequencies are almost the same. Similarly, the signal $amuse_2$ matches well with the source signal s_3. The last signal ($amuse_3$) is relatively similar to the first $amuse_1$ signal in both time and frequency domain. However, it is not considered as a recovered separated source as its characteristics are not as clear as those of $amuse_1$. Quantitatively, comparisons between the recovered and original signals are tabulated in Table 5-2 where there is no difference in the frequencies between identified signals and the source signals.

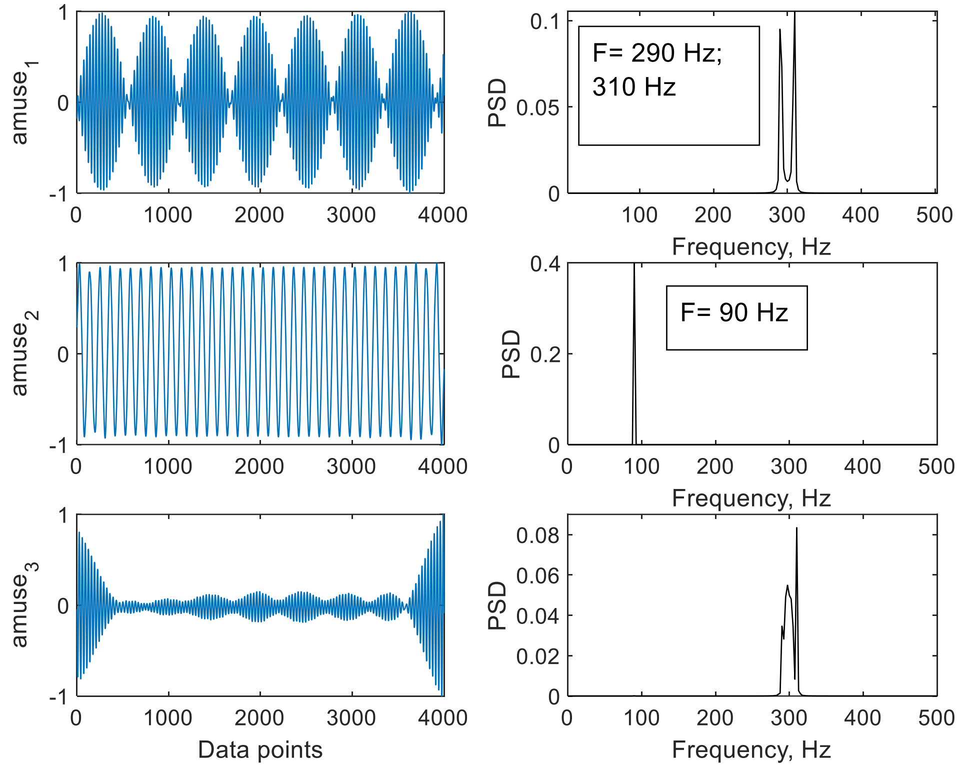

Figure 5-4. The separated signals and the corresponding PSD after applying AMUSE

The final separated sources after three iterations are shown in Figure 5-5. As can be seen from the figure, the source signals s_2, s_3, s_4 are recovered as they match well with the original sources in Figure 5-1. Quantitively, the signal interference ratio (SIR) of the original signals s_2, s_3, s_4 and their recovered signals is computed to be 46.5 dB which is comparable to 35 dB the quantity from the method proposed by He *et al.* and the other EMD-ICA, wavelet-ICA methods cited in the same paper [191].

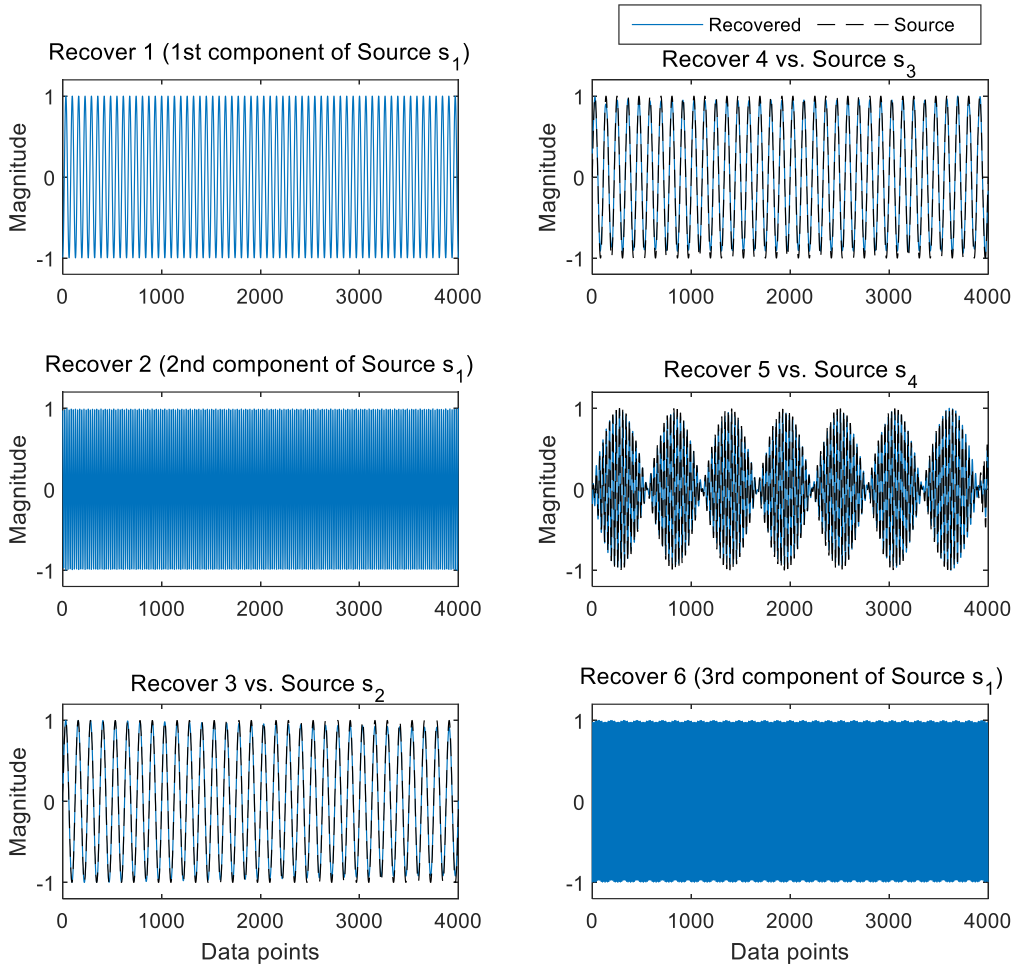

Figure 5-5. Separated normalized sources after three iterations

As shown in Table 5-2, it is clear that all signals are successfully recovered and separated as there is no error in the recovered frequencies. It is worth noting that additional signals are also revealed and reconstructed as the iteration process continues. The frequencies of these additional signals are always a factor of the first frequency (f_1) of the square signal (s_1). This finding agrees well with equation (1) where a square signal is actually an infinite sum of sinewave signals.

Table 5-2. Identified frequencies of the separated signals

Signal number	**Identified f (Hz)**	**Original f (Hz)**	**Error (%)**
1	155	155 (first component of signal s_1)	0
2	80	80 (signal s_2)	0
3	465 (= 3×155)	465 (second component of signal s_1)	0
4	290; 310	290; 310 (signal s_4)	0
5	90	90 (signal s_3)	0
6	775 (= 5×155)	775 (third component of signal s_1)	0

5.5. Application on dynamic rail track models

In this study, the proposed SCBSS technique is applied to VTD signals to examine the subgrade stiffness. It is noted that although VTD can be measured by many track stiffness measurement systems [7,9,97,195], the relative deflection signal analogous to that measured by MRail system is simulated in this study to validate the current study. MRail is a continuous track stiffness measurement system developed at the University of Nebraska-Lincoln under the sponsorship of the Federal Railroad Administration [21]. The relative vertical rail deflection (Y_{rel}) between the rail-wheel contact line and the rail surface at 1.22 m from the nearest axle is measured by the system which is then used for track condition assessments. The system has shown a lot of advantages in assessing track over long distances [25,110,112,132]. As noted in Section 5.2, on the other hand, Y_{rel} may consist of mixed information and therefore the corresponding track modulus can not be observed clearly from the raw signal. In this context, the method in the current study is proposed to examine the track stiffness from Y_{rel} signal under the effects of track geometry and varying track modulus. The purpose of the proposed methodology is two folds: to retrieve track modulus and track geometry information separately from the Y_{rel} data.

The Y_{rel} data is simulated with a dynamic rail-track model developed using multibody dynamic simulation software, SIMPACK. The system consists of three wheelsets, crossties, and flexible rails supported by discrete supports having varying track modulus. Note that a light load (5kN) is applied at the third wheelset that is located at 1.22 m from the middle wheelset. With the current configuration, the wheel-rail contact can be always ensured and the relative deflection (Y_{rel}) can be extracted by using deflections of the three wheelsets. Regarding the flexible rail parts, a finite element model (FEM) of a rail (RE100 profile) is created in ABAQUS and its substructure is generated with different retained nodes evenly distributed at 300 mm spacing on the railhead and

600m spacing on the rail base. Subsequently, the substructure model of the rail is imported to SIMPACK to create a flexible track model. A demonstration of the model is shown in Figure 5-6. Note that the red lines are the two FEMs. For computing efficiency and license resources, the total length of the rail part is 52.8 m and only the middle segment from 5m to 45m is studied.

(a)

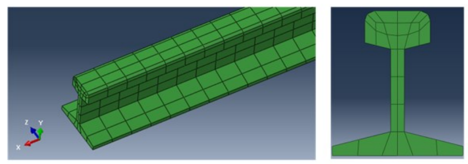

(b)

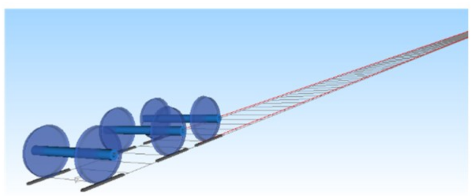

(c)

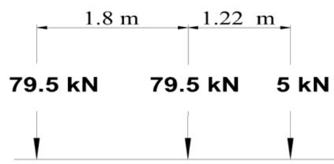

Figure 5-6. (a-b) Abaqus rail model; (c) SIMPACK model with a flexible track; (d) wheelset locations

To validate the modeling process, deflections from the numerical model were compared with those obtained from the Winkler model. As can be seen from Figure 5-7(a), the deflections (at the applied loads) given by the numerical simulation are slightly larger than those given by Winkler model, although they follow the same pattern. This behavior agrees well with an on-site experiment conducted by Lu, S. [8], where the actual rail deflections were captured by a video camera. It is worth noting that the deflection given by SIMPACK model is slightly asymmetric at the given wheelset locations. It is because of the loading configurations and the back wheelset is right above the tie, whereas the second one is standing between two ties. The zigzag pattern of Y_{rel} (Figure 5-7(b)) extracted from the SIMPACK model is due to the discrete spring supports.

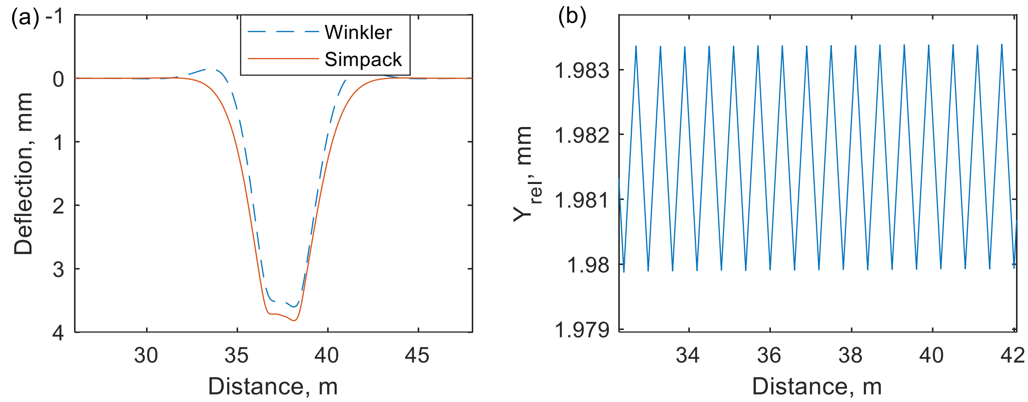

Figure 5-7. (a) Rail deflections from SIMPACK and Winkler models; (b) Y_{rel} extracted from SIMPACK model

Regarding track geometry, the analytical forms in terms of random irregularity power spectrum proposed by the Federal Railroad Administration (FRA) of the U.S. are employed. Specifically, the irregularities of track geometry are defined by six levels as detailed below [196].

The power spectrum density functions are shown below:

$$S_v(\omega) = \frac{(kA_v\omega_c^2)}{(\omega^2+\omega_c^2)\omega^2}\ (cm^2/rad/m) \tag{5-20}$$

$$S_a(\omega) = \frac{(kA_a\omega_c^2)}{(\omega^2+\omega_c^2)\omega^2}\ (cm^2/rad/m) \tag{5-21}$$

$$S_c(\omega) = \frac{(4kA_v\omega_c^2)}{(\omega^2+\omega_c^2)(\omega^2+\omega_s)}\ (cm^2/rad/m) \tag{5-22}$$

where $S_v(\omega)$, $S_a(\omega)$, $S_c(\omega)$ are track irregularity power spectral density functions for track profile, alignment, and cross-level (rad/m), ω is the spatial frequency (rad/m), ω_c, and ω_s are cutoff frequency (rad/m), A_v and A_a are roughness coefficients (cm^2·rad/m), which vary depending on irregularity levels (Table 5-3). The constant k is 0.25.

Table 5-3. Values of the parameters for FRA track irregularity power spectral density function

Parameters	**Levels and the corresponding values**					
	1	2	3	4	5	6
A_v (mm^2 rad/m)	12107	10181	6816	5376	2095	339
A_a (mm^2 rad/m)	33634	12107	4128	3027	762	339
ω_s (rad/m)	0.6046	0.9308	0.852	1.1312	0.8209	0.438
ω_c (rad/m)	0.8245	0.8245	0.8245	0.8245	0.8245	0.8245

Random samples to the track irregularity are determined from the trigonometric series below

$$r(x_k) = \sqrt{\frac{2}{N}} \times \sum_{k=1}^{N} \sqrt{S(\omega_k)\Delta\omega} \times \cos(\omega_k x_k + \phi_k) \tag{5-23}$$

where

x_k is the spatial location along the track

ω_k is the discrete frequency in the PSD functions.

ϕ_k is the random phase angle uniformly distributed over $[0, 2\pi]$

As per discussion in related studies [133,143], the vertical profile has the most influence on Y_{rel} readings. Therefore, the current study considers the vertical profile as the factor that is mixed with the track modulus in the Y_{rel} measurements.

5.5.1. Case study 1: Track model with imperfect sinewave track modulus

In this case, a random vertical profile is generated and inputted to the track model together with a sinewave track modulus. Note that the inputted sinewave track modulus is added with artificial noise to better represent uncertainties in the measurement system. The purpose is to justify the accuracy of the extracted Y_{rel} signal in identifying the track modulus. The inputted values and the corresponding Y_{rel} are demonstrated in Figure 5-8.

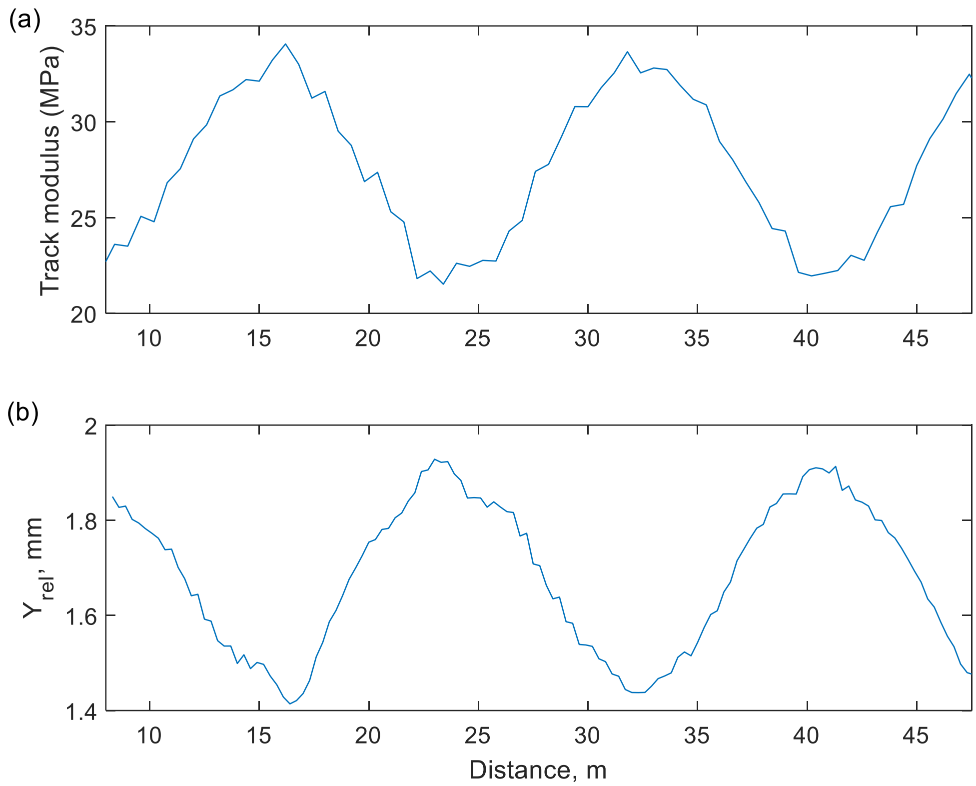

Figure 5-8. (a) The inputted sinewave track modulus (with noise); (b) the Y_{rel} signal

Intuitively, the Y_{rel} signal in Figure 5-8 clearly shows a strong correlation with the inputted track modulus where high values of support stiffness result in low deflections (Y_{rel}). The blind separation process is now conducted on the Y_{rel} signal which mainly contains the track modulus information in this case. Similar to the previous application, the procedure in Table 5-1 is followed by first defining the level of SSA decomposition. Although there is no rule for deciding the window length (L), it is recommended that sufficiently detailed elementary series (K) can be achieved when $L \approx N/2$ [182]. In the current application, since the length of the raw Y_{rel} data is relatively short ($N = 135$) and since the aim is to identify only one to two types of separate sources of information (i.e. track modulus and track geometry), only 10 elementary series are decomposed by the SSA process. Finally, the AMUSE technique with 2 time lags, one of the typical values used in the literature for AMUSE method [121,194], is deployed to extract the final separated signals.

Figure 5-9 shows the resulting signals after a single iteration. First of all, the global sinewave characteristic of the track modulus is not only revealed but also further sharpened to better reflect the actual sinusoidal pattern of the inputted track modulus (Figure 5-9(a)). Most importantly, the application of the proposed SSA-AMUSE method continues to show the localized effects of the discrete spring supports which is shown in Figure 5-9(b), the zig-zag pattern in the second separated signal reflects the discontinuity of the rail supports. It is worth mentioning that the effect of discrete spring supports is completely faded in the raw Y_{rel} signal as the varying track modulus effect is overwhelming. The proposed method has successfully revealed the two inherent properties of the track model i.e. sinewave track modulus variations and discrete spring supports.

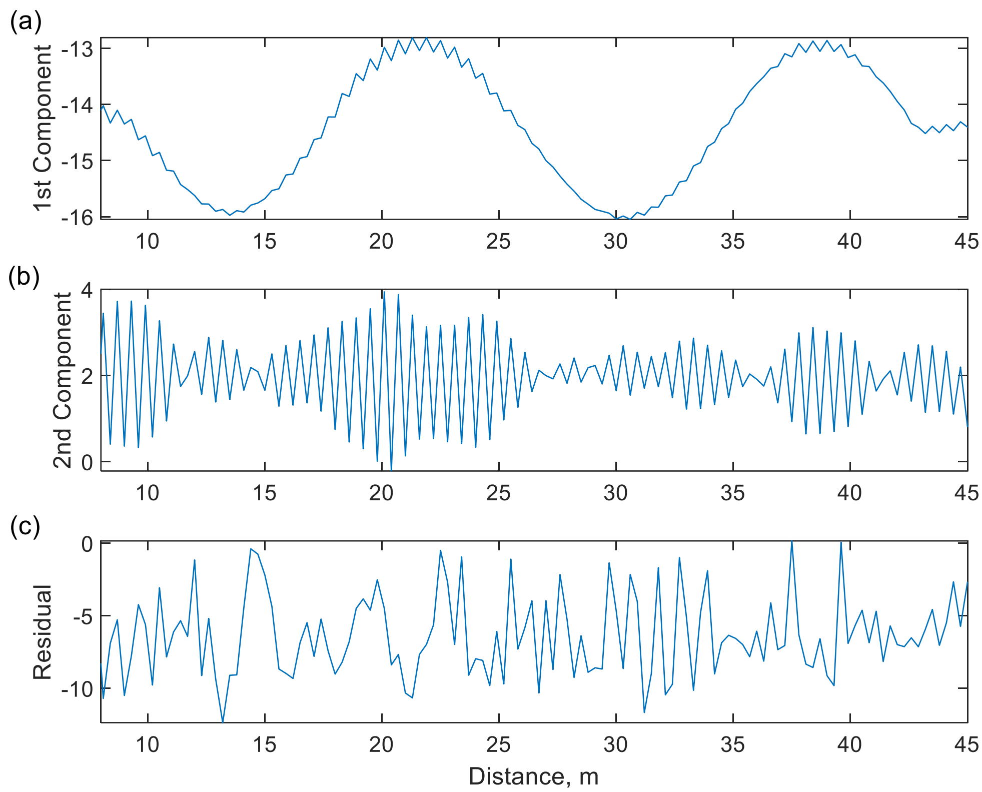

Figure 5-9. The separated signals computed by the proposed method

5.5.2. Case study 2: Track model with random vertical profile + random track modulus

In this case, a more complicated scenario is simulated where both track modulus and vertical profile are randomly generated and inputted to the track model. A Class 6 random vertical profile, the inputted track modulus and the corresponding Y_{rel} are shown in Figure 5-10.

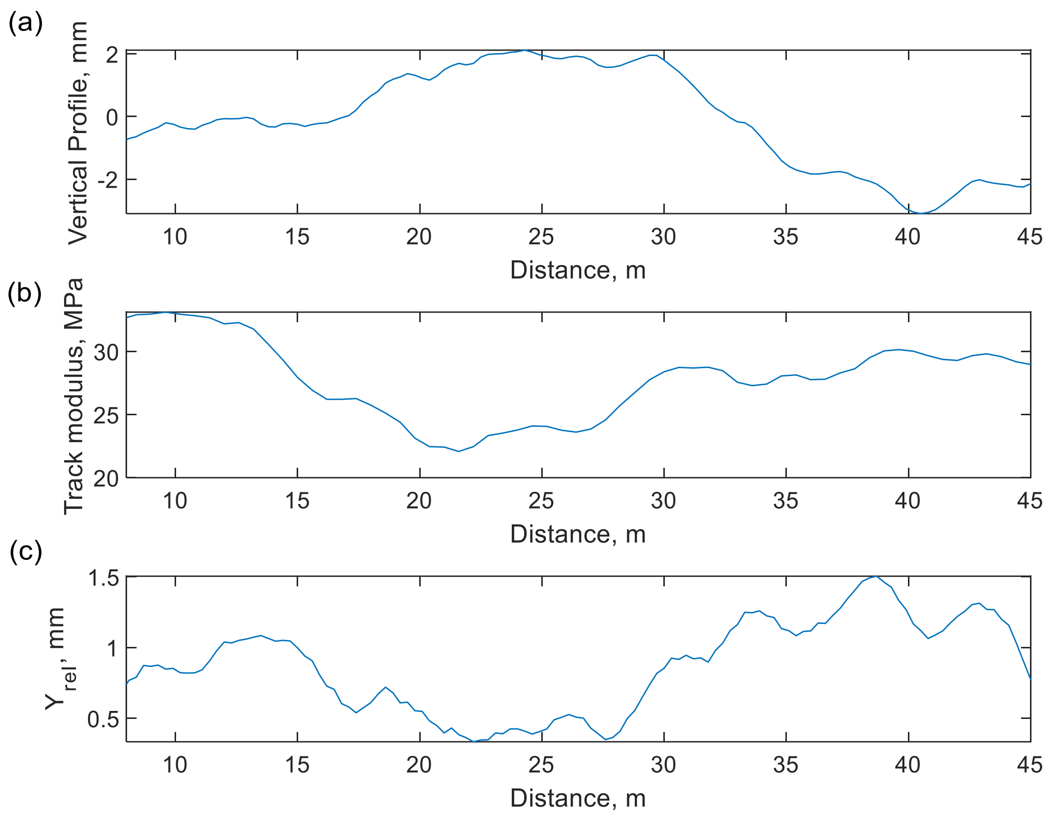

Figure 5-10. (a-b) The inputted track parameters; (c) the extracted Y_{rel} signal

The same procedure is applied to extract the two separated signals from Y_{rel}. The resulting two source signals which are relevant to the track modulus and vertical profile are shown in Figure 5-11. It can be observed that the two separated sources successfully indicate the variations of both track modulus and vertical profile. On the other hand, however, the magnitudes of track modulus and vertical profile are not well reflected by the recovered sources. The results are deemed successful as the patterns and variations of the sources are well captured. Unfolding the variations of track modulus enables a valid establishment of a function approximation to estimate the actual values of track modulus from the processed Y_{rel} (which is the first separated signal in this case) [197]. It is also shown in the current simulated model that the ability of the method in separating the track modulus is less effective as the level of track geometry variations increases. It is expected as the mixing mechanism of track modulus and track geometry source becomes more complicated. Therefore, further investigations of real-life measurements would be needed to confirm the levels that track geometry present in Y_{rel} data.

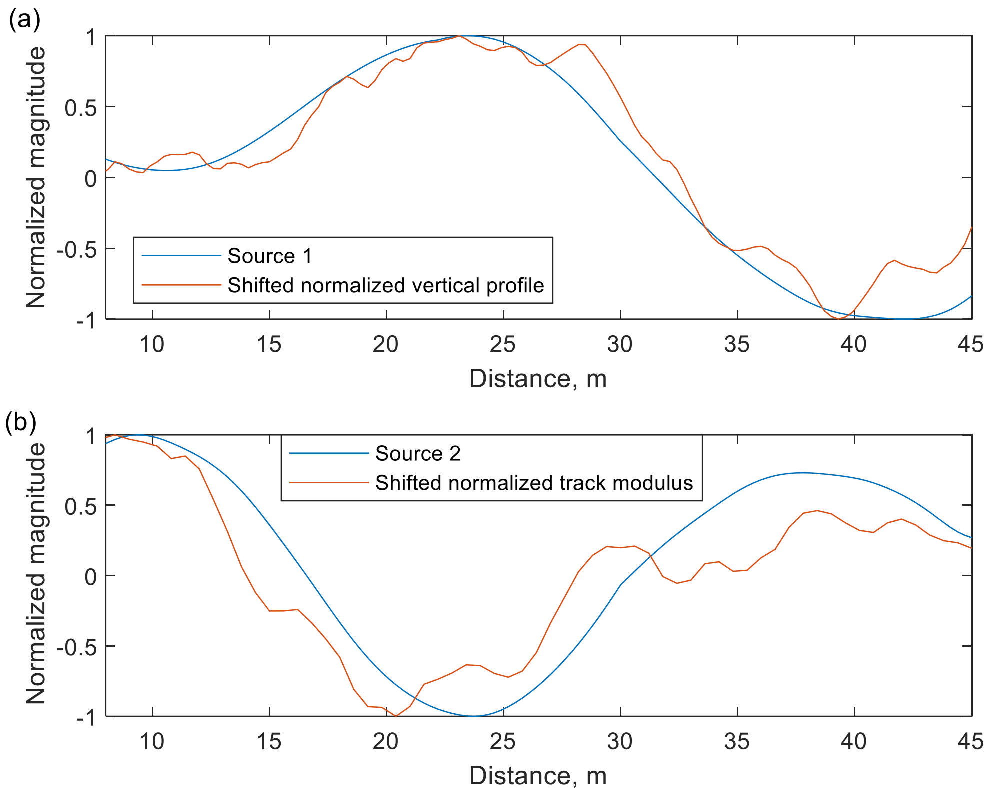

Figure 5-11. Comparisons: (a) the inputted track geometry vs. source 1; (b) track modulus vs. source 2

5.6. Conclusions

In this chapter, a recursive SSA-AMUSE algorithm that is capable of separating a single channel instantaneous mixing signal is proposed. The single channel observation is first mapped into multi-channel signals to transform an underdetermined blind source separation problem to determined blind source separation. AMUSE technique is subsequently applied to the processed multi-channel signals to define the original sources. Importantly, implementing the proposed SSA-AMUSE method in an iterative process provides superior results as the original sources are eventually peeled off from the observed signal. The applications of the proposed method on various synthetic signals previously used in the literature and Y_{rel} data confirm that the original signals are successfully reconstructed. The method puts a step forward in promoting the application of track stiffness measurement systems as it is the first time blind source separation is introduced to the Y_{rel} measurements for investigating track modulus variations. In the next chapter, a further development of the current method is proposed and validated with real-life Y_{rel} data.

Chapter 6: A Hybrid Single Channel Blind Source Separation Technique for Extracting Track Geometry and Stiffness with a Real-life Application[4]

6.1. Overview

This chapter presents a single channel blind source separation (SCBSS) technique for evaluating track support conditions and track geometry using vertical track deflection data measured by a continuous track stiffness measurement system. A track flexibility index and an estimated track quality index are computed from the separated signals extracted from the measured deflection data using singular spectrum analysis and algorithm for multiple unknown signals extraction. The application of the proposed method on the field data recorded from a revenue track shows that the variations in the track stiffness as well as the variations in the vertical track profile are successfully evaluated. Contrary to the assumption that the vertical profile is the primary geometric factor affecting the readings of continuous track stiffness measurement systems, our investigation shows that superelevation significantly influences the measurement system and thus the measured data. This finding can be a significant contribution to the development of other continuous track stiffness measurement systems where deflections are computed using indirect methods.

6.1. Introduction

Measuring vertical track deflections is a common task in investigating the vertical track stiffness, one of the factors contributing to the deterioration of track geometry, rail failures, and other superstructure components [82]. In the railway engineering literature, track stiffness and track modulus are the two common parameters to quantify the track foundation. Different continuous and standstill systems were developed and claimed to be capable of providing track stiffness information. A standstill system collects the total deflection at predefined points on the track under known applied loads from which the total track stiffness can be calculated. The main advantage of standstill systems is that the track stiffness can be defined accurately, whereas its disadvantage is that repeating the test at multiple locations is time-consuming and requires track closure. The common commercial systems include impact hammer method, falling weight deflectometer, track

[4] A version of this chapter will be submitted to Journal of Rail and Rapid Transit. Authors: N.T. Do, M. Gül, M.T. Hendry

loading vehicle [89,198,199]. In addition, there are other methods that utilize digital image correlation, multi-depth deflectometers, and LVDT to define the total track deflection [200,201]. On the other hand, due to the ability of taking vertical track deflection (VTD) measurements over a railway network level, continuous track stiffness measurement systems are necessary for track maintenance and monitoring. Different systems have been developed in various parts of the world, such as China, Europe, and North America, and these systems generally use either laser sensors or vibration sensors to measure the VTD [7,9,97,195]. It should be noted that the total VTD outputted by the measurement systems is a combination of different parameters such as void deflection, track geometry variations, and vertical stiffness of different subgrade layers [134]. Therefore, it is important to fully investigate factors affecting the track deflection data measured by such systems so that the contact deflection due to track stiffness can be identified. In this chapter, in particular, the data measured by a continuous stiffness measurement system known as MRail is investigated.

The MRail system was developed by the researchers at the University of Nebraska-Lincoln (UNL) [195]. Different studies have been conducted on the system to investigate the effects of track geometry and its ability in providing information about the track stiffness [21,22,25,110,111,132,141,143,197]. It was shown that there was a significant correlation between the measured data and track geometry although the relationship was not successfully quantified. In order to minimize the effects of track geometry and surface imperfections, the moving average of the measured data and its first derivative have been used to map the subgrade conditions [112,132,141]. By using the method, the locations of soft foundation such as muskeg formation and its variations were successfully identified [112]. However, as moving average approach is used to remove short wavelength irregularities in the MRail data, further techniques are worth investigated to deal with the long wavelength components which contains not only track stiffness information but also other unknown information. Therefore, defining the main factors that affect the collected VTD (referred to Y_{rel}) recorded by the MRail system should be rigorously studied so that the track stiffness can be successfully identified. Fully understanding the factors affecting Y_{rel} data and establishing an appropriate method for defining the track stiffness variations are key challenges that prevent the widespread application of continuous stiffness measurement systems. Although different studies have shown that the Y_{rel} data can be used to examine the variations of track stiffness and subgrade conditions [24,108,109,112], investigation on the effects of track geometry and other factors on Y_{rel} remains limited. An analytical test conducted by Lu *et al.* [143] concluded that only large vertical geometry defects over a short length significantly affects the Y_{rel} readings. On the other hand, Roghani *et al.* [113] showed that there is a significant correlation between statistical distributions of the track geometry and $Y_{rel.}$ Moreover, Mehrali *et al.* [132] conducted a field study on Y_{rel} data and track geometry to investigate the levels of their correlations. The authors found that the track alignment (the lateral deviation of the gauge side from a reference line measured from its midpoint location) has the highest correlation with Y_{rel} data.

As Y_{rel} data contains mixed information coming from track geometry, track stiffness, and track surface imperfections, it can be posed as a single channel blind source separation (SCBSS) problem whose main objective is to recover the original signals that were mixed in a single observation. The current study proposes a new solution for SCBSS problem by utilizing Singular spectrum analysis (SSA) and Algorithm for Multiple Unknown Signals Extraction (AMUSE). The advance of the method is that all required parameters for SSA are self-identified due to the use of AMUSE technique. Another contribution of the current study is that the blind source separation concept is introduced to track structure health monitoring to promote the use of a continuous track stiffness measurement system. The results from the field test conducted on a revenue mainline show that the proposed method is also successful in examining the track geometry and track stiffness variations by two separated signals. In addition, it is also shown that the superelevation has a significant influence on the measured data. This finding is important as superelevation was discovered as an influential factor in the continuous track stiffness measurement system for the first time in the literature.

6.2. Methodology

6.2.1. Mathematical description of the single channel mixing system

In many practical situations, a single sensor is used to record multidimensional outputs of a dynamic system. The linear instantaneous mixture acquired by the sensor can be described as:

$$x(t) = \sum_{i=1}^{n} a_i s_i(t) + e(t) \tag{6-1}$$

where a_i is the mixing coefficient, $s_i(t)$ is the i-th source signal, $e(t)$ is the measurement noise, n denotes the number of source signals. The goal of single channel blind source separation problem is to define the unmixing matrix **W** and the source signals from the single mixed signal $x(t)$ only (equation (6-2)).

$$\mathbf{s} = [s_1(t), s_2(t), \dots, s_n(t)] = x(t) \times \mathbf{W}^{\mathrm{T}} \tag{6-2}$$

In general, the SCBSS problem is resolved by transforming the observed signal into a combination of multiple signals. Then, a blind source separation (BSS) technique can be applied to the decomposed signals to recover the sources. In this study, the decomposition step is achieved by singular spectrum analysis (SSA), whereas the algorithm for multiple unknown signals extraction (AMUSE) technique is used to solve the BSS problem. In the current study, both SSA and AMUSE can be implemented after all free parameters are defined automatically (which will be discussed in the next sections).

6.2.2. Singular Spectrum Analysis (SSA) for Signal Decomposition

SSA is a time series analysis that is widely known for its ability in signal decomposition, forecasting and gap filling estimation [182]. Overall, the main idea of SSA is to decompose a time series into a sum of multiple series. In this section, details about implementing SSA is given. Further detailed discussion about SSA is not in the scope of this chapter and can be found in the literature [182,183].

Consider a finite real-value series $x = (x_1, x_2, \dots, x_N)$ with N discrete points. The two main parameters of SSA are the window length L and parameter K (the number of decomposed signals) that satisfy $1 < L < N$ and $K = N - L + 1$. SSA algorithm follows two main stages (i.e. decomposition and reconstruction) that consist of four steps: (1) embedding, (2) singular value decomposition, (3) grouping, and (4) diagonal averaging.

Step 1: Embedding

One-step delay-embedding is performed on the original series x to compute its trajectory matrix **X**

$$\mathbf{X} = [X_1, X_2, \dots, X_K] = \begin{bmatrix} x_1 & x_2 & x_3 & \cdots & x_K \\ x_2 & x_3 & x_4 & \cdots & x_{K+1} \\ x_3 & x_4 & x_5 & \cdots & x_{K+2} \\ \vdots & \vdots & \vdots & \ddots & \vdots \\ x_L & x_{L+1} & x_{L+2} & \cdots & x_N \end{bmatrix} \tag{6-3}$$

where $X_i = (x_i, \dots, x_{i+L-1})^T$ with $1 \le i \le K$ denotes the lagged vector.

The current delay-embedding configuration produces the trajectory matrix **X** that has constant skew-diagonals. Therefore, this step is also known as matrix Hankelization transform.

Step 2: Singular value decomposition

In this step, the trajectory matrix **X** is decomposed into L matrices by singular value decomposition (SVD) of **X**. That is:

$$\mathbf{X} = \sum_{i=1}^{L} \mathbf{X}_i = \sum_{i=1}^{L} \sqrt{\lambda_i} U_i V_i^{\mathrm{T}} \tag{6-4}$$

where U_i is the left singular vector, V_i is the right singular vector, and λ_i is the eigenvalues (that are $\lambda_1 \geq \lambda_2 \geq \ldots \geq \lambda_L \geq 0$) of the covariance matrix $\mathbf{XX}^{\mathrm{T}}$.

Step 3: Grouping

The expansion in equation (6-4) can be simplified by partitioning the **X** matrix into I_g subsets such that:

$$\mathbf{X} = \mathbf{X}_{I_1} + \mathbf{X}_{I_2} + \cdots + \mathbf{X}_{I_g} \tag{6-5}$$

where $\mathbf{X}_I = \sum_{i \in I} \mathbf{X}_i$ is the elementary matrix of **X**.

The grouping procedure depends primarily on the singular values of $\mathbf{XX}^{\mathrm{T}}$ matrix whose magnitudes are sorted in descending order, and usually appear in pairs.

Step 4: Diagonal averaging

At this final step, each elementary matrix $\mathbf{X}_I$ is transformed to a new series with N elements. For simplicity, let $\mathbf{Y} = \mathbf{X}_I$ with $\mathbf{X}_I \in \mathcal{M}_{L,K}(\mathbb{R})$, $L \leq K$. By diagonal averaging the element $y_{l,k}$ of the matrix **Y**, the corresponding series $\tilde{y} = (\tilde{y}_1, \tilde{y}_2, \ldots, \tilde{y}_s, \ldots \tilde{y}_N)$ is produced:

$$\tilde{y}_s = \begin{cases} \dfrac{1}{k} \displaystyle\sum_{m=1}^{k} y_{m,k-m+1} & \text{for } 1 < k \leq L \\ \dfrac{1}{L} \displaystyle\sum_{m=1}^{k} y_{m,k-m+1} & \text{for } L < k \leq K \\ \dfrac{1}{N-k+1} \displaystyle\sum_{m=k-K+1}^{N-K+1} y_{m,k-m+1} & \text{for } K < k \leq N \end{cases} \tag{6-6}$$

Overall, by applying the diagonal averaging (equation (6-6)) to each matrix $\mathbf{X}_I$ in equation (6-5), the original series $x(t)$ is decomposed into g interpretable component series.

$$x(t) \xrightarrow{SSA} \mathbf{y}(t) = \{y^{(1)}(t), y^{(2)}(t), \ldots, y^{(g)}(t)\}, \qquad \mathbf{y} \in \mathcal{M}_{N,g}(\mathbb{R}) \tag{6-7}$$

6.2.3. Algorithm for Multiple Unknown Signals Extraction (AMUSE) technique

The application of SSA helps to transform a unidimensional signal into multiple elementary signals. Equation (6-2) is rewritten in a new form where both sources and measured signals are in matrix form.

$$\mathbf{s}(t) = \mathbf{y}(t) \times \mathbf{W}^{\mathrm{T}} \tag{6-8}$$

where $\mathbf{s}$ and $\mathbf{y}$ are $N \times g$ matrices that contain g sources and observed signals, $\mathbf{W}$ is the $g \times g$ unmixing matrix.

The source $\mathbf{s}$ and the unmixing matrix $\mathbf{W}$ can be estimated by second order blind identification (SOBI) techniques by assuming that the sources are weakly uncorrelated and stationary. In this study, AMUSE technique is employed to develop a hybrid SSA-AMUSE technique for single blind source identification. AMUSE method was introduced by Tong *et al.* [184] to estimate the unmixing matrices and sources by simultaneously diagonalizing two covariance matrices. The main implementation steps of AMUSE is listed below.

First, the covariance matrix of the observed signal $\mathbf{y}$ is estimated:

$$\mathbf{R}_y(0) = E\{\mathbf{y}(t)\mathbf{y}^{\mathrm{T}}(t)\} \tag{6-9}$$

where $\mathbf{R}_y(0)$ is the covariance matrix at zero time lag.

Then, the eigenvalue decomposition of $\mathbf{R}_y(0)$ is computed:

$$\mathbf{R}_y(0) = \mathbf{V}_y \boldsymbol{\Lambda}_y \mathbf{V}_y^{\mathrm{T}} \tag{6-10}$$

where $\mathbf{V}_y$ is the matrix of eigenvectors and $\boldsymbol{\Lambda}_y$ is the diagonal matrix of eigenvalues in descending order.

Then, whitening transformation is performed:

$$\bar{\mathbf{y}}(t) = \left(\mathbf{V}_y \boldsymbol{\Lambda}_y^{-\frac{1}{2}} \mathbf{V}_y^{\mathrm{T}}\right) \mathbf{y}(t) = \mathbf{Q}\mathbf{y}(t) \tag{6-11}$$

where $\mathbf{Q}$ is the whitening matrix and $\bar{\mathbf{y}}(t)$ is the whitened matrix.

Then, the covariance matrix with lag τ and the corresponding symmetrized covariance matrix are calculated:

$$\mathbf{R}_{\bar{y}}(\tau) = E\{\bar{\mathbf{y}}(t)\bar{\mathbf{y}}(t-\tau)^{\mathrm{T}}\} \tag{6-12}$$

$$\mathbf{R}_{\bar{y}}^{S}(\tau) = \frac{1}{2}\left(\mathbf{R}_{\bar{y}}(\tau) + \mathbf{R}_{\bar{y}}(\tau)^{\mathrm{T}}\right) \tag{6-13}$$

Eigenvalue decomposition is applied the second time to the symmetrized covariance $\mathbf{R}_{\bar{y}}^{S}(\tau)$ to extract its eigenmatrix $\mathbf{V}$. Finally, the unmixing matrix $\mathbf{W}$ and the separated sources $\mathbf{s}$ are estimated:

$$\mathbf{W} = \mathbf{V}^{\mathrm{T}}\mathbf{Q} \tag{6-14}$$

$$\mathbf{s} = \mathbf{y}\mathbf{W}^{\mathrm{T}} \tag{6-15}$$

6.2.4. The proposed hybrid SSA-AMUSE method

Both SSA and AMUSE have been widely employed in blind source separation problems [185-188]. SSA is well known for decomposing a signal into trend and seasonality components. On the other hand, AMUSE is a blind source separation technique that is popular due to its straightforward implementation process [189,190]. In addition, the choice of time lag τ provides users a lot of flexibility in evaluating the recovered sources when implementing AMUSE technique. In this study, τ is chosen to be 1 (a common value for AMUSE) throughout the analysis. On the other hand, the choice of SSA parameters is cumbersome as there is no universal rule for it [182]. In this context, the application of AMUSE is considered an ideal supplement to SSA as it helps to define the optimized SSA parameters. In this study, the key constraint in the method's algorithm is that the first SSA and AMUSE components (which is called SSA_1 and $AMUSE_1$ respectively) must be close to each other as much as possible. By implementing the AMUSE and SSA techniques with different values of *K*, the final parameters of the proposed method can be finalized by examining the difference between the first components of SSA and AMUSE. In this context, the maximum Pearson coefficient of correlation between SSA_1 and $AMUSE_1$ (equation (6-16)) is used as the cost function to the define the final *K* value.

$$\underset{K \in \mathbb{Z}}{\operatorname{argmin}} P = \underset{K \in \mathbb{Z}}{\operatorname{argmin}} \frac{1}{M-1} \sum_{i=1}^{M} \frac{A_K(i) - \mu_{A_K}}{\sigma_{A_K}} \cdot \frac{B_K(i) - \mu_{B_K}}{\sigma_{B_K}} \tag{6-16}$$

where A_K and B_K denotes SSA_1 and $AMUSE_1$ components computed with a specific K value, μ and σ denotes the mean and standard deviation of each component.

The algorithm flow of the proposed SSA-AMUSE method is shown below:

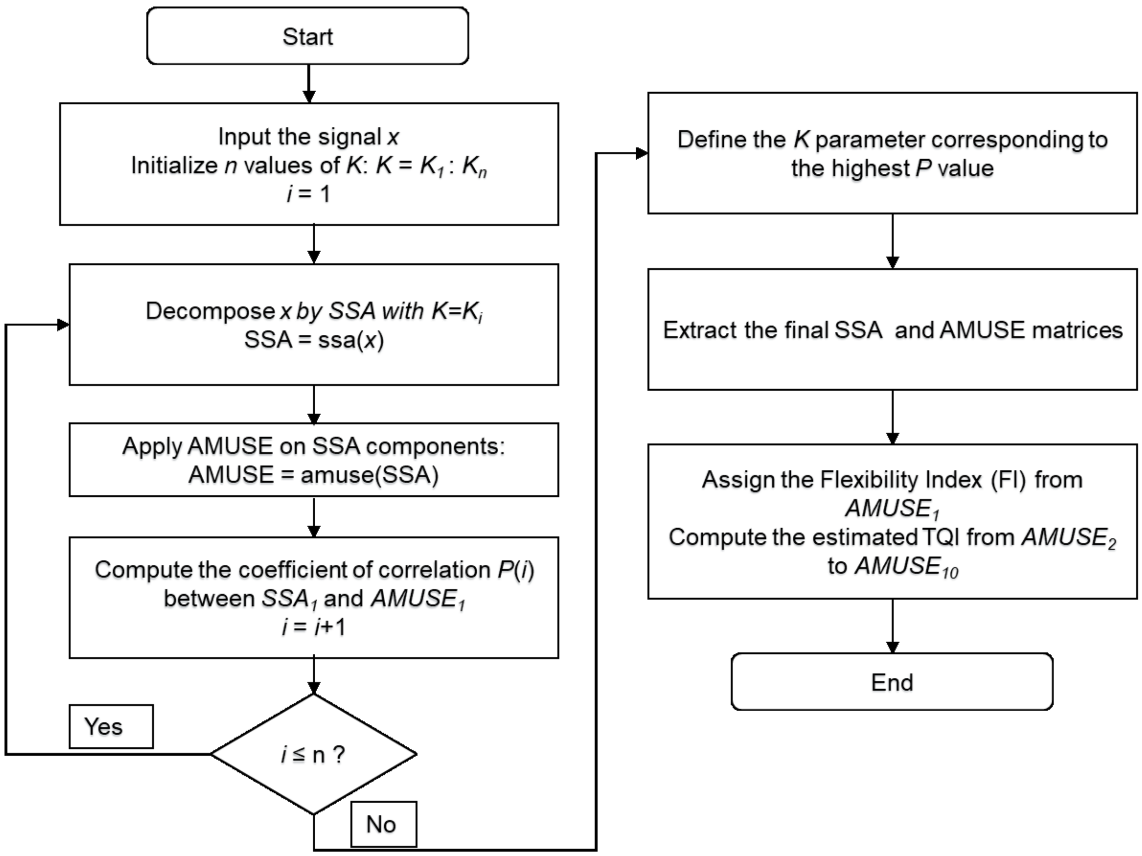

Figure 6-1. The flowchart for the proposed method

6.3. Application of the proposed method on field data

In this section, the proposed method is applied to analyze the field data. Y_{rel} and track geometry measurements recorded along over 200 km of Canadian track are analyzed in the current study.

6.3.1. Study site and measurement system

The schematic description of the study side is shown in Figure 6-2. Since the measurement system was operated together with the revenue locomotives, the wheel loads and weight of the adjacent cars were not available.

Figure 6-2. The study area

6.3.2. The continuous track stiffness measurement system

As mentioned previously, MRail system is used to measured vertical track deflections [195]. The system hardware and data acquisition are shown in Figure 6-3. Overall, the system provides noncontact measurements of the vertical track deflection using two laser lines and a camera to capture the laser projections on the rail surface. Deflections measured by the system are the relative distance of the railhead at 1.22 m from the nearest wheel before and after loading (i.e. Y_{rel}).

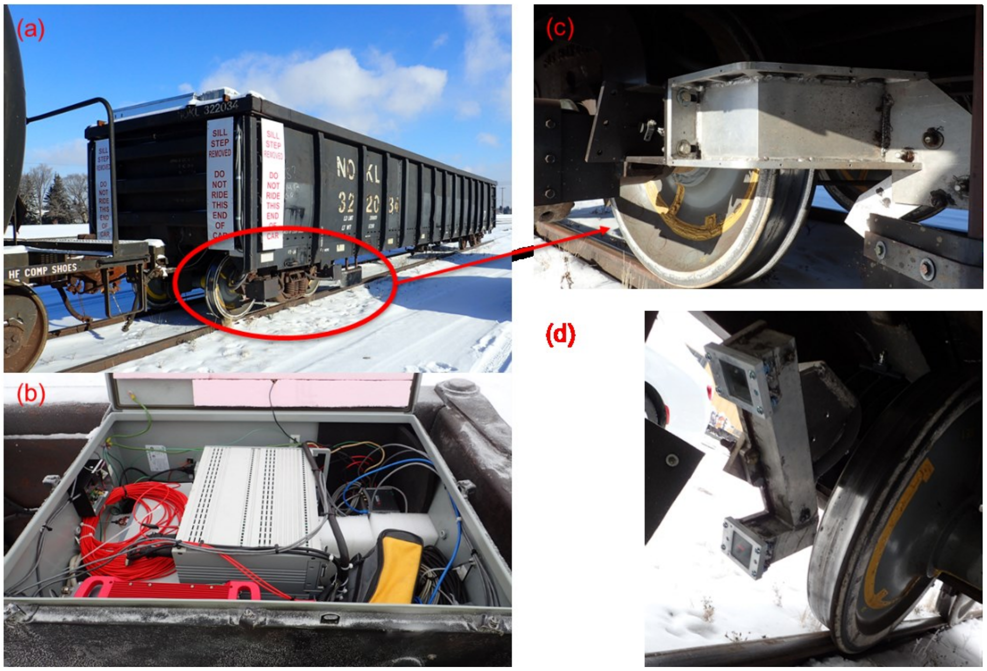

Figure 6-3. The MRail system: (a) the carrying car; (b) the acquisition uinit; (c) the mounting frame; (d) the laser unit

6.3.3. Preliminary analysis

The raw Y_{rel} recorded over the whole study site is shown in Figure 6-4(a). A preliminary analysis is first conduced to investigate the variations of the recorded data and to locate their extreme values for further investigations. A moving average (MA) of Y_{rel} over 1524 m (5000 ft) is shown in Figure 6-4(b). In addition, a simple control chart with the upper control limit (UCL) and lower control limit (LCL) being computed by one standard deviation of Y_{rel} MA is depicted in the same figure. As shown in Figure 6-4(b-c), the Y_{rel} values at Mile 49.4 and 101.4 are two of the outliers being detected. The two locations actually have deterioration that was observed during the operations of the railway line [202,203]. Figure 6-4(c) also shows other extreme values of Y_{rel} within the first 64.4 km of the study site. The common factor of these values is that they are mostly located at curves. This phenomenon will be further investigated in the subsequent sections.

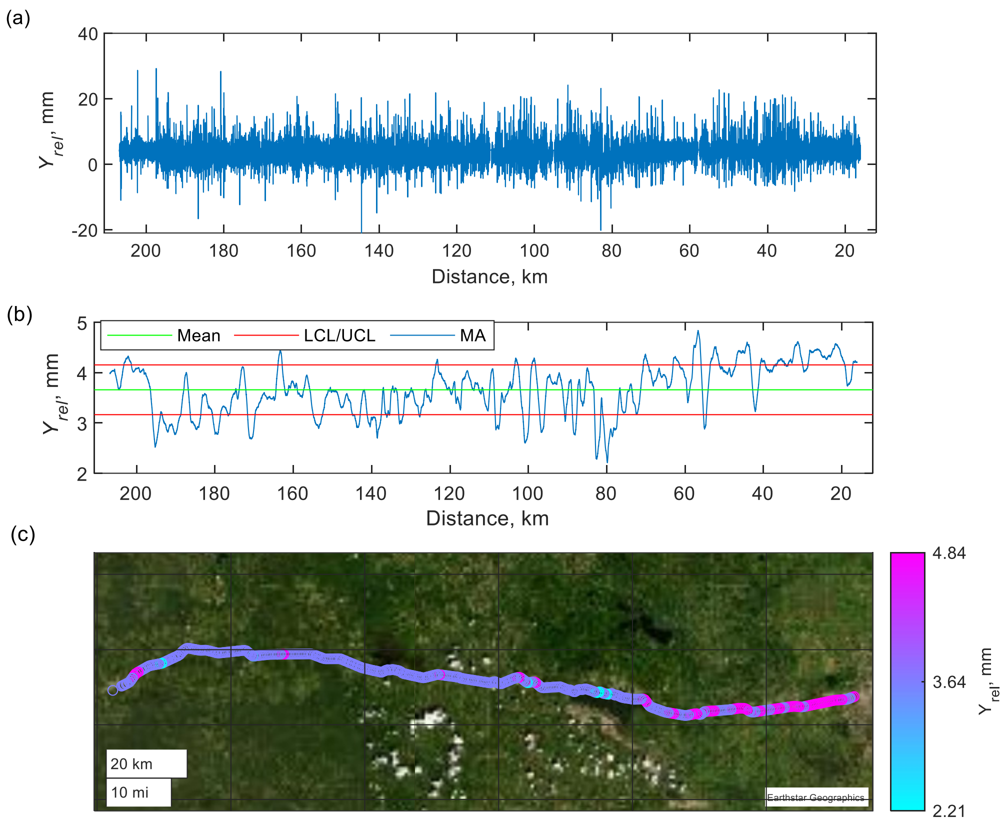

Figure 6-4. The variations of Y_{rel} along the railway line: (a) raw Y_{rel}; (b) 1524-m MA of Y_{rel} and its control chart; (c) the map of Y_{rel}'s extreme values along the railway line

An example of the raw Y_{rel} and track geometry measurements is given in Figure 6-5. As can be observed in the figure, the Y_{rel} data has a degree of similarity with the track vertical profile, especially at locations with high Y_{rel} magnitudes. However, the similarity cannot be quantified from the raw signals as further analysis is required to investigate their correlation.

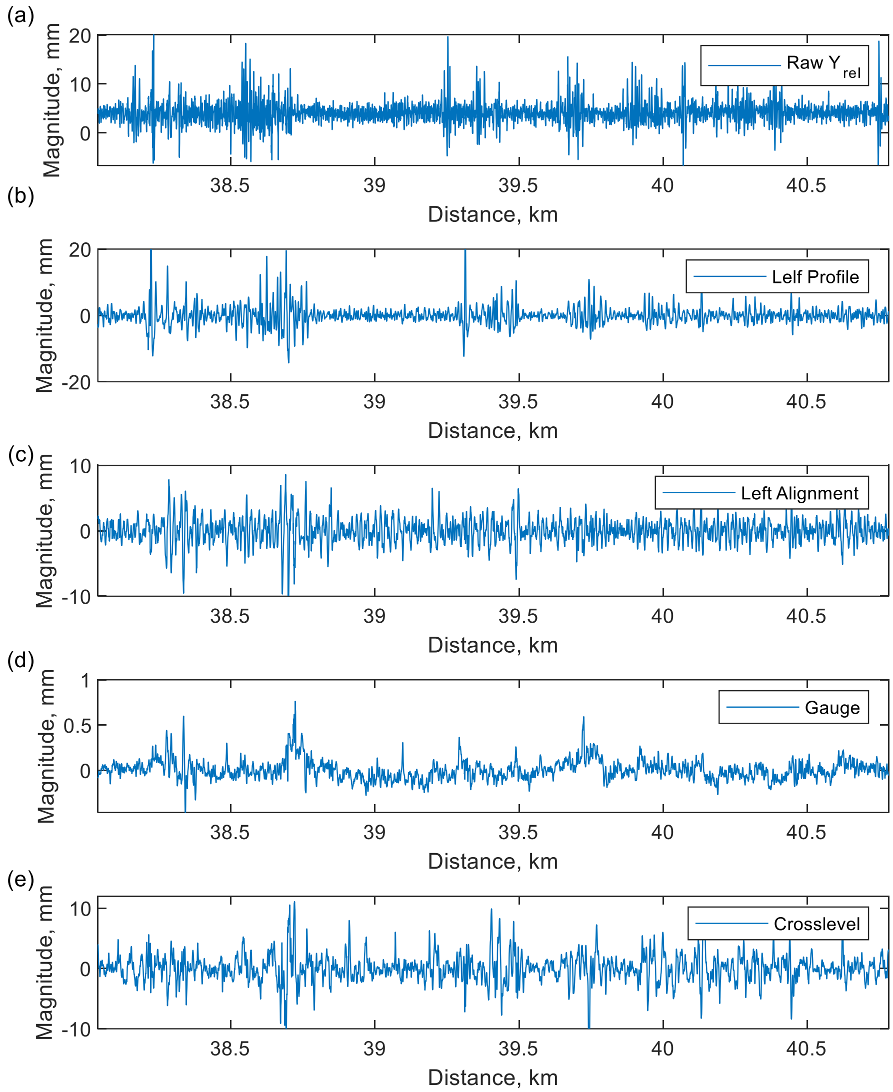

Figure 6-5. The measured data: (a) Y_{rel}; (b) Profile; (c) Alignment; (d) Guage; (e) Crosslevel

6.3.4. Analysis results

In order to show the effectiveness of the methodology, the Y_{rel} data and vertical track profile for a track segment including a railway bridge is first examined. From Figure 6-6, due to the presence a short span, a long span railway bridges connected by an approach, the high variations of track stiffness over this track segment can be clearly observed. In addition, Y_{rel} and vertical profile reflect well the variations of the track stiffness and geometry, especially at the railway bridges and grade crossings approximately occurring at the kilometer 68.8 and 71.0. The impact of track geometry (e.g. the unloaded track profiles in space) on Y_{rel} measurements were investigated in different studies [132,142,143]. For instance, Roghani et al. [113] conducted a correlation analysis between geometry defects and the filtered Y_{rel} measurements. It was found that highest frequency of defects in warp, crosslevel, and profile coincide with the large magnitudes of moving average filtered Y_{rel}. This finding agrees with the investigation about track stiffness measurement systems conducted by [134], where the authors confirmed that the total deflections measured by those systems included the unloaded track profiles, void deflections (e.g. under hanger sleeper), and contact deflection under loading.

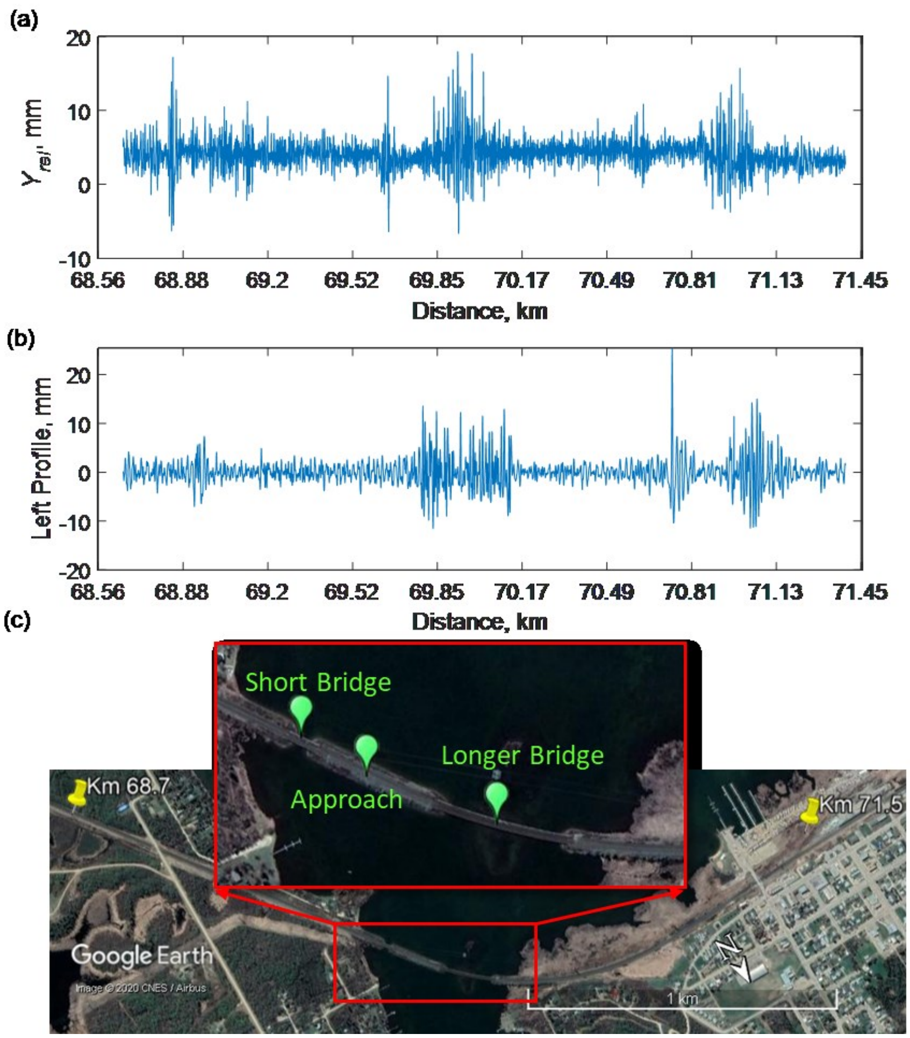

Figure 6-6. (a) The measured Y_{rel} ; (b) the track profile; (c) the track segment

First, different configurations of SSA are initiated and applied on the Y_{rel} data. the purpose is to show the sensitivity of SSA under different configurations. As mentioned previously, the most important parameter for SSA is the number of elementary components (K) resulting in the corresponding value of window length L. In this study different values of K are selected (i.e. $N/6$, $N/5$, …, $N/2$). The first SSA component of Y_{rel} with four different values of K is shown in Figure 6-7.

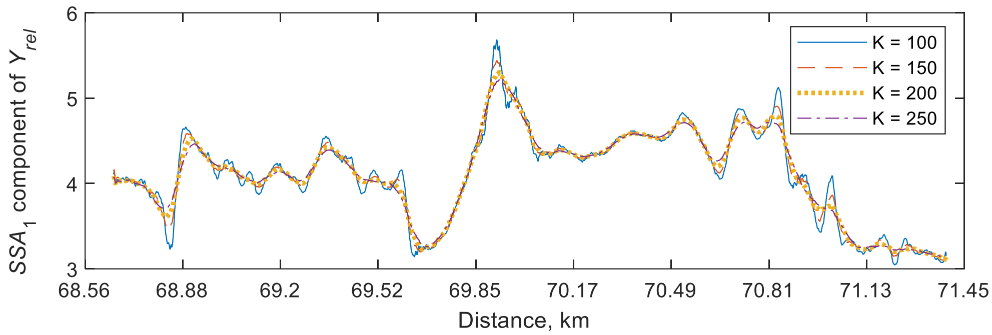

Figure 6-7. SSA_1 component under different K parameters

As shown in Figure 6-7, different values of K alter the first SSA component (i.e. SSA_1) in such a way that increasing K results in SSA_1 that has longer wavelength content. In this study, the SSA_1 component of Y_{rel} is considered a reflection of track modulus as it is essentially the trend of the signal. In fact, extracting the trend or long wavelength component in Y_{rel} by moving average filter has been widely applied in many related studies which showed that the moving average of Y_{rel} reflects really well the subgrade conditions (or track modulus variations) [141,143]. Herein, the trend is extracted by SSA instead of moving average filter. A comparison between the SSA_1 component and different moving averaged Y_{rel} is shown in Figure 6-8.

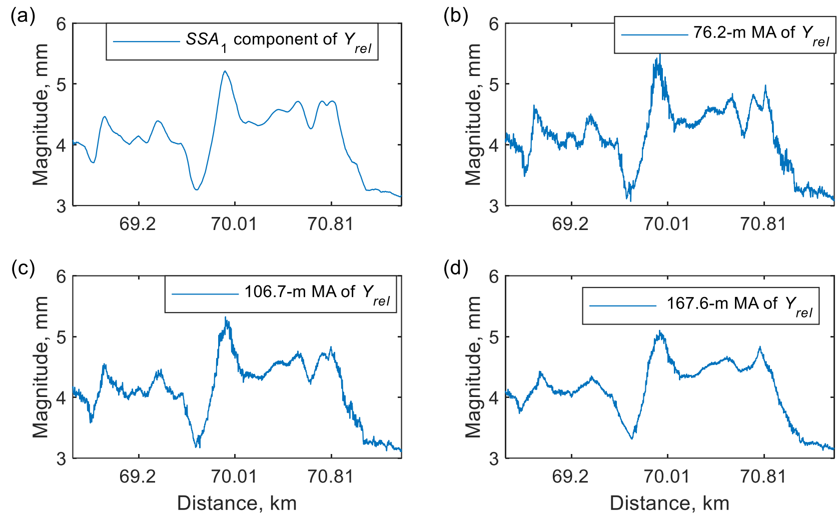

Figure 6-8. The processed Y_{rel}: (a) the 1st SSA component; (b) 76.2-m MA; (c) 106.7-m MA; (d) 167.6-m MA of Y_{rel}

As observed in Figure 6-8, the moving average of Y_{rel} (Figure 6-8(b-d)) is well comparable to the first SSA component (Figure 6-8(a)) as they follow similar patterns. However, the first SSA component is more efficient than the moving average of Y_{rel} as it effectively eliminates short wavelength content. It is worth noting that short wavelength (or high frequency) components in Y_{rel} data can also be further removed by using moving average with longer window length. However, increasing the window length of a moving average filter will also cause the filtered signal to lose local fluctuations. By comparison between Figure 6-8(a) and Figure 6-8(d), the local fluctuations still retain in the SSA_1 signal whereas they are hardly observed in Figure 6-8(d) (167.6-m MA of Y_{rel}).

The question of interest is defining the value of SSA parameter, K in an automatic manner. The application of AMUSE is proposed to define the K value of SSA and further separate the SSA components to retrieve additional information about the track geometry.

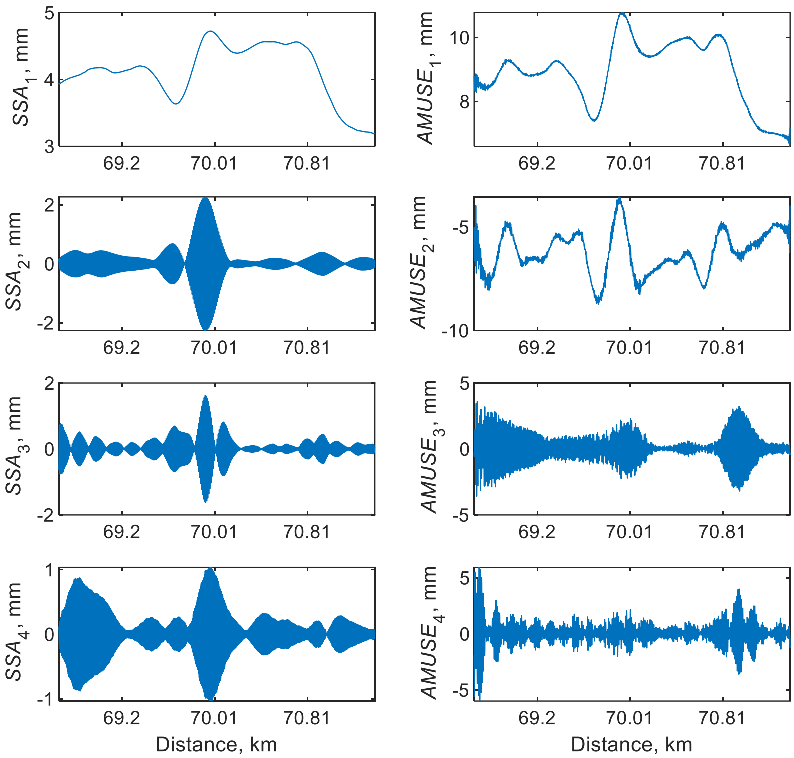

Figure 6-9. Comparison between the first four SSA and AMUSE components

Figure 6-9 demonstrates an example of the first four SSA and AMUSE components. As can be seen, SSA components are transformed into the corresponding AMUSE components after applying AMUSE. In this study, as the trend of the signal represented by SSA_1 should be reserved at the end of the analysis to indicate the variation of track stiffness, the constraint when applying AMUSE is that the first SSA component should be maintained after the transformation. As indicated in the flowchart (Figure 6-1), by varying the parameter K and examining the coefficient of correlation (P) between SSA_1 and $AMUSE_1$, the final K value is the one that produces the highest P value. The variation of the correlation between SSA_1 and $AMUSE_1$ under different values of K is shown in Figure 6-10. As can be seen, when K varies from 150 to 450, $AMUSE_1$ is closest to SSA_1. In this case, 300 is chosen as the final value of K. Different data segments were also checked and it is shown that $K = 300$ is a suitable value for the current application.

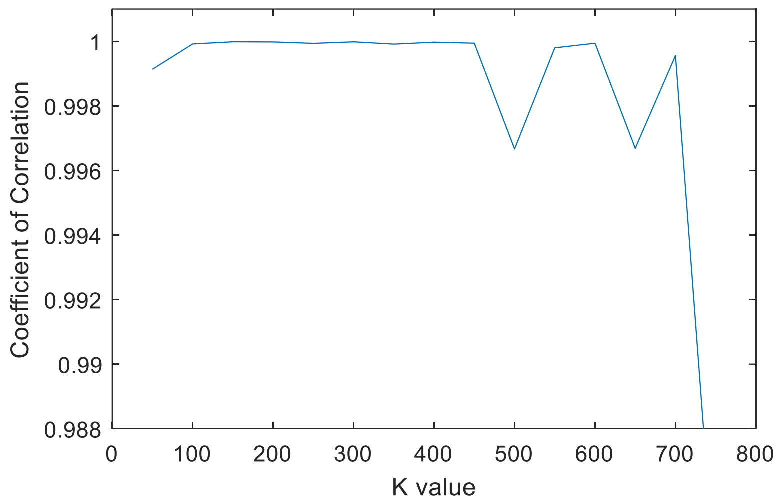

Figure 6-10. The correlation between SSA_1 and $AMUSE_1$

With the current configuration of SSA (K = 300) and AMUSE (τ = 1), the first few components of AMUSE are utilized to represent the track modulus and track geometry information. Regarding the application of SSA, it simply produces the trend, seasonality, and harmonics in the signal. On the other hand, AMUSE further separates the SSA components and rearranges the components in a way that each component contains separated informative signals. For instance, with the current configuration of SSA (K = 300) and AMUSE (τ = 1), the raw Y_{rel} in Figure 6-6 is first decomposed into 300 components. Only the first 20 components are kept for further processing with AMUSE as they account for more than 90% of the total energy of the original Y_{rel}. Finally, the first AMUSE component is used as the flexibility index (FI) to indicate the track stiffness variations, whereas the second separated signal (coming from the linear combination of the 2nd to the 10th AMUSE components) is considered as the indicator of the vertical profile signal. The results are depicted in Figure 6-11, where the computed FI clearly shows the location with a high variation of track stiffness. Comparing Figure 6-6(c) and Figure 6-11(a), the lowest value of FI occurs at km 69.7 is due to the short railway bridge. It is followed by an increase in FI due to the soft approach, and then a decrease due to the second railway bridge.

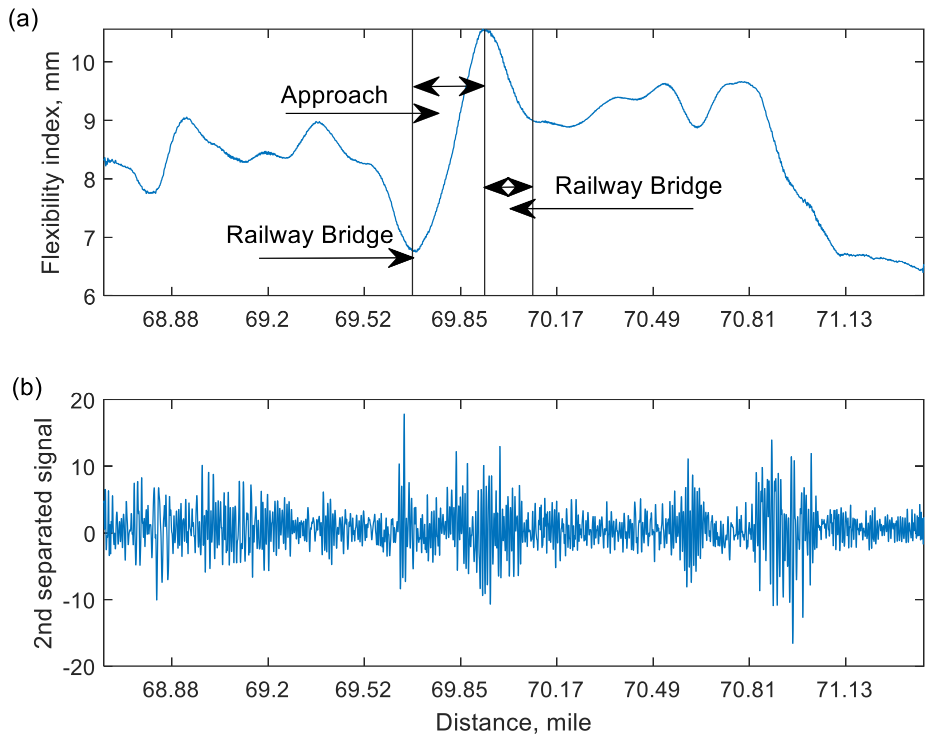

Figure 6-11. The final signals extracted from Y_{rel}: (a) Flexibility index; (b) the 2^{nd} separated

The correlation between the second separated signal and the vertical profile data is shown by the strong correlation between the track quality index (TQI) computed by the two signals. In this study, the TQI is computed by calculating the standard deviation within 76 m (250 ft) length of the track. the actual TQI of the profile (TQI_{Pro}) is computed directly from the track geometry measurements whereas the estimated track quality index (TQI_{est}) is computed from the 2^{nd} separated signal of Y_{rel} data. As can be seen in Figure 6-12, the variation of TQI_{Pro} is well captured by TQI_{est}, especially at the locations with high variations of the track geometry. In this case, the coefficient of correlation between the two TQIs is 0.73.

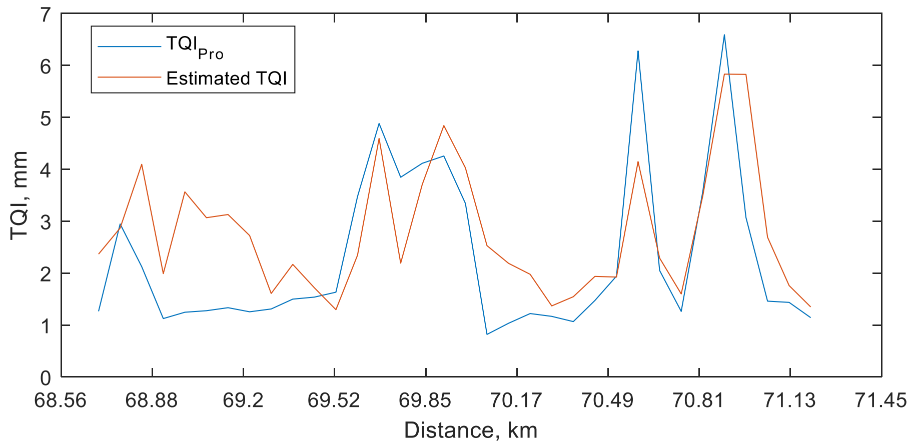

Figure 6-12. Comparison between the actual TQI and the TQI_{est}

By applying the same procedure, the values of FI and the TQI_{est} are computed over long distances. As can be seen in Figure 6-13(a), sudden changes in the FI are corresponding to the road crossings, where the track modulus increases significantly. It is also seen in Figure 6-13(b) that the TQI_{est} and its variations well capture the actual TQI_{Pro} of the track profile as the coefficient of correlation between the two parameters computed over 9 km of the track is 0.75. A good match between the current estimated TQI_{est} and the actual TQI_{Pro} especially those with high magnitudes is another advantage of the proposed method over moving average filter approach [113]. From Figure 6-13(c), the TQI is estimated by calculating the standard deviation of the measured Y_{rel} after subtracting from its filtered signal (using 122-m MA filter). As can be seen, the actual values of TQI_{Pro} are underestimated by this method. Quantitatively, the Mahalanobis distance between the excessive values of TQI in Figure 6-13 estimated by the proposed method and the actual values is 7.46 whereas it is 36.60 when TQI was estimated by the moving average method [113]. This means that the TQI_{Pro} values estimated by the current method are closer and more correlated to the actual values. Moreover, it is worth noting that the estimated TQI_{est} is solely computed from Y_{rel} data without any priori knowledge about the track geometry measurements.

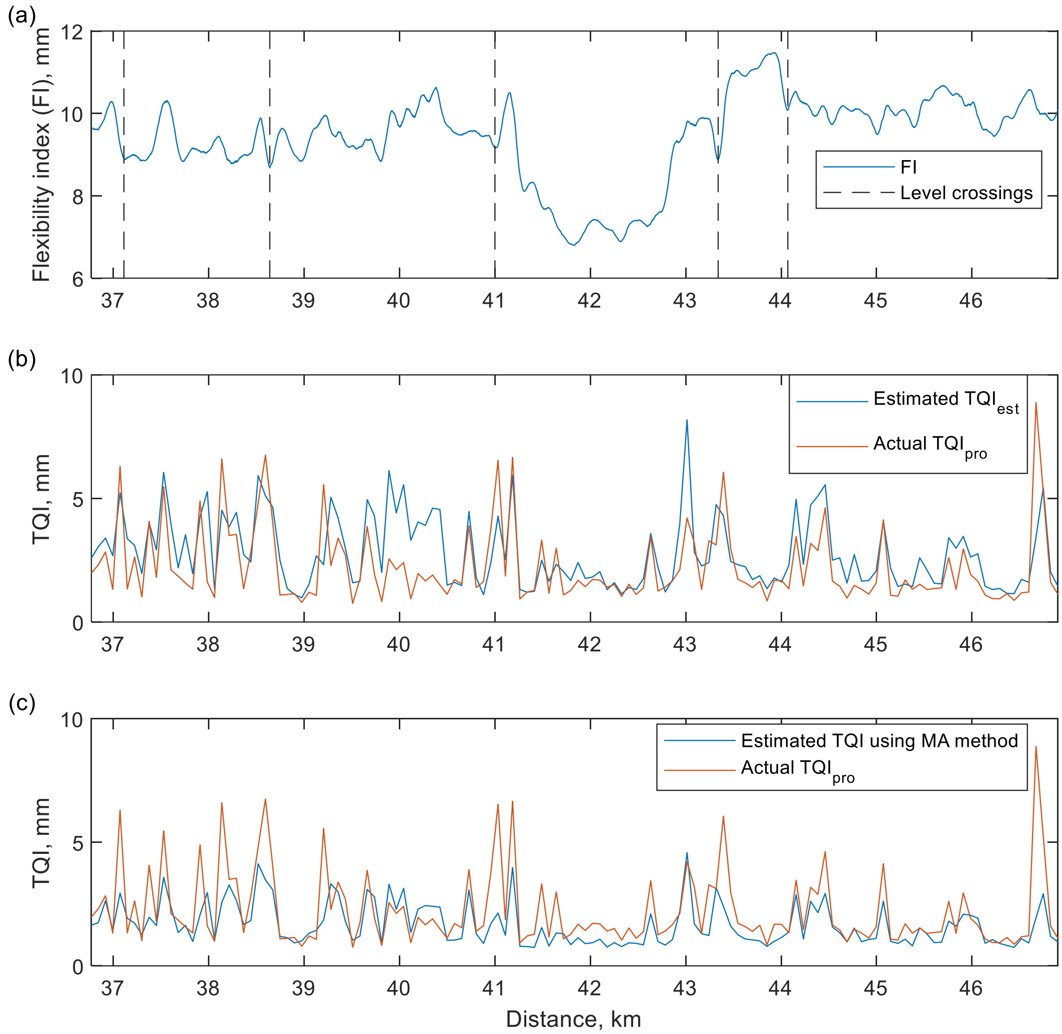
(a)
Flexibility index (FI), mm
FI
Level crossings
(b)
TQI, mm
Estimated TQI_{est}
Actual TQI_{pro}
(c)
TQI, mm
Estimated TQI using MA method
Actual TQI_{pro}
Distance, km

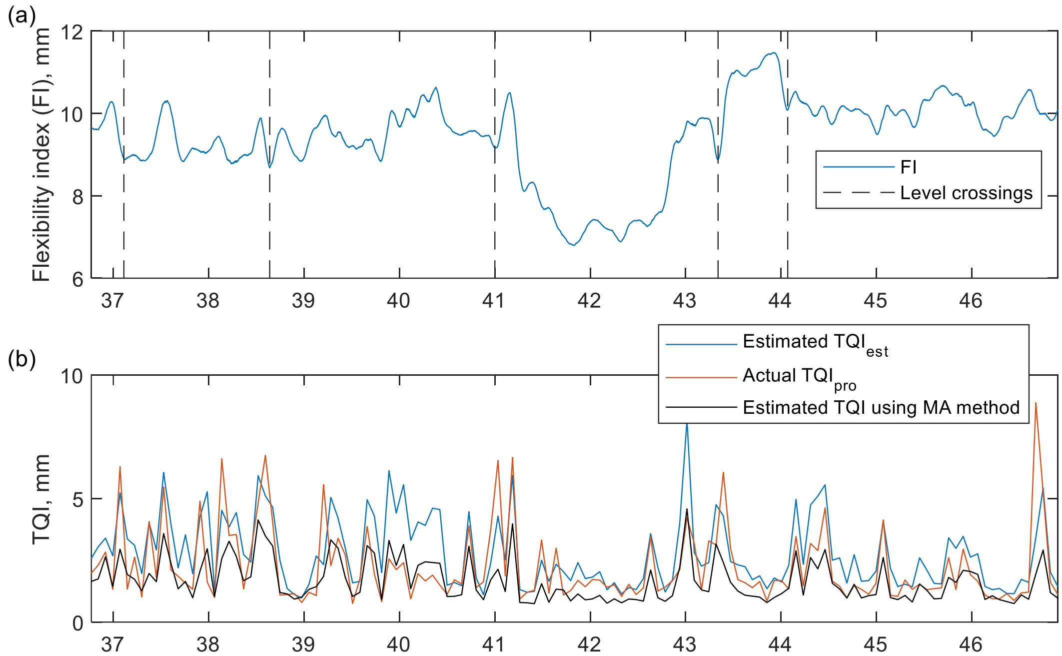

Figure 6-13. (a) The FI and (b) TQI$_{est}$ computed by the proposed method

Importantly, there is a track segment within the 41.84th km in Figure 6-13(a) where there is a substantial decrease in the FI although the track profile quality in this segment is higher than other locations in Figure 6-13(b). This behaviour in the processed Y_{rel} signal (e.g. the FI signal) can only be explained by further decomposing the Y_{rel} signal using the proposed method. In this case, K = 7000 is chosen to apply SSA on Y_{rel} signal which results in a more global trend in SSA_1 (the first SSA component). The comparison between the track plan, the corresponding superelevation and the resulting SSA_1 are shown in Figure 6-14. It is clear that the SSA_1 (which is computed from the Y_{rel} measurements) is directly related to the superelevation of the track (Figure 6-14(b)) with the coefficient of correlation being 0.85. The effect is due to the fact that MRail system uses images of the laser lines projected on the rail surface to output Y_{rel} signals. When the difference in the height of two rails (superelevation) is substantial, especially at curves, the angle between the camera and rail surface changes accordingly. Therefore, the image of the laser lines on the rail surface will be different which results in the change in Y_{rel} values. The effect of superelevation can be further confirmed by the asymmetric correlation between the SSA_1 components of Y_{rel} recorded on the left and right rails. This asymmetric correlation is due to the instance when the left rail is higher than the right rail and vice versa. This effect can be minimized by taking the average of SSA_1 computed from the left and right Y_{rel} as shown in Figure 6-14(c).

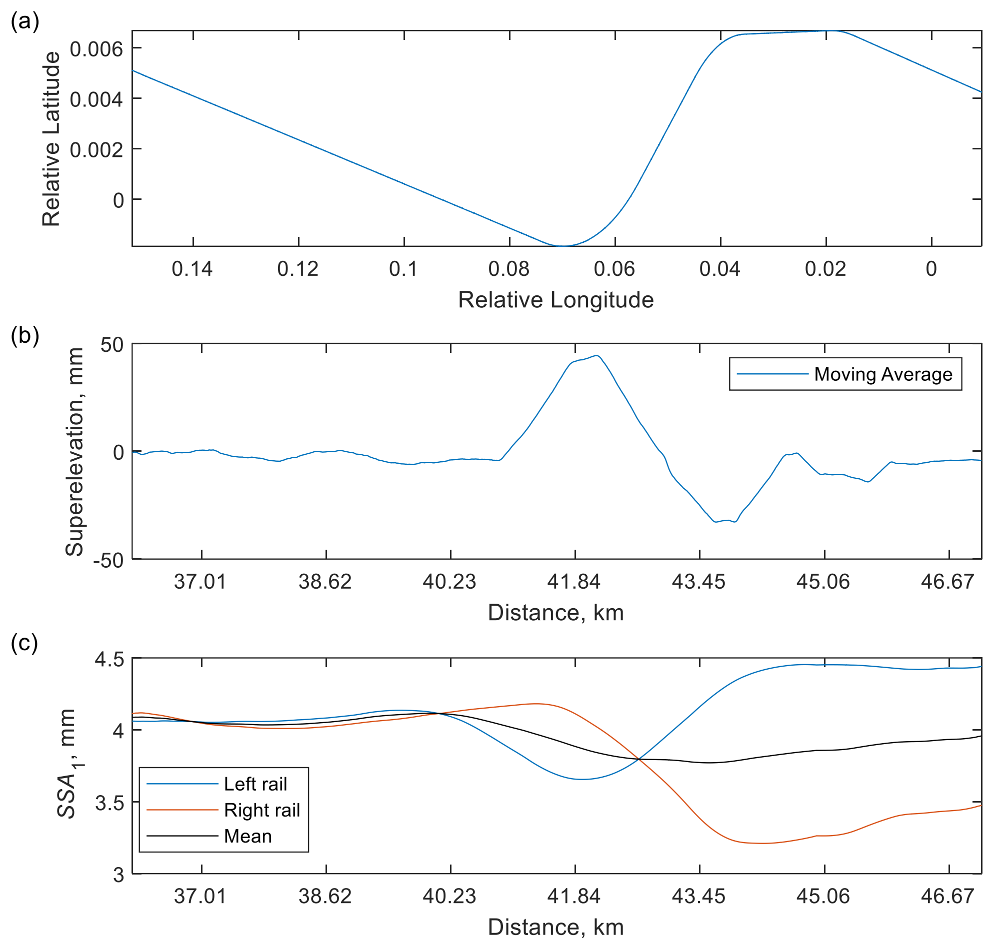

Figure 6-14. Comparisons between: (a) the track plan; (b) superelevation; and (c) the computed SSA_1

The method's effectiveness in locating the subgrade stiffness variations is also demonstrated via a tangent track segment in Figure 6-15. The segment is laid on a peat mire formation (a big bog can be observed in Figure 6-15(a)) between the 162.5th and 164th km. For this reason, the segment has undergone deteriorations (e.g. skewed, broken ties, rail seat abrasion failure) due to the strong movement of the rail-track structure [203]. Note that the average of the FI signals on the left and right rail is taken as the final flexibility index (FI_{mean}) to reduce the effect of superelevataion. As shown in Figure 6-15(b), the increase in the FIs between the 162.5th and 164th km indicates exactly the location of the track that has reduced track modulus. Apparently, the variations of superelevation over this tangent segment are minimal which explains the symmetric correlation between the FI values on the left and right rails. In addition, Figure 6-15(c) shows that there is a strong correlation between the TQI_{est} and TQI_{Pro} with the coefficient of correlation being 0.72. Therefore, the computed TQI_{est} can be considered as an indicator of the track profile variations.

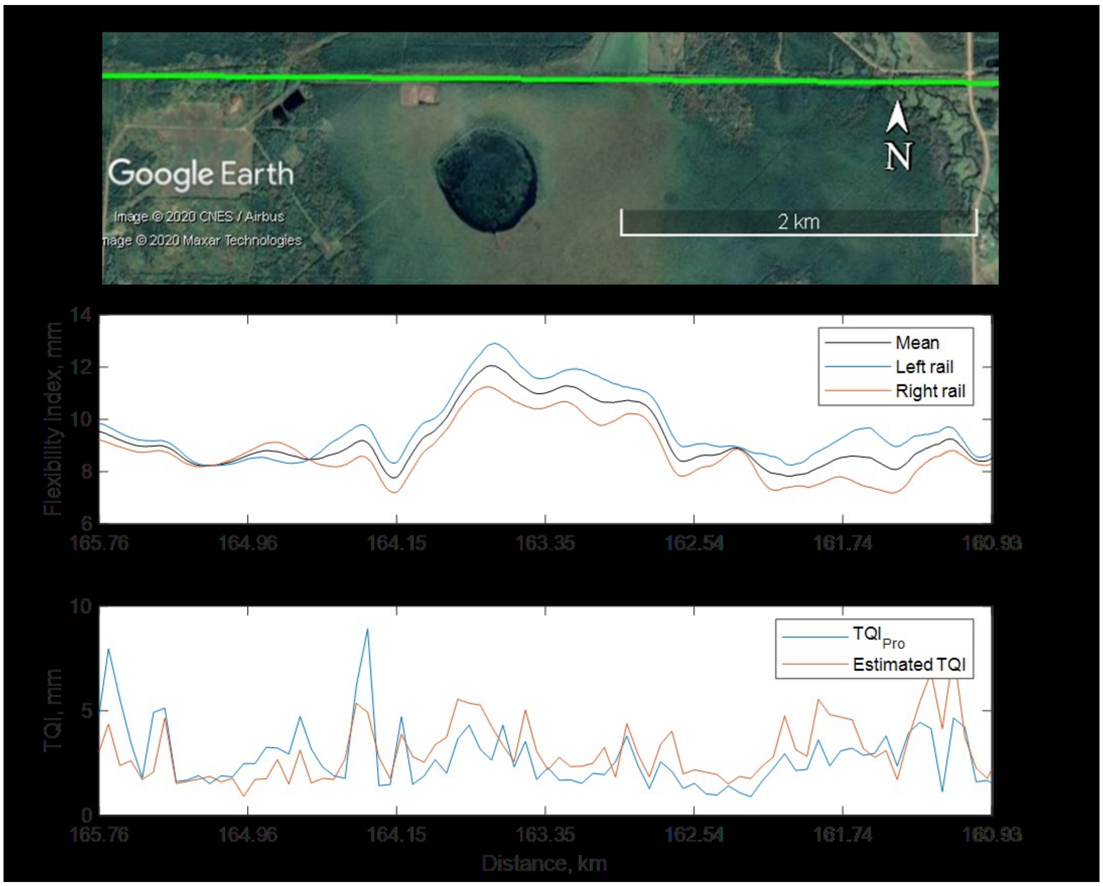

Figure 6-15. The results over a tangent track: (a) the track location; (b) FI's variations; (c) the estimated TQI_{est}

6.4. Conclusions

In this case, a new single channel blind source separation methodology is proposed to evaluate the track support conditions and track geometry of a Canadian railway line using continuous vertical track deflection measurements. This study also reveals more insight into the factors that affect the readings of a continuous track stiffness measurement system (MRail in particular). By combining singular spectrum analysis and algorithm for multiple unknown signals extraction, the recorded vertical track deflection data is separated into two independent signals which are subsequently used to build a track flexibility index (FI) and an estimated track quality index (TQI_{est}). The results show that the FI can provide useful information about the track modulus and its variations (e.g. level crossings, soft foundation due to peat meres), whereas TQI_{est} effectively reflects the vertical profile variations. On the other hand, the analysis in the current study shows that vertical profile is not the only primary factor that affects the readings of the MRail system. In this case, the measurements are substantially affected by the track superelevation, especially at curved tracks. This study also suggests that MRail measurements should be taken at both left and right rails to output the average values which are less sensitive to the variations of superelevation.

Chapter 7: Conclusions and Recommendations for Future Research

7.1. Summary and conclusions

In this study, new methodologies for track stiffness and rail bending moment evaluations considering the effects of track geometry using vertical track deflection (VTD) measurements were developed and validated. As track conditions at the surface level and subgrade stiffness are successfully quantified from a single type of measurements, the developed methods are expected to facilitate cost-effective maintenance strategies and contribute to the safety and reliability of railway networks. The study focused on the MRail system, a continuous track stiffness measurement system that collects the relative VTD (which is Y_{rel}) between the line connecting wheel/rail contact points and the rail surface, at a distance 1.22 m from the nearest wheel. The current study also provided a detailed investigation of track geometry effects on the readings of the MRail system. Although the proposed methodologies in this thesis require the measured Y_{rel} data as the primary input, the application of the methodologies on other types of continuous track stiffness measurement data would be still valid provided that the process of interpreting the VTD should be slightly modified, depending on the type of measurement systems. The following paragraphs present the summary and conclusion of the investigations of each objective of this research as presented in Chapters 3 to 6.

The capability of using Y_{rel} measurements for evaluating the track modulus, an important factor representing the track performance, was investigated in detail in Chapter 3. A series of finite element models (FEMs) that were previously developed to simulate a rail segment on discrete spring supports with varying stiffness were employed to estimate the track modulus variations from Y_{rel} over different track section lengths. Two methodologies based on Artificial neural networks (ANNs) together with statistical and frequency analysis were proposed to estimate the track modulus average and standard deviation from the corresponding Y_{rel}. The results showed that the variations of track modulus were effectively estimated regardless of the effects of reducing the length of the track section. The ANNs in the study were trained with the data corresponding to a specific rail size and loading condition. Therefore, re-training ANNs are required for other loads and rail sizes.

Information about the maximum bending moments is valuable for calculating maximum tensile and compressive stress in rails. For this reason, the capability to MRail system for evaluating the rail bending moments was investigated in Chapter 4. The analysis of the simulated Y_{rel} data and the bending moments showed that there is a strong correlation between the extreme values of Y_{rel} and those of the bending moments. The values of the maximum positive and negative bending moments depend on different factors including but not limited to the loading conditions and the track foundation. Thus, the simulated Y_{rel} data was used to estimate the extreme values of the bending moments. In this context, radial basis function neural networks and wavelet multiresolution analysis were employed to develop two frameworks for estimating the local extreme values of positive and negative moments. The results from the proposed methodologies further confirmed the potential of using data from a continuous track stiffness measurement system (e.g. MRail) for structural health monitoring of rails over large railway networks.

As the effectiveness of using a continuous track stiffness measurement system for track performance monitoring was demonstrated Chapter 3 and Chapter 4, Chapter 5 investigated the effects of track geometry variations on the Y_{rel} measurements. Dynamic models were developed to simulate the stochastic properties of track modulus and longitudinal track geometry variations. The main purpose was to investigate the impacts of track geometry on the Y_{rel} measurements and to verify the ability of using Y_{rel} data (which contains mixed information due to the presence of track geometry) for identifying the variation of track modulus. A new methodology was proposed to solve the single channel blind source separation problem by employing singular spectrum analysis (SSA) and the algorithm for multiple unknown signals extraction (AMUSE). Prior to applying the method on the simulated Y_{rel} measurements, its performance was validated by recovering the original separated synthetic signals from a single channel observation. The methodology was subsequently used to separate the track geometry and track modulus information from Y_{rel}, a single channel datatype. Contradict to the related studies in the literature, the results in the study showed that the effects of track geometry on Y_{rel} measurements were significant and they may mask the information of track modulus in the Y_{rel} data. The extracted track features showed that information about both track modulus and track geometry was obtained simultaneously using the proposed method.

Investigations of the field measurements of track geometry and Y_{rel} (recorded by MRail system) were comprehensively conducted to verify the effectiveness of the proposed study. The preliminary analysis of the data recorded from over 200 km of a track subdivision confirmed the dominance of the track profile on the Y_{rel} data. An improved method was developed to reveal the flexibility index for track performance and track quality index for track geometry evaluations from Y_{rel} data only. The field investigation also discovered the great impacts of superelevation on the MRail system. This finding could be a significant implication in improving the effectiveness of MRail system as well as other continuous track stiffness measurement systems where track deflections are inferred from other raw signals such as images or accelerations.

7.2. Recommendations for future research

The proposed methodologies in this research require further developments to facilitate an effective structural health monitoring framework for rail track structures. The estimations of rail bending moments using Y_{rel} data should be validated with field data. The task can be done by collecting the strain response of a rail under train passages and the Y_{rel} data collected by MRail system. Collecting rail strains over long distances is possible due to the implementation of fiber optic sensing that has been widely used in railway monitoring [18,164]. Having the Y_{rel} data and the corresponding strain allows a valid verification of the proposed method for estimating rail bending moments from Y_{rel}. The estimation results can be further compared with the degradation history of the rails at a specific subdivision for a better understanding of the impact of excessive bending in rails on rail defects. This rigorous study could contribute to: 1 – establishing allowable rail deflections that result in acceptable bending stresses; 2 – developing an outlier detection tool to facilitate effective rail inspection strategies.

This research also indicated that superelevation can cause systematic errors in the readings of MRail system. This effect implies that the motion of the car carrying the MRail system potentially affects the measurements especially because the MRail system employs an image-based technique to output track deflections. Any rotation in the measurement system may distort the recorded images considerably and may result in inaccurate Y_{rel} measurements. Therefore, a detailed analysis of the system configuration should be conducted to study the impact of vehicle motions on Y_{rel}, especially rotations in the vertical and transverse planes. A study may be conducted to implement an inertial measurement unit (IMU) on the car hosting the MRail system. The recorded vehicle motions would facilitate a better understanding about the measured Y_{rel} data.

Effects of environmental and operational conditions on VTD measurements should be considered extensively. It has been shown that there was a considerable decrease in rail bending stress and deflections when ballast was frozen. In low temperature, rails are subject to high tensile thermal stresses, and are more susceptible to fracture. Therefore, a comprehensive assessment of rail bending stresses and track stiffness from VTD measurements must include a detailed study of simultaneous effects of environmental and operational factors on the measured data.

Comprehensive combinations of continuous track stiffness measurement techniques with other track performance monitoring methods such as ground penetration radar (GPR) for a better rail track structural health monitoring scheme. Both GPR and track stiffness measurement systems have been widely used in track performance evaluations [78,85,204,205]. However, they were mainly deployed individually or in a parallel manner, which means data from each system was interpreted separately. It must be emphasized that processing GPR signals can only be handled by well-trained personnel as engineering judgments must be made to convert GPR scans into the sublayer thickness, whereas interpretations of the MRail data itself do not guarantee accurate evaluations of track stiffness. Therefore, detailed investigations about the relationship between the MRail data and other data such as GPR should be conducted so that the analysis of each dataset can supplement each other, and issues associated with the track performance can be clearly explained.

References

[1] Transportation Safety Board of Canada, Rail, *https://www.tsb.gc.ca/eng/rail/index.html* (Accessed November 7, 2019).

[2] X. Liu, M.R. Saat, C.P.L. Barkan, Analysis of Causes of Major Train Derailment and Their Effect on Accident Rates. *Transportation Research Record* 2289 (2012) 154-163. doi:10.3141/2289-20.

[3] X. Liu, Statistical Causal Analysis of Freight-Train Derailments in the United States. *Journal of Transportation Engineering, Part A: Systems* 143 (2017) 04016007. doi:10.1061/JTEPBS.0000014.

[4] Federal Railroad Administration (FRA), Office of Safety Analysis, Train Accidents by Cause (2016), *https://safetydata.fra.dot.gov/OfficeofSafety/publicsite/Query/inccaus.aspx* (Accessed July 30, 2018).

[5] Railway Occurrences 2017 - Statistical Summary - Transportation Safety Board of Canada, *https://www.bst-tsb.gc.ca/eng/stats/rail/2017/sser-ssro-2017.html* (Accessed Jul 30, 2018).

[6] E. Berggren, M. Hosseingholian, G. Saussine, M. Rodriguez, V. Cuellar, H. Vialletel, Methods of Track Stiffness Measurements. *INNOTRACK*2011.

[7] D. Li, R. Thompson, P. Marquez, S. Kalay, Development and Implementation of a Continuous Vertical Track-Support Testing Technique. *Transportation Research Record* (2004) 68-73.

[8] S. Lu, Real-Time Vertical Track Deflection Measurement System, PhD Dissertation, University of Nebraska Lincoln (UNL), Lincoln, Nebraska, 2008.

[9] W. Wangqing, Geming Z, Kaiming Z, Lin L, Development of inspection car for measuring railway track elasticity, *Proceedings from 6th International Heavy Haul Conference, Cape Town,* 1997.

[10] D. F. Cannon, K.O. Edel, S.L. Grassie, K. Sawley, Rail defects: an overview. *Fatigue & Fracture of Engineering Materials & Structures* 26 (2003) 865-886. doi:10.1046/j.1460-2695.2003.00693.x.

[11] W. W. Hay, *Railroad Engineering*, John Wiley & Sons; 2nd ed, 1982.

[12] U. Zerbst, M. Schödel, R. Heyder, Damage tolerance investigations on rails. *Engineering Fracture Mechanics* 76 (2009) 2637-2653. doi:10.1016/j.engfracmech.2008.04.001.

[13] U. Zerbst, R. Lundén, K.-. Edel, R.A. Smith, Introduction to the damage tolerance behaviour of railway rails – a review. *Engineering Fracture Mechanics* 76 (2009) 2563-2601. doi://doi.org/10.1016/j.engfracmech.2009.09.003.

[14] C. Esveld, *Modern Railway Track*, MRT Productions, Duisburg, West Germany, 1989.

[15] J. Seo, S. Kwon, H. Jun, D. Lee, Numerical stress analysis and rolling contact fatigue of White Etching Layer on rail steel. *International Journal of Fatigue* 33 (2011) 203-211. doi://doi.org/10.1016/j.ijfatigue.2010.08.007.

[16] T. Deshimaru, H. Kataoka, N. Abe, Estimation of Service Life of Aged Continuous Welded Rail. *Quarterly Report of RTRI* 47 (2006) 211-215. doi:10.2219/rtriqr.47.211.

[17] H. Yoon, K. Song, J. Kim, D. Kim, Longitudinal strain monitoring of rail using a distributed fiber sensor based on Brillouin optical correlation domain analysis. *NDT & E International* 44 (2011) 637-644. doi://doi.org/10.1016/j.ndteint.2011.07.004.

[18] L. N. Wheeler, W.A. Take, N.A. Hoult, H. Le, Use of fiber optic sensing to measure distributed rail strains and determine rail seat forces under a moving train. *Canadian Geotechnical Journal* (2018) 1-13. doi:10.1139/cgj-2017-0163.

[19] C. Greisen, S. Lu, H. Duan, S. Farritor, R. Arnold, B. GeMeiner, D. Clark, T. Toth, K. Hicks, T. Sussmann, M. Fateh, G. Carr, Estimation of rail bending stress from real-time vertical track deflection measurement. *Proceedings of the ASME/IEEE Joint Rail Conference 2009, JRC2009* (2009) 175-182. doi:10.1115/JRC2009-63050.

[20] G. B. Eric, A. Nissen, S.P. Björn, Track deflection and stiffness measurements from a track recording car. *Proceedings of the Institution of Mechanical Engineers, Part F: Journal of Rail and Rapid Transit* 228 (2014) 570-580. doi:10.1177/0954409714529267.

[21] S. Farritor, M. Fateh, *Measurement of Vertical Track Deflection from a Moving Rail Car (no. DOT/FRA/ORD-13/08)*, United States. Federal Railroad Administration. Office of Research and Development, 2013.

[22] S. F. Nafari, M. Gül, M. Hendry T., O. Duane, R.J.J. Cheng, Operational Vertical Bending Stresses in Rail: Real-Life Case Study. *Journal of Transportation Engineering, Part A: Systems* 144 (2018) 05017012. doi:10.1061/JTEPBS.0000116.

[23] C. Norman, S. Farritor, R. Arnold, S. Elias, M. Fateh, M. El-Sibaie, *Design of a System to Measure Track Modulus from a Moving Railcar*, US Department of Transportation, Federal Railroad Administration, Office of Research and Development, 2006.

[24] R. Alireza, M. Renato, M.T. Hendry, Quantifying the Effectiveness of Methods Used to Improve Railway Track Performance over Soft Subgrades: Methodology and Case Study. *Journal of Transportation Engineering, Part A: Systems* 143 (2017) 04017043. doi:10.1061/JTEPBS.0000071.

[25] S. F. Nafari, M. Gül, M.T. Hendry, R.J. Cheng, Estimation of vertical bending stress in rails using train-mounted vertical track deflection measurement systems. *Proceedings of the Institution of Mechanical Engineers, Part F: Journal of Rail and Rapid Transit* (2018) 0954409717738444. doi:10.1177/0954409717738444.

[26] M. X. D. Li, E.G. Berggren, A study of the effect of global track stiffness and its variations on track performance: simulation and measurement. *Proceedings of the Institution of Mechanical Engineers, Part F (Journal of Rail and Rapid Transit)* 224 (2010) 375-82. doi:10.1243/09544097JRRT361.

[27] A. D. Kerr, *Fundamentals of Railway Track Engineering*, Simmons-Boardman Books Inc., 2003.

[28] AREMA, *Manual for Railway Engineering*, The American Railway Engineering and Maintenance-of-Way Association, 2020.

[29] G. P. Raymond, Design for Railroad Ballast and Subgrade Support. *ASCE J Geotech Eng Div* 104 (1978) 45-60.

[30] E. T. Selig, J.M. Waters, *Track Geotechnology and Substructure Management*, Thomas Telford Publishing, 1994.

[31] M. Kerr, Rail Defects Handbook. *NSW Transport RailCorp* (2019).

[32] R. A. Mayville, P.D. Hilton, Fracture mechanics analysis of a rail-end bolt hole crack. *Theoretical and Applied Fracture Mechanics* 1 (1984) 51-60. doi:*https://doi.org/10.1016/0167-8442(84)90020-X*.

[33] U. Zerbst, K. Mädler, H. Hintze, Fracture mechanics in railway applications—an overview. *Engineering Fracture Mechanics* 72 (2005) 163-194. doi://doi.org/10.1016/j.engfracmech.2003.11.010.

[34] D. F. Cannon, K.O. Edel, S.L. Grassie, K. Sawley, Rail defects: an overview. *Fatigue & Fracture of Engineering Materials & Structures* 26 (2003) 865-886. doi:10.1046/j.1460-2695.2003.00693.x.

[35] T. G. Johns, K.B. Davies, D.P. McConnell, Introduction to stresses in rails: stresses in midrail regions. *Transportation Research Record* (1978) 10-19.

[36] S. Sroba, Kalousek, E. Magel, P. Sroba, K. Sawley, J. Kalousek, *Control of Rolling Contact Fatigue of Rails*, Centre for Surface Transportation Technology, National Research Council, Canada, 2005.

[37] O. Orringer, Y.H. Tang, J.E. Gordon, D.Y. Jeong, J.M. Morris, A.B. Perlman, *Crack Propagation Life of Detail Fractures in Rails*, United States. Federal Railroad Administration. Office of Research and Development, 1988.

[38] B. Dirks, R. Enblom, A. Ekberg, M. Berg, The development of a crack propagation model for railway wheels and rails. *Fatigue & Fracture of Engineering Materials & Structures* 38 (2015) 1478-1491. doi:10.1111/ffe.12318.

[39] W. Sung, S. Ming-hsiang, L. Cheng-I, G.C. Germ, The critical loading for lateral buckling of continuous welded rail. *Journal of Zhejiang University-SCIENCE A* 6 (2005) 878-885. doi:10.1631/jzus.2005.A0878.

[40] A. Kish, G. Samavedam, *Track Buckling Prevention: Theory, Safety Concepts, and Applications (no. DOT/FRA/ORD-13/16)*, United States. Federal Railroad Administration. Office of Research and Development, 2013.

[41] N. Lim, N. Park, Y. Kang, Stability of continuous welded rail track. *Computers & Structures* 81 (2003) 2219-2236. doi:*https://doi.org/10.1016/S0045-7949(03)00287-6*.

[42] K. Dobney, C.J. Baker, A.D. Quinn, L. Chapman, Quantifying the effects of high summer temperatures due to climate change on buckling and rail related delays in south-east United Kingdom. *Meteorological Applications* 16 (2009) 245-251. doi:10.1002/met.114.

[43] U. Zerbst, S. Beretta, Failure and damage tolerance aspects of railway components. *Engineering Failure Analysis* 18 (2011) 534-542. doi:*https://doi.org/10.1016/j.engfailanal.2010.06.001*.

[44] H. Nazmul, Allowable Bending Fatigue Stress of Rails. *Practice Periodical on Structural Design and Construction* 20 (2015) 04014033. doi:10.1061/(ASCE)SC.1943-5576.0000228.

[45] Taking the stress out of engineering, *https://www.scienceinschool.org/print/269* (Accessed June 1, 2020).

[46] D. F. Cannon, H. Pradier, Rail rolling contact fatigue Research by the European Rail Research Institute. *Wear* 191 (1996) 1-13. doi:*https://doi.org/10.1016/0043-1648(95)06650-0*.

[47] G. Schleinzer, F.D. Fischer, Residual stresses in new rails. *Materials Science and Engineering: A* 288 (2000) 280-283. doi:*https://doi.org/10.1016/S0921-5093(00)00872-8*.

[48] G. Schleinzer, F.D. Fischer, Residual stress formation during the roller straightening of railway rails. *International Journal of Mechanical Sciences* 43 (2001) 2281-2295.

[49] T. Sasaki, S. Takahashi, Y. Kanematsu, Y. Satoh, K. Iwafuchi, M. Ishida, Y. Morii, Measurement of residual stresses in rails by neutron diffraction. *Wear* 265 (2008) 1402-1407. doi:*https://doi.org/10.1016/j.wear.2008.04.047*.

[50] D. I. Fletcher, F.J. Franklin, A. Kapoor, 9 - Rail surface fatigue and wear. *Wheel–Rail Interface Handbook* (2009) 280-310. doi:*https://doi.org/10.1533/9781845696788.1.280*.

[51] Y. Kimura, M. Sekizawa, A. Nitanai, Wear and fatigue in rolling contact. *Wear* 253 (2002) 9.

[52] E. E. Magel, *Rolling Contact Fatigue: A Comprehensive Review (no. DOT/FRA/ORD-11/24)*, United States. Federal Railroad Administration. Office of Research and Development, 2011.

[53] W. Zhong, J.J. Hu, P. Shen, C.Y. Wang, Q.Y. Lius, Experimental investigation between rolling contact fatigue and wear of high-speed and heavy-haul railway and selection of rail material. *Wear* 271 (2011) 2485.

[54] M. L. Lyons, Jeong DY, Gordon JE, Fracture mechanics approach to estimate rail wear limits, *American Society of Mechanical Engineers, Rail Transportation Division Conference,* 2010, vol. 48944, pp. 137-146.

[55] U. Olofsson, T. Telliskivi, Wear, plastic deformation and friction of two rail steels - A full-scale test and a laboratory study. *Wear* 254 (2003) 80.

[56] A. M. Zarembski, D. Einbinder, N. Attoh-Okine, Using multiple adaptive regression to address the impact of track geometry on development of rail defects. *Construction and Building Materials* 127 (2016) 546-555. doi:10.1016/j.conbuildmat.2016.10.012.

[57] A. M. Zarembski, Bonaventura CS, Dynamic effects of track surface condition on vertical wheel/rail forces and energy consumption, *Proceedings of the ASME Joint Rail Conference 2010, JRC20,* 10 2010, pp. 1-6.

[58] R. Mohammadi, Q. He, F. Ghofrani, A. Pathak, A. Aref, Exploring the impact of foot-by-foot track geometry on the occurrence of rail defects. *Transportation Research Part C: Emerging Technologies* 102 (2019) 153-172. doi:*https://doi-org/10.1016/j.trc.2019.03.004*.

[59] FRA (Federal Railroad Administration), *Track Safety Standard Compliance Manual*, US Dept. of Transportation Washington, DC, 2018.

[60] Transport Canada, Rules Respecting Track Safety. (2011).

[61] British Standard, Railway applications-Track-Track geometry quality-Part 5: Geometric quality levels-Plain line. 3. *BS EN 13848-5: 2008 A1: 2010* (2010).

[62] British Standard, Railway applications. Track. Track geometry quality. Characterisation of track geometry quality. *BS EN 13848-6:2014* (2014).

[63] Rail transportation occurrences in 2018 - Statistical Summary - Transportation Safety Board of Canada, *https://www.tsb.gc.ca/eng/stats/rail/2018/sser-ssro-2018.html* (Accessed Jun 6, 2020).

[64] Q. He, H. Li, D. Bhattacharjya, D.P. Parikh, A. Hampapur, Track geometry defect rectification based on track deterioration modelling and derailment risk assessment. *Journal of the Operational Research Society* 66 (2015) 392-404. doi:10.1057/jors.2014.7.

[65] M. El-Sibaie, Y. Zhang, Objective track quality indices. *Transportation Research Record* (2004) 81.

[66] J. Sadeghi, H. Askarinejad, An investigation into the effects of track structural conditions on railway track geometry deviations. *Proceedings of the Institution of Mechanical Engineers, Part F: Journal of Rail and Rapid Transit* 223 (2009) 415-425. doi:10.1243/09544097JRRT266.

[67] J. Sadeghi, Development of railway track geometry indexes based on statistical distribution of geometry data. *Journal of Transportation Engineering* 136 (2010) 693-700. doi:10.1061/(ASCE)0733-947X(2010)136:8(693).

[68] J. Sadeghi, M. Emad Motieyan, J. Ali Zakeri, Development of integrated railway ballast quality index. (2019). doi:10.1080/10298436.2019.1577418.

[69] J. Sadeghi, M.E. Motieyan Najar, J.A. Zakeri, C. Kuttelwascher, Development of railway ballast geometry index using automated measurement system. *Measurement: Journal of the International Measurement Confederation* 138 (2019) 132-142. doi:10.1016/j.measurement.2019.01.092.

[70] J. Sadeghi, M. Fathali, N. Boloukian, Development of a new track geometry assessment technique incorporating rail cant factor. *Proc.Inst.Mech.Eng.F, J.Rail Rapid Transit (UK)* 223 (2009) 255.

[71] L. Liu, Wang J, Lv R, Finite element analysis of ballastless track rail-floating slab's dynamic characteristics, 2011, pp. 3907.

[72] X. Chen, L. Wang, X. Tao, G. Cui, F. Yang, X. Chai, W. Wu, Study on the judgment method for track regularity of the main railway lines in China. *Zhongguo Tiedao Kexue/China Railway Science* 29 (2008) 21.

[73] Z. Liu, Luo S, Ma W, Song R, Application research of track irregularity PSD in the high-speed train dynamic simulation, 2009, pp. 2845.

[74] A.R.B. Berawi, Improving railway track maintenance using power spectral density (PSD), Universidade do Porto (Portugal), 2013.

[75] E. T. Selig, D. Li, Track modulus: its meaning and factors influencing it. *Transportation Research Record* (1994) 47-54.

[76] Z. Cai, G.P. Raymond, R.J. Bathurst, Estimate of static track modulus using elastic foundation models. *Transportation Research Record* (1994) 65.

[77] W. Ebersohn, E.T. Selig, Track modulus measurements on a heavy haul line. *Transportation Research Record* (1994) 73.

[78] R. M. Narayanan, J.W. Jakub, D. Li, S.E.G. Elias, Railroad track modulus estimation using ground penetrating radar measurements. *NDT & E International* 37 (2004) 141-151. doi:10.1016/j.ndteint.2003.05.003.

[79] A. D. Kerr, On the determination of the rail support modulus k. *International Journal of Solids and Structures* 37 (2000) 4335-4351. doi://doi.org/10.1016/S0020-7683(99)00151-1.

[80] A. Lopez Pita, P.F. Teixeira, F. Robuste, High speed and track deterioration: The role of vertical stiffness of the track. *Proceedings of the Institution of Mechanical Engineers, Part F: Journal of Rail and Rapid Transit* 218 (2004) 31-40. doi:10.1243/095440904322804411.

[81] D. Read, S. Chrismer, W. Ebersohn, E. Selig, Track modulus measurements at the Pueblo soft subgrade site. *Transportation Research Record* 1470 (1994) 55.

[82] T. Dahlberg, Railway Track Stiffness Variations - Consequences and Countermeasures. *International Journal of Civil Engineering* 8 (2010) 1-12.

[83] A. M. Zarembski, J. Palese, Transitions eliminate impact at crossings. *RT and S: Railway Track and Structures* 99 (2003) 28-30.

[84] D. D. Davis, D. Otter, D. Li, S. Singh, P.C. Simmons-Boardman, Bridge Approach Performance in Revenue Service. *Railway Track and Structures* 99 (2003) p. 18-20.

[85] T. R. Sussmann, W. Ebersohn, E.T. Selig, Fundamental nonlinear track load-deflection behavior for condition evaluation. *Transportation Research Record* (2001) 61-67.

[86] AREMA, American railway engineering and maintenance-of-way association. *Manual for railway engineering, Volume 4* (2013).

[87] J. W. P. Redden, E.T. Selig, A.M. Zaremsbki, Stiff track modulus considerations. *Railway Track and Structures* 98 (2002) 25-30.

[88] G. P. Raymond, Analysis of track support and determination of track modulus. *Transportation Research Record* (1985) pp 80-90.

[89] A. D. Kerr, A method for determining the track modulus using a locomotive or car on multi-axle trucks. *Proceedings AREA* 84 (1983) 269-286.

[90] M. Burrow, P. Texeira, E.G. Berggren, T. Dahlberg, Track stiffness considerations for high speed railway lines, *Railway Transportation: Policies, Technology and Perspectives*, Nova Science Publishers, Inc., 2009, pp. 1-55.

[91] A. López-Pita, P.F. Teixeira, C. Casas, L. Ubalde, F. Robusté, Evolution of track geometric quality in high-speed lines: Ten years experience of the Madrid-Seville line: *Proceedings of the Institution of Mechanical Engineers, Part F: Journal of Rail and Rapid Transit* (2007). doi:10.1243/0954409JRRT62.

[92] B. Brickle, R. Morgan, E. Smith, J. Brosseau, C. Pinney, Identification of Existing and New Technologies for Wheelset Condition Monitoring. *TTCI Ltd UK RSSB Report for Task T607*2008.

[93] C. Thompson, Reichl P, Zeng D, White J, Ahmed F, Sethi H, Predictive maintenance approaches based on continuous monitoring systems at Rio Tinto, *CORE 2016, Maintaining the Momentum, Conference on Railway Excellence,* Melbourne, Victoria, 16-18 May 2016, pp. 7p.

[94] M. Jesussek, K. Ellermann, Fault detection and isolation for a full-scale railway vehicle suspension with multiple Kalman filters. *Vehicle System Dynamics* 52 (2014) 1695-1715. doi:10.1080/00423114.2014.959026.

[95] Y. Hayashi, T. Kojima, H. Tsunashima, Y. Marumo, Real time fault detection of railway vehicles and tracks. *IET Seminar Digest* 2006 (2006) 20-25. doi:20060037.

[96] C. Li, S. Luo, C. Cole, M. Spiryagin, An overview: modern techniques for railway vehicle on-board health monitoring systems. *Vehicle System Dynamics* 55 (2017) 1045-1070. doi:10.1080/00423114.2017.1296963.

[97] E. Berggren, A. Jahlenius, B.E. Bengtsson, Continuous Track Stiffness Measurement: an Effective Method to Investigate the Structural Conditions of the Track. *Railway Engineering - International Conference* (2002) P39.

[98] P. Wang, L. Wang, R. Chen, J. Xu, J. Xu, M. Gao, Overview and outlook on railway track stiffness measurement. *Journal of Modern Transportation* 24 (2016) 89-102. doi:10.1007/s40534-016-0104-8.

[99] J. Nielsen, E. Berggren, T. Lölgen, R. Müller, Overview of Methods for Measurement of Track Irregularities Important for Ground-Borne Vibration. *RIVAS Railway Induced Vibration Abatement Solutions Collaborative Project* (2013).

[100] Trip Report: A Look Inside the TTC - Chapter 3, *http://www.drgw.net/trips/report.php?tr=TTCI.3* (Accessed Jun 8, 2020).

[101] D. Li, Thompson R, Kalay S, Update of TTCI's research in track condition testing and inspection, *Proc. of the 2004 AREMA Annual Conference,* 2004.

[102] R. Thompson, P. Marquez, Track strength testing using TTCI's track loading vehicle. *Railway track and Structures* 97 (2001).

[103] E. Berggren, Berg M, Simulation, Development and Field Testing of a Track Stiffness Measurement Vehicle, Rio de Janeiro, 14th-16th of June 2005.

[104] E. G. Berggren, A.M. Kaynia, B. Dehlbom, Identification of substructure properties of railway tracks by dynamic stiffness measurements and simulations. *Journal of Sound and Vibration* 329 (2010) 3999-4016. doi:*https://doi.org/10.1016/j.jsv.2010.04.015*.

[105] M. Hosseingholian, M. Froumentin, D. Levacher, Continuous method to measure track stiffness a new tool for inspection of rail infrastructure. *World Applied Sciences Journal* 6 (2009) 579-589.

[106] M. Hosseingholian, Foumentin M, Robinet A, Dynamic track modulus from measurement of track acceleration by portancemetre, *9th World Congress on Railway Research,* Lille, France, 22 to 26 May 2011.

[107] C.D. Norman, Measurement of track modulus from a moving railcar, MSc. Thesis, University of Nebraska-Lincoln, 2004.

[108] S. Lu, Duan H, Greisen C, Farritor S, Arnold R, Hogan C, Dick M, Fateh M, Carr G, Case studies determining the effects of track stiffness on vehicle dynamics, *ASME 2010 Joint Rail Conference, JRC2010, April 27, 2010 - April 29,* 2010 2010, pp. 145-154.

[109] S. Lu, Hogan C, Minert B, Arnold R, Farritor S, GeMeiner W, Clark D, Exception criteria in vertical track deflection and modulus, *2007 ASME/IEEE Joint Rail Conference and the ASME Internal Combustion Engine Division, Spring Technical Conference, JRCICE2007, March 13, 2007 - March 16,* 2007 2007, pp. 191-198.

[110] S. F. Nafari, M. Gül, A. Roghani, M.T. Hendry, R.J. Cheng, Evaluating the potential of a rolling deflection measurement system to estimate track modulus. *Proceedings of the IMechE* (2018) 0954409716646404. doi:10.1177/0954409716646404.

[111] S. F. Nafari, M. Gül, J.J.R. Cheng, Quantifying live bending moments in rail using train-mounted vertical track deflection measurements and track modulus estimations. *Journal of Civil Structural Health Monitoring* 7 (2017) 637-643. doi:10.1007/s13349-017-0248-1.

[112] R. Alireza, M.T. Hendry, Continuous Vertical Track Deflection Measurements to Map Subgrade Condition along a Railway Line: Methodology and Case Studies. *Journal of Transportation Engineering* 142 (2016) 04016059. doi:10.1061/(ASCE)TE.1943-5436.0000892.

[113] A. Roghani, M.T. Hendry, Quantifying the impact of subgrade stiffness on track quality and the development of geometry defects. *Journal of Transportation Engineering* 143 (2017). doi:10.1061/JTEPBS.0000043.

[114] S. Choi, A. Cichocki, H. Park, S. Lee, Blind source separation and independent component analysis: A review. 6 (2004).

[115] G. Kerschen, F. Poncelet, J.-. Golinval, Physical interpretation of independent component analysis in structural dynamics. *Mechanical Systems and Signal Processing* 21 (2007) 1561-1575. doi:*https://doi-org.login.ezproxy.library.ualberta.ca/10.1016/j.ymssp.2006.07.009*.

[116] A. Belouchrani, K. Abed-Meraim, J. -. Cardoso, E. Moulines, A blind source separation technique using second-order statistics. *IEEE Transactions on Signal Processing* 45 (1997) 434-444. doi:10.1109/78.554307.

[117] B. Hazra, A. Sadhu, A.J. Roffel, S. Narasimhan, Hybrid Time-Frequency Blind Source Separation Towards Ambient System Identification of Structures. *Computer-Aided Civil and Infrastructure Engineering* 27 (2012) 314-332. doi:10.1111/j.1467-8667.2011.00732.x.

[118] P. D. O'grady, B.A. Pearlmutter, S.T. Rickard, Survey of sparse and non-sparse methods in source separation. *International Journal of Imaging Systems and Technology* 15 (2005) 18-33.

[119] R. Bro, PARAFAC. Tutorial and applications. *Chemometrics and Intelligent Laboratory Systems* 38 (1997) 149-172.

[120] J. D. Carroll, J. Chang, Analysis of individual differences in multidimensional scaling via an N-way generalization of "Eckart-Young" decomposition. *Psychometrika* 35 (1970) 283-319.

[121] F. J. Theis, Meyer-Baese A, Lang EW, Second-order blind source separation based on multi-dimensional autocovariances, *International Conference on Independent Component Analysis and Signal Separation,* 2004, pp. 726-733.

[122] F. Abazarsa, S.F. Ghahari, F. Nateghi, E. Taciroglu, Response-only modal identification of structures using limited sensors. *Structural Control and Health Monitoring* 20 (2013) 987-1006. doi:10.1002/stc.1513.

[123] H. Ma, Q. Jiang, Z. Liu, G. Liu, Z. Ma, A novel blind source separation method for single-channel signal. *Signal Processing* 90 (2010) 3232-3241. doi:*https://doi.org/10.1016/j.sigpro.2010.05.029*.

[124] M. G. López P., H. Molina Lozano, L. P. Sánchez F, L. N. Oliva Moreno, Blind Source Separation of audio signals using independent component analysis and wavelets, *CONIELECOMP 2011, 21st International Conference on Electrical Communications and Computers,* 2011, pp. 152-157.

[125] Y. Guo, S. Huang, Y. Li, Single-Mixture Source Separation Using Dimensionality Reduction of Ensemble Empirical Mode Decomposition and Independent Component Analysis. *Circuits, Systems, and Signal Processing* 31 (2012) 2047-2060. doi:10.1007/s00034-012-9414-1.

[126] A. Ozerov, P. Philippe, F. Bimbot, R. Gribonval, Adaptation of bayesian models for single-channel source separation and its application to voice/music separation in popular songs. *IEEE Transactions on Audio, Speech and Language Processing* 15 (2007) 1564-1578. doi:10.1109/TASL.2007.899291.

[127] G. Jang, T. Lee, A Maximum Likelihood Approach to Single-Channel Source Separation. *J.Mach.Learn.Res.* 4 (2004) 1365–1392. doi:10.1162/jmlr.2003.4.7-8.1365.

[128] H. Zhu, X. Wang, T. Rui, Y. Li, H. Zhang, Y. Zhao, Shift invariant sparse coding for blind source separation of single channel mechanical signal. *Zhendong Gongcheng Xuebao/Journal of Vibration Engineering* 28 (2015) 625-632. doi:10.16385/j.cnki.issn.1004-4523.2015.04.016.

[129] B. Gao, W.L. Woo, S.S. Dlay, Single-channel source separation using EMD-subband variable regularized sparse features. *IEEE Transactions on Audio, Speech and Language Processing* 19 (2011) 961-976. doi:10.1109/TASL.2010.2072500.

[130] Y. Guo, Naik GR, Nguyen H, Single channel blind source separation based local mean decomposition for Biomedical applications, *2013 35th Annual International Conference of the IEEE Engineering in Medicine and Biology Society, EMBC 2013, July 3, 2013 - July 7, 20,* 13 2013, pp. 6812-6815.

[131] P. Dey, U. Satija, B. Ramkumar, Single channel blind source separation based on variational mode decomposition and PCA. *2015 Annual IEEE India Conference (INDICON)* (2015) 1-5. doi:10.1109/INDICON.2015.7443723.

[132] M. Mehrali, M. Esmaeili, S. Mohammadzadeh, Application of data mining techniques for the investigation of track geometry and stiffness variation. *Proceedings of the Institution of Mechanical Engineers, Part F: Journal of Rail and Rapid Transit* (2019) 0954409719844885. doi:10.1177/0954409719844885.

[133] A. Roghani, M.T. Hendry, Quantifying the Impact of Subgrade Stiffness on Track Quality and the Development of Geometry Defects. *Journal of Transportation Engineering, Part A: Systems* 143 (2017) 04017029. doi:10.1061/JTEPBS.0000043.

[134] D. M. Read, Plotkin D, Issues Surrounding the Measurement and Application of Vertical Track Stiffness Data, *Poceedings of the 2009 Joint Rail Conference. 2009 Joint Rail Conference,* Pueblo, Colorado, USA., March 4–5, 2009, pp. 79-87.

[135] M. P. N. Burrow, A.H.C. Chan, A. Shein, Deflectometer-based analysis of ballasted railway tracks. *Proceedings of the Institution of Civil Engineers: Geotechnical Engineering* 160 (2007) 169-177. doi:10.1680/geng.2007.160.3.169.

[136] C.J. Greisen, Measurement, simulation, and analysis of the mechanical response of railroad track, MSc Thesis, University of Nebraska - Lincoln, 2010.

[137] R. Thompson, Li D, Automated vertical track strength testing using TTCI's track loading vehicle, *Technology Digest,* February 2002.

[138] S. Rasmussen, Krarup JA, Hildebrand G, Non-Contact Deflection Measurement at High Speed, *Proc. 6th Int. Conf. Bearing Capacity Roads Railways and Airfields, ,* Lisbon, Portugal, 2002, pp. 53-60.

[139] C. With, A.V. Metrikine, A. Bodare, Identification of effective properties of the railway substructure in the low-frequency range using a heavy oscillating unit on the track. *Archive of Applied Mechanics* 80 (2010) 959-968. doi:10.1007/s00419-009-0348-4.

[140] A. Roghani, M. Hendry, M. Ruel, T. Edwards, P. Sharpe, J. Hyslip, A case study of the assessment of an existing rail line for increased traffic and axle loads. *Proc., International Heavy Haul Association, International Heavy Haul Association, Virginia Beach, VA* (2015).

[141] A. Roghani, M. T. Hendry, Assessing the potential of a technology to map the subgrade stiffness under the rail tracks, *Transportation Research Board 94th Annual Meeting,* Washington DC, United States, 2015.

[142] A. Roghani, Macciotta R, Hendry M, Combining track quality and performance measures to assess track maintenance requirements, *ASME/ASCE/IEEE 2015 Joint Rail Conference, JRC 2015,* San Jose, CA, United states, March 23-26, 2015.

[143] M. El-Sibaie, GeMeiner W, Clark D, Al-Nazer L, Arnold R, Farritor S, Fateh M, Lu S, Carr G, Measurement of Vertical Track Modulus: Field Testing, Repeatability, and Effects of Track Geometry, 2009, pp. 151-158.

[144] J. Sadeghi, P. Barati, Evaluation of conventional methods in Analysis and Design of Railway Track System. *IJCE* 8 (2010) 44-56.

[145] H. Feng, 3D-models of railway track for dynamic analysis, MSc. Thesis, Royal Institute of Technology, Stockholm, Sweden, 2011.

[146] J. A. Zakeri, R. Abbasi, Field investigation on variation of rail support modulus in ballasted railway tracks. *Latin American Journal of Solids and Structures* 9 (2012) 643-656.

[147] T. R. Sussmann, H.B. Thompson, T.D. Stark, S.T. Wilk, C.L. Ho, Use of seismic surface wave testing to assess track substructure condition. *Construction and Building Materials* 155 (2017) 1250-1255. doi:*https://doi.org/10.1016/j.conbuildmat.2017.02.077*.

[148] CSIBridge, Computers and Structures. *CSI Berkeley, California* (2015).

[149] S. S. Haykin, *Neural Networks and Learning Machines*, Prentice Hall, New York, 2009.

[150] G. Cybenko, Approximation by superpositions of a sigmoidal function. *Mathematics of Control, Signals, and Systems* 2 (1989) 303-14. doi:10.1007/BF02551274.

[151] H. Guler, Prediction of railway track geometry deterioration using artificial neural networks: A case study for Turkish state railways. *Structure and Infrastructure Engineering* 10 (2014) 614-626. doi:10.1080/15732479.2012.757791.

[152] O. Fink, Weidmann U, Scope and potential of applying artificial neural networks in reliability prediction with a focus on railway rolling stock, *European Safety and Reliability Conference: Advances in Safety, Reliability and Risk Management, ESREL 2011, September 18, 2011 - September 22,* 2011 2012, pp. 508-514.

[153] J. Sadeghi, H. Askarinejad, Application of neural networks in evaluation of railway track quality condition. *Journal of Mechanical Science and Technology* 26 (2012) 113-122. doi:10.1007/s12206-011-1016-5.

[154] R. J. Hyndman, A.B. Koehler, Another look at measures of forecast accuracy. *International Journal of Forecasting* 22 (2006) 679-688. doi://doi.org/10.1016/j.ijforecast.2006.03.001.

[155] S.F. Nafari, Quantifying the Distribution of Rail Bending Stresses along the Track using Train-Mounted Deflection Measurements, PhD Dissertation, University of Alberta, 2017.

[156] S. Young, G. Evermann, M. Gales, T. Hain, D. Kershaw, X. Liu, G. Moore, J. Odell, D. Ollason, D. Povey, The HTK book.

[157] International Union of Railways, Online Statistics-Synopsis 2017, *https://uic.org/statistics#Statistics-Group* (Accessed November 28, 2018).

[158] J. Nielsen, E. Berggren, T. Lölgen, R. Müller, Overview of methods for measurement of track irregularities. *RIVAS Railway Induced Vibration Abatement Solutions Collaborative Project* (2013).

[159] A. Alemi, F. Corman, G. Lodewijks, Condition monitoring approaches for the detection of railway wheel defects. *Proceedings of the Institution of Mechanical Engineers, Part F: Journal of Rail and Rapid Transit* 231 (2017) 961-981. doi:10.1177/0954409716656218.

[160] Transportation Safety Board of Canada, Statistical Summary – Railway Occurrences 2018, *https://www.tsb.gc.ca/eng/stats/rail/2018/sser-ssro-2018.html* (Accessed December 01, 2019).

[161] C. Tyler Dick, C. Barkan, E. Chapman, M. Stehly, Multivariate Statistical Model for Predicting Occurrence and Location of Broken Rails. *Transportation Research Record: Journal of the Transportation Research Board* 1825 (2003) 48-55. doi:10.3141/1825-07.

[162] J. Magiera, J. Orkisz, W. Karmowski, Reconstruction of residual stresses in railroad rails from measurements made on vertical and oblique slices. *Wear* 191 (1996) 78-89.

[163] Y. Y. Wang, F.P. Chiang, Experimental Study of Three-dimensional Residual Stresses in Rails by Moire Interferometry and Dissecting Methods. *Optics and Lasers in Engineering* 27 (1997) 89-100.

[164] H. Naderi, Mirabadi A, Railway track condition monitoring using FBG and FPI fiber optic sensors, *IET International Conference on Railway Condition Monitoring,* Birmingham, United kingdom, November 29, 2006 - November 30, 2006, pp. 198-203.

[165] G. Strang, T. Nguyen, *Wavelets and Filter Banks*, Wellesley-Cambridge, Wellesley, Mass.; Stockport, 2009.

[166] S. G. Mallat, *A Wavelet Tour of Signal Processing : The Sparse Way*, Elsevier/Academic Press, Amsterdam ;Boston, 2009.

[167] I. Daubechies, *Ten Lectures on Wavelets*, Society for Industrial and Applied Mathematics, Philadelphia, PA, 1992.

[168] C. K. Chui, *An Introduction to Wavelets*, Academic Press, Boston, 1992.

[169] M. M. R. Taha, A. Noureldin, J.L. Lucero, T.J. Baca, Wavelet Transform for Structural Health Monitoring: A Compendium of Uses and Features. *Structural Health Monitoring* 5 (2006) 267-295. doi:10.1177/1475921706067741.

[170] S. G. Mallat, A theory for multiresolution signal decomposition: the wavelet representation. *IEEE Transactions on Pattern Analysis and Machine Intelligence* 11 (1989) 674-693. doi:10.1109/34.192463.

[171] M. E. Davies, C.J. James, Source separation using single channel ICA. *Signal Processing* 87 (2007) 1819-1832. doi:*https://doi.org/10.1016/j.sigpro.2007.01.011*.

[172] H. Shao, X. Shi, L. Li, Power signal separation in milling process based on wavelet transform and independent component analysis. *International Journal of Machine Tools and Manufacture* 51 (2011) 701-710. doi:*https://doi.org/10.1016/j.ijmachtools.2011.05.006*.

[173] B. Mijović, M. De Vos, I. Gligorijević, J. Taelman, S. Van Huffel, Source Separation From Single-Channel Recordings by Combining Empirical-Mode Decomposition and Independent Component Analysis. *IEEE Transactions on Biomedical Engineering* 57 (2010) 2188-2196. doi:10.1109/TBME.2010.2051440.

[174] M. F. Isham, M.S. Leong, M.H. Lim, Z.A. Ahmad, Variational mode decomposition: mode determination method for rotating machinery diagnosis. *Journal of Vibroengineering* 20 (2018) 2604-2621. doi:10.21595/jve.2018.19479.

[175] Z. Wu, N.E. Huang, Ensemble empirical mode decomposition: a noise-assisted data analysis method. *Advances in Adaptive Data Analysis* 01 (2009) 1-41. doi:10.1142/S1793536909000047.

[176] H. Sun, H. Wang, J. Guo, A Single-Channel Blind Source Separation Technique Based on AMGMF and AFEEMD for the Rotor System. *IEEE Access* 6 (2018) 50882-50890. doi:10.1109/ACCESS.2018.2868643.

[177] L. Sun, C. Zhao, M. Su, F. Wang, Single-channel blind source separation based on joint dictionary with common sub-dictionary. *International Journal of Speech Technology* 21 (2018) 19-27. doi:10.1007/s10772-017-9469-2.

[178] C. Wu, Z. Liu, X. Wang, W. Jiang, X. Ru, Single-Channel Blind Source Separation of Co-Frequency Overlapped GMSK Signals Under Constant-Modulus Constraints. *IEEE Communications Letters* 20 (2016) 486-489. doi:10.1109/LCOMM.2016.2521737.

[179] G. Li, G. Tang, G. Luo, H. Wang, Underdetermined blind separation of bearing faults in hyperplane space with variational mode decomposition. *Mechanical Systems and Signal Processing* 120 (2019) 83-97. doi:*https://doi.org/10.1016/j.ymssp.2018.10.016*.

[180] A. Sadhu, S. Narasimhan, J. Antoni, A review of output-only structural mode identification literature employing blind source separation methods. *Mechanical Systems and Signal Processing* 94 (2017) 415-431. doi:*https://doi.org/10.1016/j.ymssp.2017.03.001*.

[181] E. G. Berggren, A. Nissen, B.S. Paulsson, Track deflection and stiffness measurements from a track recording car. *Proceedings of the Institution of Mechanical Engineers, Part F: Journal of Rail and Rapid Transit* 228 (2014) 570-580. doi:10.1177/0954409714529267.

[182] N. Golyandina, A. Zhigljavsky, *Singular Spectrum Analysis for Time Series*, Springer Berlin Heidelberg, 2013.

[183] J. B. Elsner, A.A. Tsonis, *Singular Spectrum Analysis: A New Tool in Time Series Analysis*, Plenum Press, New York, 1996.

[184] L. Tong, V. C. Soon, Y. F. Huang, R. Liu, AMUSE: a new blind identification algorithm. *IEEE International Symposium on Circuits and Systems* (1990) 1784-1787 vol.3. doi:10.1109/ISCAS.1990.111981.

[185] J. Virta, K. Nordhausen, Determining the signal dimension in second order source separation. *Statistica Sinica* (2020). doi:10.5705/ss.202018.0347.

[186] A. K. Maddirala, R. A. Shaik, Removal of EMG artifacts from single channel EEG signal using singular spectrum analysis. *2015 IEEE International Circuits and Systems Symposium (ICSyS)* (2015) 111-115. doi:10.1109/CircuitsAndSystems.2015.7394075.

[187] A. K. Maddirala, R.A. Shaik, Motion artifact removal from single channel electroencephalogram signals using singular spectrum analysis. *Biomedical Signal Processing and Control* 30 (2016) 79-85. doi:*https://doi.org/10.1016/j.bspc.2016.06.017*.

[188] D. A. Bridwell, S. Rachakonda, R.F. Silva, G.D. Pearlson, V.D. Calhoun, Spatiospectral Decomposition of Multi-subject EEG: Evaluating Blind Source Separation Algorithms on Real and Realistic Simulated Data. *Brain topography* 31 (2018) 47-61. doi:10.1007/s10548-016-0479-1.

[189] D. T. Pham, Joint Approximate Diagonalization of Positive Definite Hermitian Matrices. *SIAM Journal on Matrix Analysis and Applications* 22 (2001) 1136-1152. doi:10.1137/S089547980035689X.

[190] G. Chabriel, M. Kleinsteuber, E. Moreau, H. Shen, P. Tichavsky, A. Yeredor, Joint Matrices Decompositions and Blind Source Separation: A survey of methods, identification, and applications. *IEEE Signal Processing Magazine* 31 (2014) 34-43. doi:10.1109/MSP.2014.2298045.

[191] P. He, T. She, W. Li, W. Yuan, Single channel blind source separation on the instantaneous mixed signal of multiple dynamic sources. *Mechanical Systems and Signal Processing* 113 (2018) 22-35. doi:10.1016/j.ymssp.2017.04.004.

[192] M. Atikur Rahman Khan, D.S. Poskitt, A Note on Window Length Selection in Singular Spectrum Analysis. *Australian & New Zealand Journal of Statistics* 55 (2013) 87-108. doi:10.1111/anzs.12027.

[193] A. Cichocki, S. Amari, *Adaptive Blind Signal and Image Processing: Learning Algorithms and Applications*, J. Wiley, Chichester, New York, 2002.

[194] J. Miettinen, K. Nordhausen, H. Oja, S. Taskinen, Statistical properties of a blind source separation estimator for stationary time series. *Statistics & Probability Letters* 82 (2012) 1865-1873. doi:*https://doi.org/10.1016/j.spl.2012.06.025*.

[195] S. Farritor, R. Arnold, S. Lu, C. Hogan, *Real-Time Vertical Track Modulus Measurement System from a Moving Railcar (no. DOT/FRA/ORD-05/05)*, United States. Federal Railroad Administration. Office of Research and Development, No. DOT/FRA/ORD-05/05, 2006.

[196] X. Lei, Track Irregularity Power Spectrum and Numerical Simulation, *High Speed Railway Track Dynamics: Models, Algorithms and Applications*, Springer Singapore, Singapore, 2017, pp. 137-160.

[197] N. T. Do, M. Gül, S.F. Nafari, Continuous Evaluation of Track Modulus from a Moving Railcar Using ANN-Based Techniques. *Vibration* 3 (2020) 149-161. doi:10.3390/vibration3020012.

[198] S. Kaewunruen, A.M. Remennikov, Field trials for dynamic characteristics of railway track and its components using impact excitation technique. *NDT & E International* 40 (2007) 510-519. doi:*https://doi.org/10.1016/j.ndteint.2007.03.004*.

[199] P. Haji Abdulrazagh, M.T. Hendry, Case study of use of falling weight deflectometer to investigate railway infrastructure constructed upon soft subgrades. *Canadian Geotechnical Journal* 53 (2016) 1991-2000. doi:10.1139/cgj-2016-0083.

[200] C. A. Murray, W.A. Take, N.A. Hoult, Measurement of vertical and longitudinal rail displacements using digital image correlation. *Canadian Geotechnical Journal* 52 (2015) 141-155. doi:10.1139/cgj-2013-0403.

[201] D. Mishra, E. Tutumluer, H. Boler, J.P. Hyslip, T.R. Sussmann, Railroad track transitions with multidepth deflectometers and strain gauges. *Transportation Research Record* 2448 (2014) 105-114.

[202] Railway Investigation Report R05E0059, Derailment, Canadian National, Freight Train M30351-03, Mile 49.4, Edson Subdivision Wabamun, Alberta, 03 August 2005, *https://www.tsb.gc.ca/eng/rapports-reports/rail/2005/r05e0059/r05e0059.html* (Accessed Jul 1, 2020).

[203] M. T. Hendry, C.D. Martin, S.L. Barbour, Measurement of cyclic response of railway embankments and underlying soft peat foundations to heavy axle loads. *Canadian Geotechnical Journal* 50 (2013) 467-480. doi:10.1139/cgj-2012-0118.

[204] F. Benedetto, F. Tosti, A.M. Alani, An entropy-based analysis of GPR data for the assessment of railway ballast conditions. *IEEE Transactions on Geoscience and Remote Sensing* 55 (2017) 3900-3908. doi:10.1109/TGRS.2017.2683507.

[205] E. G. Berggren, Efficient track maintenance: Methodology for combined analysis of condition data. *Proceedings of the Institution of Mechanical Engineers, Part F: Journal of Rail and Rapid Transit* 224 (2010) 353-360. doi:10.1243/09544097JRRT354.